AMPHOTERICIN B ION CHANNELS RESTORE CYSTIC FIBROSIS AIRWAY SURFACE PHYSIOLOGY

BY

KATRINA ANNE MURAGLIA

DISSERTATION

Submitted in partial fulfillment of the requirements
for the degree of Doctorate of Philosophy in Biochemistry
in the Graduate College of the
University of Illinois at Urbana-Champaign, 2018

Urbana, Illinois

Doctoral Committee:

Professor Martin D. Burke, Chair
Professor Claudio Grosman
Professor Stephen G. Sligar
Professor Emad Tajkhorshid

ABSTRACT

Just as artificial limbs replace the physical function of a missing arm or leg, small molecule surrogates acting as prosthetics on the molecular scale could replace protein functions that are either dysfunctional or absent in humans. These 'molecular prosthetics' could build upon and interface with the existing architecture and residual function of the organism to restore normal physiology. Importantly, small molecules with the capacity to move ions across lipid membranes and act as surrogates for channels or transporters have already been shown to restore physiology in protein-deficient cells and animals. This approach could now potentially address diseases caused by a deficiency of protein function, even in cases of severely reduced or absent protein production, such as cystic fibrosis (CF).

Amphotericin B (AmB) is a natural product known to self-assemble into nonspecific ion channels in sterol-containing lipid membranes. It was long believed that AmB killed yeast through its inherent ion channel activity, existing primarily in the form of small aggregates that could insert into the lipid bilayer and cause toxic permeabilization. We demonstrate here that AmB actually predominantly forms large, extramembranous aggregates that kill yeast by extracting ergosterol (Erg), a required sterol in yeast membranes. Additionally, AmB is toxic to cells only when the ratio of AmB present exceeds that of membrane sterols. These mechanistic findings led to the development of two strategies to separate the ion channel forming capacity of AmB from its toxicity to eukaryotic cells. The first strategy utilizes low doses of AmB so as not to exceed the total membrane sterol content. The second strategy is to pre-complex AmB with the native sterol (ergosterol or cholesterol) to mitigate toxicity while retaining the channel forming activity. These two strategies proved to be successful in restoring growth to a strain of yeast missing essential potassium transporter proteins.

Cystic fibrosis (CF) is caused by loss-of-function mutations in the cystic fibrosis transmembrane conductance regulator (CFTR) anion channel, some of which result in little to no protein produced, rendering protein substrate-dependent current therapies ineffective in these cases. Loss-of-function mutations in the CFTR anion channel result in reduced apical bicarbonate transport and decreased airway surface liquid (ASL) pH, which impairs respiratory host defenses and leads to chronic lung infections. Because basolateral pumps and channels remain active in the absence of functional CFTR, we hypothesized that an outward-facing bicarbonate gradient would develop across the apical membrane, which could be harnessed by a bicarbonate-permeable small molecule channel.

Our current mechanistic understanding of the AmB ion channel allowed us to use it as a probe to test that hypothesis that an imperfect but anion-permeable small molecule ion channel surrogate for CFTR could restore ASL physiology. Here we report that AmB facilitates apical bicarbonate transport thereby increasing ASL pH. This effect is sustained for at least 48 hours and restores ASL viscosity and antimicrobial activity in CF patient-derived human lung epithelia across a range of genotypes, including those with little to no production of CFTR. AmB similarly increases ASL pH in $CFTR^{-/-}$ piglets. Dependence of the AmB-mediated rescue on Na^+/K^+ ATPase indicates that this unselective CFTR surrogate is functionally interfaced with the endogenous ion transport network driving transepithelial bicarbonate movement. Additionally, non-channel-based activities of CFTR, including regulation of other apical ion transporters, are not required for maintaining these key parameters of ASL physiology. These results suggest a potential CFTR-independent and therefore genotype-agnostic mechanism for addressing CF.

For my parents

"I shall be telling this with a sigh
Somewhere ages and ages hence:
Two roads diverged in a wood, and I—
I took the one less traveled by,
And that has made all the difference."

- Robert Frost

ACKNOWLEDGEMENTS

There are so many people to thank for helping me reach the end of my graduate work in one piece that I barely even know where to start. My first acknowledgement absolutely has to go to my advisor, Marty Burke. The first day we met, I almost skipped your talk because I wanted to go to lunch early, and I'm grateful for the friends who convinced me to go even though I thought it looked really boring. Thanks for seeing something in me that day and always pushing me from then on to be the best, most rigorous scientist I can be. I know we spent some time butting heads but when it comes down to it, you've taught me how to go after the biggest, most impactful of problems and to always be the most enthusiastic scientist in the room. Thank you also for unfettered Marty-isms and the most uses of "tremendous" I have ever heard uttered in one minute. Big thanks also to my committee: Dr. Claudio Grosman, Dr. Stephen G. Sligar, and Dr. Emad Tajkhorshid for your valuable feedback and support over the years. Claudio, special thanks to you for teaching me about membrane physiology and always asking the hard questions. I would also like to thank Dr. Mike Welsh for his mentorship and his entire lab for generously hosting me for a summer and numerous trips out to Iowa City. Thank you to Jeff Goldberg and Cara Day for their support and their smiles every day at the fourth floor elevator.

Thank you to everyone in the Burke group who made my stay on the fourth floor of RAL as enjoyable as it could have possibly been, especially the AmB subgroup for giving me their harshest, most well-thought out criticism every week. You have all helped mold me into the scientist I am today. Deepest thanks to the late, great Anuj Khandelwal whose passion and wonder for my own work reminded me why I did this in the first place. Anna SantaMaria, I thought you were too boring and quiet at first (I think there's a trend here) but as it turns out, you're one of the smartest, most delightful and science-savvy people I know, and over the years

we have spent together in the lab, you have easily become someone I consider part of my family. Rajeev Chorghade, I've said it many times and I'll say it again here, you are the best junior student and friend I could have ever asked to work with. Who else would I rather go with to the slaughterhouse at 7 AM on a Tuesday to get some fresh pig trachea (sorry you can't cook with raw pork anymore) or go on our weekly drives to Peoria and back? I would be remiss not to mention Grandpa Justin Struble, who taught me that I should do something to hold on to my identity and sanity outside of the lab, which leads me to extend a huge thank you to the 2013-2016 members of Illini Powerlifting for being exactly that, particularly Jessica Evans and Jeff Damasco. Without you, I would not have made it this far in grad school—I know that for a fact.

I would like to thank my loving family, immediate, extended, in law, for supporting me in any way they could; in particular, my parents, Ireneo and Jocelyn, who have always selflessly given me all the tools I have ever needed to get where I wanted to go. Because of your unfailing love and devotion, I am the person I am today, and there are not enough thanks in the world I could give to you in return that would equal your unimaginable sacrifices.

Last, but certainly not least, I would like to thank my husband, Ryan Muraglia, who stuck with me as life put us through the wringer. Thank you for Skype calls late into the night, flying (sometimes driving!) back and forth between Illinois and North Carolina, and stopping in Lexington that one time to bring me my favorite pie. You know me—I could go on forever trying to find all the words in the world to truly express my gratitude, but since there are only so many pages allotted for acknowledgments, this will have to suffice: I will always love you.

I also gratefully acknowledge the University of Illinois, the National Institutes of Health, Howard Hughes Medical Institute, the Medical Scholars Program, the Biochemistry Department, and Professor Martin Burke for funding.

TABLE OF CONTENTS

CHAPTER 1

CYSTIC FIBROSIS AND THE PROSPECT OF MOLECULAR PROSTHETICS

1.1 DISEASE INTRODUCTION TO CYSTIC FIBROSIS

Diseases caused by an excess of protein function can often be treated with small molecule inhibitors, which interact with overactive proteins to shut off the excess activity. A classic example is the small molecule inhibitor imatinib (Gleevec®). Chromosomal translocation in the gene *BCR-ABL* produces a constitutively active form of the enzyme tyrosine kinase, which then stimulates uncontrolled cell growth in white blood cells and leads to chronic myelogenous leukemia (CML). Imatinib is a specific inhibitor of the BCR-ABL tyrosine kinase and has had remarkable clinical impact on CML patients since its discovery (*1*). However, diseases instead caused by a deficiency of protein function, either from a dysfunctional or even completely missing protein, can be difficult to treat. Examples of these diseases include lysosomal storage disorders such as Tay-Sachs (*2*) and Fabry disease (*3*), hemoglobinopathies like β-thalassemia (*4*), and channelopathies like Bartter syndrome, Dravet syndrome, and Dent's disease (*5*). Our particular research interest was in this latter category, channelopathies: diseases characterized by a dysfunctional or missing protein ion channel.

One of the most recognizable of the channelopathies is cystic fibrosis (CF), a disease caused by loss-of-function mutations in the CF transmembrane conductance regulator (CFTR) protein, a 1480-amino acid cAMP-regulated anion channel (*6*). Patients with CFTR mutations exhibit abnormal epithelial anion (chloride and bicarbonate) transport, which leads to pancreatic insufficiency, gastrointestinal disease, hepatobiliary failure, male infertility, and elevated sweat chloride concentrations, which serves as a diagnostic marker. Importantly, it is the disease manifestations in the lung that contribute most to the morbidity and mortality in CF patients, an

accumulation of thick mucus, neutrophilic inflammation, progressive bronchiectasis, and chronic bacterial infection typically by *Pseudomonas aeruginosa*, *Staphylococcus aureus* and *Burkholderia cepacia* (*6-8*). While the *CFTR* gene was first characterized almost 30 years ago in 1989, it is considered an orphan disease affecting one in 3,000 live births and treatment of the underlying pathophysiology of CF is still challenging (*8*). This is likely due to the fact that the exact mechanism by which the loss of CFTR-mediated anion transport, both chloride and bicarbonate, leads to chronic airway infection is still unknown (*7*). The discovery of genetic mutations in the *CFTR* gene allows for relative ease of diagnosis but unfortunately, options for treatment remain limited (*6*).

1.2 CLASSIFICATION OF CFTR MUTATIONS

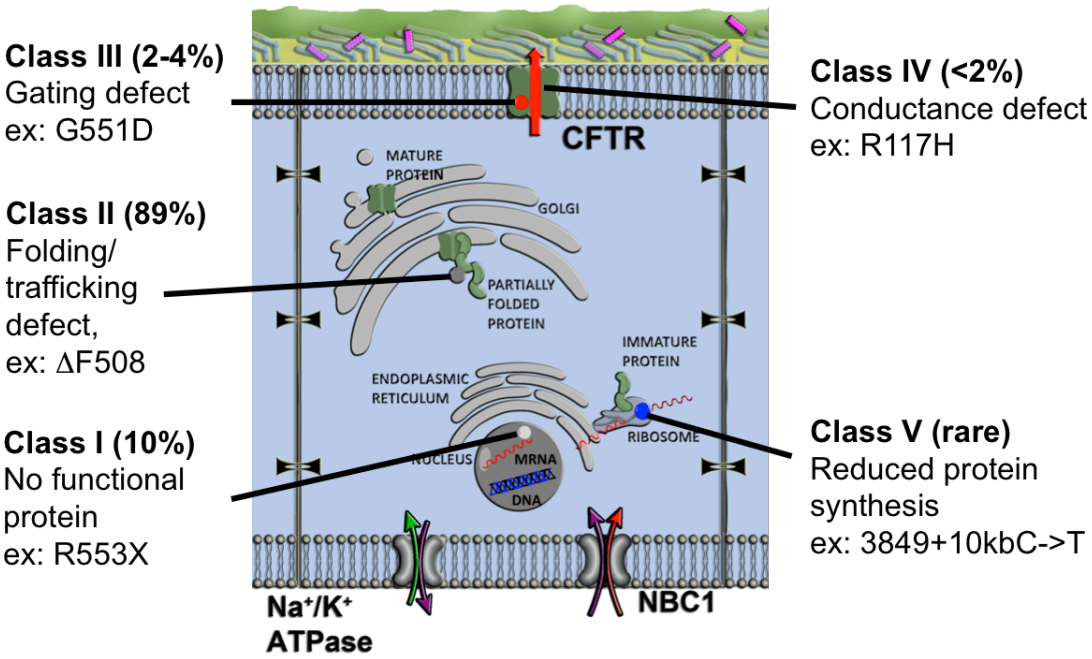

Figure 1.1. Classification of CFTR mutations. Hundreds of CF mutations cause disease through at least five major mechanisms of functional loss. Incidence is indicated within parenthesis and a specific example of each mutation class is given.

One of the major reasons why CF is so difficult to treat is because there are almost 2,000 known CFTR mutations, including missense, frameshift, nonsense and splice site defects,

truncations, and in-frame deletions/insertions (*6*). Hundreds of these mutations cause disease in CF patients through at least five major mechanisms of functional loss (Fig. 1.1) (*8*). Comprising 10% of CFTR defects, Class I includes nonsense mutations (specifically single point alterations that cause premature termination codons or PTCs) and splice site defects that interrupt CFTR biosynthesis and result in reduced or absent protein production (*8*). Because these mutations make little to no protein substrate, they are difficult to target with current small molecule-based therapies (*6*).

Class II mutations include the most common deletion of phenylalanine 508 (ΔF508), which appears in 85% of all CF patients, 50% of these bearing two copies of this allele (ΔF508/ΔF508). This class of mutations produces misfolded CFTR, which results in premature degradation before the protein reaches the cell membrane. Interestingly, when ΔF508/ΔF508 CFTR misfolding is corrected with small molecule-based therapies, it has gating and regulation defects similar to class III mutations as well as defective recycling and decreased stability in the plasma membrane as seen in class IV mutants. This phenomenon can make single classification difficult and therefore, may require therapies with broader application across mutations classes (*6, 8*).

Gating and regulation defects characterize class III mutations, which include the G551D allele. This is the third most common CFTR mutation and occurs in 2-4% of all CF patients. The protein is inserted into the membrane but has reduced open probability due to its defect, which interferes with ATP binding and phosphorylation. Class IV mutations are fairly rare and results in reduced single-channel anion conductance due to perturbations in ion-ion interactions inside the CFTR pore (*6*). In class V mutations, which are seen in less than 1% of all patients with CF, normal plasma membrane protein is produced but in drastically reduced quantities due to transcriptional dysregulation. This is largely due to splice defects, which make the level of

functional CFTR in each patient with these mutations highly variable even between different organs within the same patient (*8*). Sixth and seventh classes of mutations have also been proposed but not universal in CF literature, where CFTR is destabilized within the plasma membrane and disposed early by endocytosis or large deletions lead to untreatable mutations, respectively (*6*).

1.3 PROPOSED MECHANISMS OF CF PATHOPHYSIOLOGY

While the specific underlying mechanism of CF pathophysiology in the lung remains highly debated, both current major hypotheses revolve around maintenance of airway surface liquid (ASL) physiology. CFTR-mediated anion (chloride and bicarbonate) secretion as well as epithelial sodium channel (ENaC)-mediated sodium absorption comprise the majority of electrophysiological activity at the apical membrane of lung epithelia. It is universally accepted that cyclic AMP-stimulated chloride secretion is decreased in all CF animals. However, the competing hypotheses contend two different essential aspects of ASL physiology that must be corrected: 1) the hydration model proposes a detrimental decrease in lung fluid, while 2) the salt model, which later evolved into the pH model, suggests a salt imbalance in the airway that negatively affects the activity of antimicrobial proteins in the ASL (*9, 10*).

The ASL consists of a mucus layer, which traps debris and pathogens from further entering the body, and a periciliary liquid layer (PCL), which maintains clearance between the mucus layer and the underlying epithelia. In normal lungs, the PCL is approximately the same height as the length of the cilia when it is fully outstretched (7 μm) and allows for normal beating movement unimpeded by the mucus layer above (*11-14*). In the first major hypothesis for CF pathophysiology, largely championed by the Boucher group at the University of North Carolina, the lack of chloride secretion by CFTR results in reduced fluid movement to the airway surface

(*10*). As CFTR is hypothesized to inhibit ENaC, either through chloride ion movement or directly via protein-protein interaction, the loss of this inhibition then leads to sodium hyperabsorption (*15-18*). These two consequences compound to dehydrate and reduce the height of the ASL in CF cultured human lung epithelia to 3 μm, causing the mucus layer to physically obstruct the cilia and results in inhibited ciliary movement that normally clears mucus and debris from airway passages and protects against lung infections (*11-14*). This dehydration can be prevented by chemically inhibiting ENaC with the specific blocker amiloride (*9*). CF mice as well as mice with overexpression of ENaC also exhibit this same phenotype of reduced ASL height (*9, 11*). In this model, normal and CF ASL salt concentrations are similar (*10*).

A second hypothesis emerged when the Welsh group at the University of Iowa looked to determine the underlying cause of chronic CF airway infection. In CF cultured human lung epithelia, they found that ASL sodium and chloride concentrations were significantly higher than that of non-CF, but ASL height and sodium absorption were similar, contrary to the findings in support of the hydration model (*10, 19, 20*). One possible explanation for this is that the chloride conductance by CFTR and the ENaC conductance are parallel processes in the apical membrane, and elimination of chloride conductance magnifies sodium-dependent electrophysiological properties without actually increasing sodium absorption (*21*). More importantly, they also found that some bactericidal factor in non-CF ASL is active against *Pseudomonas aeruginosa, Staphylococcus aureus,* and *Escherichia coli* and therefore prevented infection, but it is inactivated in CF ASL due to this observed high ASL salt concentration. As the concentration of NaCl in the ASL increased, antibacterial activity against these strains decreased, but when salt concentration was decreased, bacterial killing was restored (*22*).

The production of a CF porcine model by the Welsh group in 2008 provided a tool with

which to further develop this hypothesis (*23*). Pigs were chosen because their anatomy, physiology, biochemistry, genetics, size, and lifespan better resemble those of humans than mice, the previous leading model for CF (*23*). Importantly, in these CF piglets, the Welsh group observed that ASL height and sodium hyperabsorption did not differ by genotype (*21*). Instead, the ASL isolated from newborn CF pigs had reduced antibacterial activity compared to non-CF pigs against *Staphylococcus aureus,* the most common organism isolated from young children with CF (*7, 24*). Since they had previously determined that increasing salt concentration decreased antibacterial activity in human lung epithelial cultures, they tested if the same was true in the CF pig. Interestingly, when sodium and potassium concentrations in ASL collected from newborn pigs were measured, they did not differ by genotype and therefore could not explain defective bacterial killing in CF (*24*).

ASL pH had been previously proposed to differ between CF and non-CF epithelia, due to the loss of bicarbonate transport through CFTR (*21, 25, 26*). As decreased pH has also been hypothesized to affect antimicrobial activity, the Welsh group then measured ASL pH *in vivo* (directly on the trachea), *ex vivo* (collected ASL), and in primary cultured airway epithelia and found that in all preparations, CF pig ASL had a lower pH than non-CF (*24*). In support of this model, it was found that neonates with CF had a lower nasal airway-surface liquid than infants without CF (*27*). It is important to note, however, that genotype-dependent differences in the pH of nasal airway-surface liquid in older children and adults may be more variable (*9, 27*). They also found that decreasing pH in *ex vivo* ASL from non-CF pigs with HCl decreased antibacterial activity; increasing pH increased bacterial killing, indicating a pH-dependence (*24, 28*). Increasing airway CO_2 in non-CF pigs decreased ASL pH and inhibited antibacterial activity, while aerosolizing $NaHCO_3$ into the trachea of CF pigs to increase ASL pH enhanced bacterial

killing (*24*). Aerosolization of bicarbonate or other basic buffer into the airways of CF patients also increased ASL pH and improved antimicrobial activity (*29*). These experiments directly linked loss of bicarbonate secretion through CFTR to decreased ASL pH, which in turn impairs killing of bacteria that enter the lung (*24*). Additionally, it was found that decreased ASL pH leads to increased ASL viscosity, possibly through influencing mucin electrostatic interactions, consistent with previous reports of mucociliary abnormalities in CF epithelia (*20*).

The pH hypothesis was further supported by studies that determined why CF mice do not manifest lung disease while humans and pigs do. All three species rely on CFTR to secrete bicarbonate into the ASL to maintain pH, but in humans and pigs, unchecked H^+ secretion by the nongastric H^+/K^+ adenosine triphosphatase (ATP12A) decreased ASL pH and led to downstream pathophysiology including increased ASL viscosity and decreased antimicrobial activity. CF mice do not manifest lung disease because they do not express ATP12A and therefore did not have genotype-dependent differences in ASL pH. When ATP12A was inhibited chemically with ouabain in human and pig airways, defects in ASL physiology were corrected; conversely, expressing ATP12A in CF mouse airways decreased ASL pH and impaired host defenses as observed in pigs and humans (*30*). These findings are the most compelling evidence for the pH model as the basis for CF pathophysiology. While it is possible that the hydration model may play some role in the manifestation of CF, the pH model has thus far presented more clinically relevant evidence and therefore we justified our decision to test our hypothesis largely within that framework.

1.4 CURRENT AND DEVELOPING THERAPIES FOR CF

As seen with ΔF508/ΔF508, combination therapies may be required due to multiple molecular defects attributed to a single mutation, making classification and therefore specific

drug discovery difficult (*6*). Even patients with the same genotype can present variably in the clinic. Because of this, symptomatic therapies of CF are still the first line of treatment and have been shown to extend the median life expectancy of patients past 40 years. These include mucolytics like dornase-alpha, myriad oral, intravenous or inhaled antibiotics, hydrators of the airway surface such as hypertonic saline and mannitol, anti-inflammatory drugs, replacement pancreatic enzymes, and mechanical clearance of the airway mucus. To address ASL abnormalities, aerosolized mucolytics and osmotics agents are used (*6*). Another option currently being explored is aerosolizing bicarbonate and other basic buffers like tromethamine to increase ASL pH and improve bacterial killing in CF airways (*29*).

Inhibitors of other protein ion channels have been targeted to mitigate ASL physiology hypothesized to be downstream of the CFTR defect by the two models of pathophysiology. P-1037, a compound that inhibits ENaC and corrects abnormal ASL hydration is currently in phase II clinical trials. Other channels targeted for this same restoration of water and electrolyte balance in CF airways are calcium-activated chloride channels (CaCCs) such as anoctamin 1 (ANO-1, TMEM16A) (*6*). It was also discovered that using ouabain to block ATP12A in the nasal epithelia of both non-CF and CF subjects compared to control increased ASL pH (*31*). This could be a viable future strategy to address downstream effects in the pH model. However, along with symptomatic treatments, these approaches do not address the fundamental underlying defect of the disease, the mutated CFTR protein, and therefore result in an overwhelming and impractical number of medications and procedures for the average CF patient (*6*).

Gene therapy has long been pursued to correct the underlying defect of CF, as it is a monogenic disease and hypothetically, an ideal target. However, more than 200 gene therapy trials have been undertaken since the 1990s and none of these trials have resulted in US Food

and Drug Administration (FDA) approval or even shown effective clinical outcomes (*6, 8*). Delivery of the functional CFTR gene is perhaps the greatest challenge of gene therapy, as the entry of viral or non-viral vectors are largely blocked by the inherent barriers that lung epithelia have, which are exacerbated in CF patients with excess mucus and inflammation. More recently, the use of plasmid-DNA liposomes resulted in modest improvement of lung function with monthly administration in patients (*32*). The same group is also developing F/HN-pseudotyped lentiviral vectors that are preparing to begin clinical trial this year (*33*). Genome editing is another direction gene therapy is recently going in, correcting the *CFTR* gene defect by removing mutated segments of the gene using engineered nucleases and then inducing homologous recombination with the wild type gene. This approach would specifically edit mutant *CFTR* and not WT *CFTR* using techniques such as CRISP/Cas9 and specific RNA guides. Another approach is RNA editing, where single-strained antisense RNA-based oligonucleotides replace deleted mRNA segments. Repaired RNA can then be translated into wild type CFTR. There is an ongoing phase I study with QR-010, an oligonucleotide designed to repair CFTR-encoded mRNA, administered intranasally and targeting patients who are either homozygous or compound heterozygous for ΔF508. An oligonucleotide that would selectively inhibit ENaC is also in development to target other potential effectors of ASL physiology (*6*).

Small molecule-based approaches to CF have been vastly more successful than gene therapy thus far, although these treatments are mutation-specific. Because it has been demonstrated that restoring CFTR function to approximately 20–30% of the normal value is sufficient to have clinical impact, drugs targeting CF have been developed to restore just enough CFTR function to mitigate the CF phenotype (*34*). The most clinically impactful of these drugs have been potentiators and correctors of the CFTR protein.

Potentiators largely target class III and IV mutations, which are CFTR mutants with gating and conductance defects (ex: G551D) to increase anion movement (*8*). While Vertex Pharmaceutical developed a number of molecules for this purpose using high-throughput screening, VX-770 (ivacaftor/Kalydeco®) was the first CFTR potentiator to get FDA approval for use in CF patients with the G551D allele mutation (*35*). Recently, Kalydeco® was FDA approved to treat another 23 similar gating mutations (*36-38*). The mechanism by which ivacaftor increases channel open probability is not understood, but it is known that it can promote the open configuration of CFTR and restore chloride transport to G551D CFTR up to 50% of that of WT (*35*). It is also known that ivacaftor can increase phosphorylation-dependent channel gating independent of ATP and uncouples gating from ATP hydrolysis (*39-41*). Potentiators can also increase anion transport of ΔF508 CFTR if it has been trafficked to the plasma membrane (*8*). However, ivacaftor destabilizes G551D-CFTR to improve its function because it is too rigid for channel gating, and this same effect can be deleterious for other mutations that are not stable enough, such as ΔF508 CFTR. This may be why the combination of ivacaftor and CFTR correctors such as lumacaftor/Orkambi® have had modest impact in the clinic at best (*42-45*). Potentiators that do not have this destabilizing effect or may have synergy with ivacaftor are currently in development or are in clinical trial (*6*). Kalydeco® alone has demonstrated impressive clinical impact, showing statistically significant increases in forced expiratory volume in one second (FEV_1), an important marker of lung function; improved body weight and quality of life, and decreased incidence of pulmonary exacerbation in patients with a G551D allele (*46, 47*).

Correctors act directly upon the CFTR protein to correct folding defects and thereby increase productive trafficking and plasma membrane expression, primarily targeting class II or

misfolding mutations (ex: ΔF508). The primary defect in ΔF508 CFTR is a misfolded, unstable protein that is degraded within the cell before it can reach the plasma membrane. Interestingly, culturing these cells at a low temperature (26–30 °C) or using glycerol as a chemical chaperone can encourage insertion into the membrane, but these are not practical approaches in patients (*6, 8*). As with potentiators, high-throughput screening led to the discovery of several small molecules that can act upon ΔF508 CFTR and correct misfolding, most notably VX-809 (lumacaftor) and VX-661 (tezacaftor) by Vertex Pharmaceuticals (*48-50*). These correctors directly bind CFTR to increase processing efficiency and stabilize the immature protein. High-throughput screens are now being used to identify second-generation correctors that may bind different sites on CFTR and have a synergistic effect with lumacaftor or tezacaftor (*6*). As mentioned previously, combination treatments involving potentiators (such as ivacaftor) and correctors (lumacaftor and tezacaftor) are difficult to develop because of potential drug interactions. Because of this, molecules with dual activity to both correct and potentiate are currently being explored, such as aminoarylthiazoles (AATs) (*51*), 4,6,4'-trimethylangelicin (*52*) and phosphodiesterase-5 inhibitors like sildenafil and vardenafil (*53*).

Another approach is the development of proteostasis modulators that regulate the cellular environment to indirectly improve CFTR trafficking to the cell membrane and autophagy. One such compound is suberolyanilide hydroxamic acid (SAHA), which inhibits histone deacetylase and regulates the Hsp90 chaperone protein. SAHA has been shown to restore surface channel activity of ΔF508 CFTR in primary human airway epithelia to levels that are 28% of those of WT CFTR (*54*). ΔF508 CFTR exit from the endoplasmic reticulum (ER) and trafficking to the cell membrane are improved by silencing the expression of the Hsp90 c-chaperon Aha1 (*55*). Mature CFTR degradation can be prevented by inhibiting S-nitrosoglutathione reductase and

modulating Hsp70/Hsp90 organizing protein (HOP) nitrosylation (*56*). Other proteostasis modulators being developed increase autophagic flux and modulate the phosphoproteome (*6*). In epithelia with ΔF508 CFTR, protein aggregation is increased and autophagy, a key pathway of adaptation to cell-autonomous or environmental stresses, is suppressed. This results in the accumulation of autophagic substrates, which then bind to ubiquitinated ΔF508 CFTR and lead to its degradation. These deleterious changes in proteostasis are largely due to SUMOylation of the enzyme transglutaminase-2 (TG2), which leads to its constitutive activity. Interestingly, CFTR inhibition activates TG2 and inhibits autophagy, and TG2 inhibition and autophagy induction increase the abundance of functional ΔF508 CFTR. This makes TG2 and autophagy important targets for the restoration of ΔF508 CFTR processing, trafficking and stability at the membrane (*6*). In fact, restoring autophagic flux by inhibiting TG2 with proteostasis regulator cysteamine rescues ΔF508 CFTR cell surface expression for at least 24 hours after washout and restores functions in human bronchial epithelial cell lines, primary nasal cells from CF patients with ΔF508 CFTR, and in ΔF508 CF mice (*57*). Cysteamine treatment can reduce lung inflammation for several days after washout and prevents the intestinal obstruction in ΔF508 CF mice that leads to early death, suggesting that targeting autophagy with cysteamine may be a viable strategy to rescue and stabilize ΔF508 CFTR in patents (*58*). The naturally occurring polypeptide thymosin α1 has been shown to have a similar ability to restore autophagy, reduce lung inflammation and restore the function of ΔF508 CFTR in human bronchial epithelial cells and ΔF508 CF mice (*59*). More importantly, using rapamycin to stimulate autophagy also restores bacterial killing in ΔF508 CFTR epithelia, suggesting that autophagy restoration therapy could potentially reduce lung inflammation and improve pathogen clearance in CF airways (*60*).

The master protein kinase CK2 phosphorylates CFTR and can stimulate its degradation (*59*).

As such, selective inhibitors of CK2 such as CX-4945 can stabilize ΔF508 CFTR in the membrane after rescue with cysteamine (*58*). Another CK2 inhibitor, the nutraceutical epigallocatechin-gallate (EGCG), can similarly stabilize ΔF508 CFTR in the membrane after cysteamine washout for up to 48 hours in primary nasal epithelial cells and prolongs the effect of cysteamine rescue for several weeks in ΔF508/ΔF508 or ΔF508/null CF mice (*58, 61*). In phase II clinical trials with ΔF508/ΔF508 and ΔF508 compound heterozygous CF patients, the combination of cysteamine and EGCG significantly decreased reduced airway inflammation and sweat chloride concentrations (*58, 61*). Like with the corrector/potentiator approach, combination therapy with different proteostasis regulators may be a viable future treatment option for CF.

While proteostasis-based strategies may be less inherently genotype-specific as CFTR correctors and potentiators, class I mutations, which lack CFTR protein, are inherently untargetable with both of these approaches, as they require a protein substrate to act upon. One promising strategy with which to address these defects was the ribosomal read-through of premature termination codon (PTC) mutations to enable translation of the whole gene sequence and promote synthesis of the mature, full-length CFTR protein. These mutations prevent mRNA from being translated into CFTR protein, which is what leads to reduced or absent CFTR production. It has been shown that aminoglycoside antibiotics and derivatives like gentamicin or NB124 can promote a "read-through" of these PTCs in CFTR mRNA with class I mutations. These compounds were promising in cell cultures and CF mouse models but eventually failed to improve cell surface expression in human clinical trials (*62, 63*). Additionally, aminoglycosides can be highly toxic, so alternative molecules were sought with high-throughput screening, which led to the discovery of the nontoxic PTC124 or Ataluren by PTC Therapeutics, Inc. Ataluren can

read through PTCs specifically, not natural stop codons, and promote protein production in both a dystrophin-deficient (Duchenne's) and G542X CF mouse model (*64*). In a phase II clinical trial, 23 adult CF patients with heterozygous nonsense mutations were treated with ataluren for two 2-week cycles and nasal potential difference (NPD) was measured. Mean CFTR-dependent chloride transport in these patients normalized in more than half of the patients, and the drug was safe and well tolerated with minimal side effects (*65*). Another study in pediatric patients found that ataluren reduces electrophysiological abnormalities in children with CFTR nonsense mutations (*66*). Unfortunately in a double blind, placebo-controlled, 48-week phase III clinical trial comparing ataluren to placebo in nonsense mutation CF patients, the drug failed to produce statistically significant differences between the two study populations in absolute change in percent-predicted FEV_1 or in rate of pulmonary exacerbations. As such, PTC has discontinued current clinical development of ataluren in cystic fibrosis, leaving this class of mutations without a viable therapeutic candidate (*67*).

1.5 EFFORTS TO DEVELOP ANION-PERMEABLE CHANNELS FOR CF

There has previously been extensive work developing synthetic ionophores, both small molecule and peptide-based, with a main focus on chloride transport and developing cystic fibrosis therapeutics. The general strategy was to reduce pathophysiology by opening alternative, non-CFTR anion pathways to compensate for the CFTR channel defect. In 1996, El-Etri et al first tested if anions can increase the permeability of epithelia to anions using 5,10,15,20-Tetraphenyl-21H,23H-porphine manganese(III) chloride (TPPMn(III)), a positively charged lipophilic anion carrier selective for chloride over other halides. TPPMn(III) did increase anion permeability of cultured mouse lung epithelia (MLE) as measured by short-circuit current (I_{sc}) to a level similar to that of CFTR activation induced by forskolin analogues (*68*). However, since

this molecule was tested in non-CF epithelia, it is unclear if it actually acts independently of CFTR to increase chloride conductance.

Tomich and coworkers in the late 1990s and early 2000s developed a series of channel-forming peptides with the core M2GlyR, corresponding to a domain proposed to line the pore of the ligand-gated chloride channel. Application of C-K4-M2GlyR to cultured human colonic epithelia from the T84 cell line increased I_{sc} and caused fluid secretion, which could be inhibited by chloride channel blockers, bumetanide and the removal of external chloride. They concluded that membrane insertion of C-K4-M2GlyR and the subsequent anion conductance might functionally mimic CFTR (*69*). A subsequent study determined if restoration of chloride transport would also restore glutathione secretion, a major antioxidant in the epithelial lung lining fluid, reported to be decreased in the apical fluid of CF airway epithelia. Another peptide with the M2GlyR core that also forms chloride channels, N-K_4-M2GlyR, and a K^+ channel activator (chlorzoxazone) increased bumetanide-sensitive I_{sc}, and glutathione efflux, measured by high-performance liquid chromatography (HPLC), in CFT1 cultured epithelia. They concluded that glutathione efflux occurs in tandem with apical chloride secretion, and that these could be restored independently of CFTR (*70*). Nasal potential difference (PD) studies were also performed in ΔF508 homozygous transgenic mice treated with CK4-M2GlyR or NK4-M2GlyR. Treated CF nasal epithelia were found to respond to cAMP-agonist isoproterenol to more similarly to that of WT animals than to untreated CF epithelia, and sustained chloride conductance was observed for up to 6 hours after a single peptide treatment (*71*). It is unclear if these promising studies are still being pursued.

In 2001, Jiang et al reported increased chloride transport with GL-172, a synthetic analog of squalamine in immortalized tracheobronchial epithelial cells derived from a ΔF508 patient

(CFT1), as measured by the Cl^--sensitive fluorescent indicator SPQ and patch clamp. Studies of normal human lung epithelia (NHBE) in an Ussing chamber showed an increase in I_{sc} with addition of GL-172 that was 30% of that observed with cAMP agonist-activated CFTR. The magnitude of this change in short-circuit current was ~30% of that attained when CFTR was maximally stimulated with cAMP agonists. Administration of GL-172 to the nasal epithelium of gut-corrected $CFTR^{-/-}$ mice (FABP-$CFTR^{-/-}$) caused hyperpolarization, indicating increased anion permeability and restoration of Cl^- secretion (*72*). While promising, the studies relevant for translation were only carried out in normal lung epithelia or in $CFTR^{-/-}$ mice, which do not manifest typical CF lung disease, making them an non-ideal animal model for testing this hypothesis.

The Davis group has developed several classes of small molecule-based anion transporters, including the "cholapods" in 2003. These are shown to increase chloride efflux from liposomes, and increase I_{sc} across cultured Madin Darby canine kidney (MDCK) epithelia in an Ussing chamber. This response was found to be different from that induced by activating native chloride channels in the MDCK epithelia. A recent study from this group evaluated another fifteen anionophores in similar fashion, with anion transport from single cells assayed with a novel fluorescence technique and electrophysiology once again measured by Ussing chamber (*73*). While the breadth of work from the Davis group is indeed impressive, none have thus far translated past electrophysiological changes *in vitro* and it is unclear if they will have any kind of clinical impact.

In 2012, the Yang group developed a synthetic compound that transports chloride across lipid membranes and exhibits single-channel currents by patch clamp that confirm formation of ion channels in liposomes. They then studied this compound in CuFi-8 and NuLi cell lines derived

from a ΔF508/ΔF508 and WT patient, respectively, and found that whole-cell currents were increased in the first few minutes, and sustained for 15 minutes. The current increase persisted even after washing with control buffer for 30 minutes. Most interestingly, compound addition resulted in an even larger increase in CuFi-8 cells than activating WT CFTR in the NuLi cells with forskolin did, while CuFi-8 cells showed no response to forskolin. This indicates that the compound can increase chloride conductance via a non-CFTR pathway (*74*). Again, it is unclear if this promising compound is being pursued in higher organisms, but the Yang group is actively developing other small molecule synthetic channels (*75*).

The Gale group is also actively developing small molecules that can transport anions. They are exploring derivatives of the small molecule natural product prodigiosin, which is known to facilitate the co-transport HCl and exchange of chloride across lipid bilayers. They used ion-selective electrodes to determine that prodigiosin and derivatives can efflux chloride from POPC-based liposomes in the presence of external nitrate or bicarbonate anions. This anion exchange required the presence of a less hydrophilic anion on the outside of the liposomes. They then used a ^{13}C NMR-based assay to determine that these small molecules can facilitate Cl^-/HCO_3^- exchange similar to that observed with the anion exchanger (AE2) protein. Notably, prodigiosin is better at this exchange than its derivatives (*76*). The Gale group studies anion transporters for several different purposes, and this would be a highly interesting molecule to see translate to animal studies.

1.6 THE PROSPECT OF MOLECULAR PROSTHETICS

Robustness is an inherent property of living systems, meaning that organisms have the ability to largely maintain function despite a range of perturbations, such as environmental change or and genetic variation (*77-80*). For example, most humans are missing ~20 proteins yet have no

disease phenotype (*77*), and some people with mutations that typically cause catastrophic Mendelian diseases live symptom-free (*79*). Such resilience is attributed to a variety of mechanisms (*78, 80*), including networks of collaborating proteins (*81*) that typically provide more functional capacity than required for physiology (Fig. 1.2, left). However, in some cases these mechanisms are insufficient to maintain physiology, and the capacity for an important function drops below the required threshold. This can lead to a dramatic phenotype, such as lack of growth in a cell or disease in a patient. In such cases all possible robustness mechanisms are likely engaged and a substantial level of functional capacity may still be retained, lessening the gap in functional capacity that needs to be filled. (Fig. 1.2, middle).

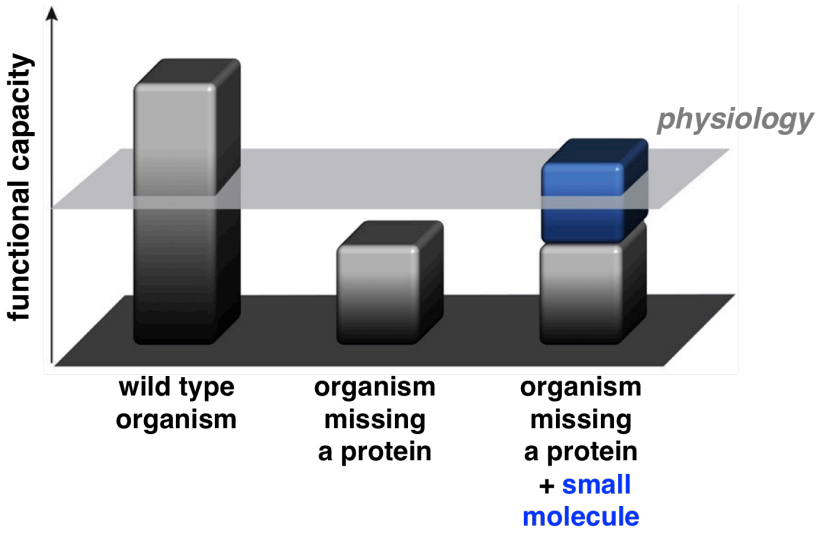

Figure 1.2 The prospect of molecular prosthetics. The robustness of living systems suggests small molecules that only partially mimic the function of missing proteins may be sufficient to restore physiology.

The concept of robustness and residual function suggests that in cases where an important protein is missing, even imperfect replication of its function may be sufficient to restore physiology. It became increasingly clear to us that many human diseases caused by the loss of protein function remain incurable, and based on our experience and skillset we knew that we wanted to come at the problem with a small molecule-based approach. Small molecules have

many features that can make them exceptionally effective as therapeutics. Relative to proteins and oligonucleotides, they are generally more evasive of the immune system, inert to peripheral metabolism, cell permeable, orally bioavailable, and cost effective to produce, purify, and store. Importantly, just as artificial limbs replace the physical function of a missing arm or leg, we hypothesized that small molecule surrogates acting as prosthetics on the molecular scale could replace protein functions that are either dysfunctional or absent in humans. Perfectly replicating protein function is challenging, especially with a small molecule that may at best mimic one of two functions of a multifunctional protein. However, the concept of robustness allows for this kind of imperfection, because like an artificial limb, a molecular prosthetic could build upon and interface with the existing architecture and residual function of the organism to restore normal physiology (Fig. 1.2, right).

The molecular prosthetics concept within the framework of channelopathies and related ion transporter deficiencies relies heavily on the idea of a residual network of pumps and channels that remain active despite the missing protein and a subsequent build up of an ion gradient across lipid membranes that could be harnessed by a passive small molecule channel or transporter. Molecular prosthetics have already been shown to restore whole-animal physiology in disease models with a deficiency of iron-transporting protein function that abolishes transmembrane iron flux. In these models, iron gradients build up across protein-deficient membranes due to the residual action of other iron-transport proteins in the network. My colleagues Tony Grillo and Anna SantaMaria found that the small molecule natural product, hinokitiol, can release these gradients to restore iron transport into, within, and/or out of cells. Hinokitiol promotes gut iron absorption in animal models of divalent metal transporter 1 (DMT1) and ferroportin deficiencies, as well as hemoglobinization in DMT1-and mitoferrin-deficient zebrafish (*82*). Their findings

suggest that small molecule prosthetics that partially mimic the function of missing protein ion channels or transporters may have potential in treating human diseases. Unfortunately, hinokitiol only transports divalent metals (*82*), so another molecular prosthetic would need to be developed for cystic fibrosis.

In human lungs, there are several ion channels responsible for maintaining the normal ion gradient across the lung epithelium that could potentially functionally interface with a molecular prosthetic to rescue CF pathophysiology. Bicarbonate import through the basolateral membrane of epithelia is primarily driven by a sodium gradient created by Na^+/K^+ ATPase. The Na^+/H^+ exchanger (NHE1) provides the cytosolic sodium necessary to fuel the Na^+/K^+ ATPase and works in collaboration with anion exchanger 2 (AE2) to maintain cytoplasmic pH (pH_i). NHE1 is activated by acidic pH_i to extrude excess acid, while AE2 is activated by alkaline pH_i to extrude excess base. Na^+-HCO_3^- cotransporter 1 (NBC1) is the major basolateral bicarbonate uptake transport, which uses the sodium gradient generated by the Na^+/K^+ ATPase to provide adequate bicarbonate accumulation in the cytoplasm. The vacuolar-type H^+-ATPase pump and the H^+-K^+-ATPase pump in the basolateral membrane can generate steep inward H+ gradients and interface with NBC1 to dramatically increase HCO_3^- loading of the cell (*83*). These mechanisms would help create the gradient that a molecular prosthetic could release to restore bicarbonate secretion. Examples of proteins that may help to balance over-permeabilization or relatively unselective ion transport by molecular prosthetics by effluxing excess ions could include AE2, K^+ leak channels, calcium-activated chloride channels (CaCC), and outward-rectifying chloride channels (ORCC) (*83*). These ion channels and pumps collectively represent an endogenous protein network with the potential to functionally interface with an imperfect small molecule mimic of the missing CFTR anion channel to restore physiology in lung epithelia.

1.7 AMB PRIMARILY KILLS YEAST BY SIMPLY BINDING STEROL

Fortunately, nature has already provided a small molecule ion channel prototype for us to potentially test our molecular prosthetics hypothesis in a CF model. Amphotericin B (AmB) is a small molecule natural product used in the clinic as an antifungal for almost 60 years. It is known to self-assemble into nonspecific ion channels in sterol-containing lipid membranes that have been shown to transport both cations and anions (*84, 85*). Planar lipid bilayer studies performed in our lab revealed that the single ion channel trace of AmB exhibits an opening and closing pattern similar to that of a protein ion channel (*86*). Despite the remarkable ability of AmB to form ion channels, it remained a non-ideal candidate for testing our hypothesis, as it has long been believed that AmB kills cells via ion channel-mediated membrane permeabilization (*87-93*). To use AmB as a probe, our first task was to determine if channel formation and membrane permeabilization was indeed its mechanism of toxicity, and if there was some way to separate the channel-forming capacity from cell killing.

The first step was the development of AmB derivatives that test different hypothesis regarding sterol binding and channel formation, via site-specific deletions of functional groups predicted to play specific roles in the aforementioned activities. Several groups had previously determined that the presence of sterols is required for membrane interaction and channel formation (*84, 87, 88, 91*), so it was hypothesized that sterol binding was in fact the killing mechanism of AmB. The C41 carboxylate and mycosamine sugar appendages were hypothesized to promote the direct binding of membrane-embedded sterols (*94-96*), and so in the first derivative developed, amphoteronolide B (AmdeB), the mycosamine sugar appendage was removed (*96*).

The second derivative developed was C35deOAmB, where a single oxygen atom was

removed from the C35 position (*97*). This was rationally designed using both leading models for the structure of the AmB ion channel. The hydroxyl group at C35 is predicted to be critical for channel formation, either by anchoring the channel to one side of the lipid bilayer in the single barrel stave model or by connecting two barrel-shaped aggregates together into a membrane-spanning channel in the double barrel stave model (*98*). These two molecules served as important probes in determining the killing mechanism of AmB and if cell killing and channel formation could be separable.

Isothermal calorimetry was then used to test the binding of these molecules with ergosterol, the essential sterol in the yeast membrane, where an increase in isotherm is consistent with binding. Liposomes with or without 10% ergosterol were titrated into a chamber containing AmB, AmdeB, or C35deOAmB in buffer. As a negative control, no increase in isotherm was observed with any of the three molecules with sterol-free liposomes. As expected, an increase in isotherm was observed with AmB in the presence of sterol-containing liposomes, consistent with literature precedent of AmB's sterol binding capacity, whereas no increase in isotherm was observed with AmdeB. This indicates that loss of the mycosamine sugar results in a complete inability to bind ergosterol. In contrast, C35deOAmB fully retains sterol-binding ability, exhibiting an increase in isotherm commensurate with that of the original AmB molecule (*97*). To then determine channel-forming capacity of these molecules, potassium efflux was measured either in sterol-containing liposomes or *Saccharomyces cerevisiae* yeast. Importantly, AmB caused robust efflux of potassium ions, but both AmdeB and C35deOAmB did not (*97*). This led to the conclusion that AmdeB and C35deOAmB are both unable to form channels.

With sterol binding and channel-forming activity known, the minimum inhibitory concentration (MIC) of these compounds was tested against both *Saccharomyces cerevisiae* and

Candida albicans. It was found that consistent with its inability to bind sterols, AmdeB was unable to kill the yeast at any tested concentration. However, despite losing its channel-forming ability, C35deOAmB remains potent against both yeast strains like the original AmB molecule. Notably, C35deOAmB remains fungicidal like the original molecule, as observed in a killing kinetics assay versus AmB and ketoconazole, a fungistatic drug. Another important finding was that at the MIC, there are more AmB molecules than ergosterol molecules, suggesting that the stoichiometric ratio of the two plays a key role in toxicity (*97*). Because C35deOAmB cannot form channels but still binds sterols and potently kills yeast, our lab concluded that the binding of essential sterols is actually the primary mechanism of cell killing by AmB, not channel formation. This represented the first hint to us that the channel-forming capacity could indeed be separated from cell killing. Because AmB is only toxic when there are more AmB molecules present than ergosterol molecules, we could potentially use a low concentration of AmB as a nontoxic ion channel surrogate.

1.8 OUTLOOK

We now have an extensive understanding of what is currently known about the pathophysiology of CF and current therapies, as well as a model framework within which to test our hypothesis. This dissertation will determine if even an unregulated and non-selective small molecule ion channel could functionally interface with the endogenous protein network to increase bicarbonate transport and ASL pH, thereby restoring downstream physiology in CF epithelia. Herein, the characterization of a potential molecular prosthetic, AmB, is detailed from greater structural understanding, yeast model studies, to studies in CF primary epithelia and porcine model.

1.9 REFERENCES

1. B. J. Druker *et al.*, Efficacy and Safety of a Specific Inhibitor of the BCR-ABL Tyrosine Kinase in Chronic Myeloid Leukemia. *New England Journal of Medicine* **344**, 1031-1037 (2001).
2. S. Okada, J. S. O'Brien, Tay-Sachs disease: generalized absence of a beta-DN-acetylhexosaminidase component. *Science* **165**, 698-700 (1969).
3. J. Kint, Fabry's disease: alpha-galactosidase deficiency. *Science* **167**, 1268-1269 (1970).
4. A. Cao, R. Galanello, Beta-thalassemia. *Genetics In Medicine* **12**, 61 (2010).
5. C. A. Hübner, T. J. Jentsch, Ion channel diseases. *Human molecular genetics* **11**, 2435-2445 (2002).
6. L. Maiuri, V. Raia, G. Kroemer, Strategies for the etiological therapy of cystic fibrosis. *Cell Death Differ* **24**, 1825-1844 (2017).
7. D. A. Stoltz *et al.*, Cystic fibrosis pigs develop lung disease and exhibit defective bacterial eradication at birth. *Sci Transl Med* **2**, 29ra31 (2010).
8. M. P. Rogan, D. A. Stoltz, D. B. Hornick, Cystic Fibrosis Transmembrane Conductance Regulator Intracellular Processing, Trafficking, and Opportunities for Mutation-Specific Treatment. *Chest* **139**, 1480-1490 (2011).
9. D. A. Stoltz , D. K. Meyerholz , M. J. Welsh Origins of Cystic Fibrosis Lung Disease. *New England Journal of Medicine* **372**, 351-362 (2015).
10. W. B. Guggino, Cystic fibrosis and the salt controversy. *Cell* **96**, 607-610 (1999).
11. R. Tarran *et al.*, The CF salt controversy: in vivo observations and therapeutic approaches. *Mol Cell* **8**, 149-158 (2001).
12. R. Tarran, Regulation of airway surface liquid volume and mucus transport by active ion transport. *Proceedings of the American Thoracic Society* **1**, 42-46 (2004).
13. R. C. Boucher, Evidence for airway surface dehydration as the initiating event in CF airway disease. *J Intern Med* **261**, 5-16 (2007).
14. R. C. Boucher, Cystic fibrosis: a disease of vulnerability to airway surface dehydration. *Trends in molecular medicine* **13**, 231-240 (2007).
15. C. Lu, C. Jiang, S. Pribanic, D. Rotin, CFTR stabilizes ENaC at the plasma membrane. *J Cyst Fibros* **6**, 419-422 (2007).
16. B. K. Berdiev, Y. J. Qadri, D. J. Benos, Assessment of the CFTR and ENaC association. *Mol Biosyst* **5**, 123-127 (2009).
17. J. F. Collawn, A. Lazrak, Z. Bebok, S. Matalon, The CFTR and ENaC debate: how important is ENaC in CF lung disease? *Am J Physiol Lung Cell Mol Physiol* **302**, L1141-1146 (2012).
18. A. Livraghi-Butrico *et al.*, Loss of Cftr function exacerbates the phenotype of Na(+) hyperabsorption in murine airways. *Am J Physiol Lung Cell Mol Physiol* **304**, L469-480 (2013).
19. O. A. Itani *et al.*, Human cystic fibrosis airway epithelia have reduced Cl− conductance but not increased Na+ conductance. *Proceedings of the National Academy of Sciences* **108**, 10260-10265 (2011).
20. X. X. Tang *et al.*, Acidic pH increases airway surface liquid viscosity in cystic fibrosis. *J Clin Invest* **126**, 879-891 (2016).
21. J. H. Chen *et al.*, Loss of anion transport without increased sodium absorption characterizes newborn porcine cystic fibrosis airway epithelia. *Cell* **143**, 911-923 (2010).

22. J. J. Smith, S. M. Travis, E. P. Greenberg, M. J. Welsh, Cystic fibrosis airway epithelia fail to kill bacteria because of abnormal airway surface fluid. *Cell* **85**, 229-236 (1996).
23. C. S. Rogers *et al.*, Disruption of the CFTR gene produces a model of cystic fibrosis in newborn pigs. *Science* **321**, 1837-1841 (2008).
24. A. A. Pezzulo *et al.*, Reduced airway surface pH impairs bacterial killing in the porcine cystic fibrosis lung. *Nature* **487**, 109-113 (2012).
25. R. D. Coakley *et al.*, Abnormal surface liquid pH regulation by cultured cystic fibrosis bronchial epithelium. *Proceedings of the National Academy of Sciences of the United States of America* **100**, 16083-16088 (2003).
26. J. J. Smith, M. J. Welsh, cAMP stimulates bicarbonate secretion across normal, but not cystic fibrosis airway epithelia. *Journal of Clinical Investigation* **89**, 1148 (1992).
27. M. H. A. Alaiwa *et al.*, Neonates with cystic fibrosis have a reduced nasal liquid pH; a small pilot study. *Journal of cystic fibrosis* **13**, 373-377 (2014).
28. M. H. Abou Alaiwa *et al.*, pH modulates the activity and synergism of the airway surface liquid antimicrobials beta-defensin-3 and LL-37. *Proc Natl Acad Sci U S A* **111**, 18703-18708 (2014).
29. M. H. Abou Alaiwa *et al.*, Repurposing tromethamine as inhaled therapy to treat CF airway disease. *JCI Insight* **1**, (2016).
30. V. S. Shah *et al.*, Airway acidification initiates host defense abnormalities in cystic fibrosis mice. *Science* **351**, 503-507 (2016).
31. V. S. Shah, University of Iowa, (2017).
32. E. W. Alton *et al.*, A phase I/IIa safety and efficacy study of nebulized liposome-mediated gene therapy for cystic fibrosis supports a multidose trial. *American journal of respiratory and critical care medicine* **192**, 1389-1392 (2015).
33. E. W. Alton *et al.*, Preparation for a first-in-man lentivirus trial in patients with cystic fibrosis. *Thorax* **72**, 137-147 (2017).
34. G. R. Cutting, Cystic fibrosis genetics: from molecular understanding to clinical application. *Nat Rev Genet* **16**, 45-56 (2015).
35. F. Van Goor *et al.*, Rescue of CF airway epithelial cell function in vitro by a CFTR potentiator, VX-770. *Proceedings of the National Academy of Sciences* **106**, 18825-18830 (2009).
36. F. Van Goor, H. Yu, B. Burton, B. J. Hoffman, Effect of ivacaftor on CFTR forms with missense mutations associated with defects in protein processing or function. *Journal of Cystic Fibrosis* **13**, 29-36 (2014).
37. K. De Boeck *et al.*, Efficacy and safety of ivacaftor in patients with cystic fibrosis and a non-G551D gating mutation. *J Cyst Fibros* **13**, 674-680 (2014).
38. M. Partridge, E. Rojas, Z. Barber. (Vertex Pharmaceuticals Incorporated, Business Wire, 2017).
39. H. Yu *et al.*, Ivacaftor potentiation of multiple CFTR channels with gating mutations. *J Cyst Fibros* **11**, 237-245 (2012).
40. P. D. Eckford, C. Li, M. Ramjeesingh, C. E. Bear, CFTR potentiator VX-770 (ivacaftor) opens the defective channel gate of mutant CFTR in a phosphorylation-dependent but ATP-independent manner. *Journal of Biological Chemistry*, jbc. M112. 393637 (2012).
41. K.-Y. Jih, T.-C. Hwang, Vx-770 potentiates CFTR function by promoting decoupling between the gating cycle and ATP hydrolysis cycle. *Proceedings of the National Academy of Sciences* **110**, 4404-4409 (2013).

42. C. E. Wainwright *et al.*, Lumacaftor–Ivacaftor in Patients with Cystic Fibrosis Homozygous for Phe508del CFTR. *New England Journal of Medicine* **373**, 220-231 (2015).
43. D. M. Cholon *et al.*, Potentiator ivacaftor abrogates pharmacological correction of DeltaF508 CFTR in cystic fibrosis. *Sci Transl Med* **6**, 246ra296 (2014).
44. G. Veit *et al.*, Some gating potentiators, including VX-770, diminish DeltaF508-CFTR functional expression. *Sci Transl Med* **6**, 246ra297 (2014).
45. D. Holmes, in *Nat Rev Drug Discov*. (England, 2014), vol. 13, pp. 713-714.
46. B. W. Ramsey *et al.*, A CFTR Potentiator in Patients with Cystic Fibrosis and the G551D Mutation. *New England Journal of Medicine* **365**, 1663-1672 (2011).
47. F. J. Accurso *et al.*, Effect of VX-770 in persons with cystic fibrosis and the G551D-CFTR mutation. *New England Journal of Medicine* **363**, 1991-2003 (2010).
48. H. Y. Ren *et al.*, VX-809 corrects folding defects in cystic fibrosis transmembrane conductance regulator protein through action on membrane-spanning domain 1. *Mol Biol Cell* **24**, 3016-3024 (2013).
49. J. L. Taylor-Cousar *et al.*, Tezacaftor–Ivacaftor in Patients with Cystic Fibrosis Homozygous for Phe508del. *New England Journal of Medicine*, (2017).
50. M. Partridge, E. Rojas, Z. Barber. (Vertex Pharmaceuticals Incorporated, Business Wire, 2017).
51. N. Pedemonte *et al.*, Dual activity of aminoarylthiazoles on the trafficking and gating defects of the cystic fibrosis transmembrane conductance regulator chloride channel caused by cystic fibrosis mutations. *Journal of Biological Chemistry* **286**, 15215-15226 (2011).
52. O. Laselva, S. Molinski, V. Casavola, C. E. Bear, The investigational Cystic Fibrosis drug Trimethylangelicin directly modulates CFTR by stabilizing the first membrane-spanning domain. *Biochemical pharmacology* **119**, 85-92 (2016).
53. B. Lubamba *et al.*, Preclinical evidence that sildenafil and vardenafil activate chloride transport in cystic fibrosis. *American journal of respiratory and critical care medicine* **177**, 506-515 (2008).
54. D. M. Hutt *et al.*, Reduced histone deacetylase 7 activity restores function to misfolded CFTR in cystic fibrosis. *Nature chemical biology* **6**, 25-33 (2010).
55. X. Wang *et al.*, Hsp90 cochaperone Aha1 downregulation rescues misfolding of CFTR in cystic fibrosis. *Cell* **127**, 803-815 (2006).
56. K. Zaman *et al.*, Augmentation of CFTR maturation by S-nitrosoglutathione reductase. *American Journal of Physiology-Lung Cellular and Molecular Physiology* **310**, L263-L270 (2016).
57. A. Luciani *et al.*, Targeting autophagy as a novel strategy for facilitating the therapeutic action of potentiators on ΔF508 cystic fibrosis transmembrane conductance regulator. *Autophagy* **8**, 1657-1672 (2012).
58. D. D. Stefano *et al.*, Restoration of CFTR function in patients with cystic fibrosis carrying the F508del-CFTR mutation. *Autophagy* **10**, 2053-2074 (2014).
59. S. Luz *et al.*, LMTK2-mediated phosphorylation regulates CFTR endocytosis in human airway epithelial cells. *Journal of Biological Chemistry* **289**, 15080-15093 (2014).
60. R. D. Junkins, C. McCormick, T.-J. Lin, The emerging potential of autophagy-based therapies in the treatment of cystic fibrosis lung infections. *Autophagy* **10**, 538-547 (2014).

61. A. Tosco *et al.*, A novel treatment of cystic fibrosis acting on-target: cysteamine plus epigallocatechin gallate for the autophagy-dependent rescue of class II-mutated CFTR. *Cell Death & Differentiation* **23**, 1380-1393 (2016).
62. X. Xue *et al.*, Synthetic aminoglycosides efficiently suppress cystic fibrosis transmembrane conductance regulator nonsense mutations and are enhanced by ivacaftor. *American journal of respiratory cell and molecular biology* **50**, 805-816 (2014).
63. J. P. Clancy *et al.*, No detectable improvements in cystic fibrosis transmembrane conductance regulator by nasal aminoglycosides in patients with cystic fibrosis with stop mutations. *American journal of respiratory cell and molecular biology* **37**, 57-66 (2007).
64. M. Du *et al.*, PTC124 is an orally bioavailable compound that promotes suppression of the human CFTR-G542X nonsense allele in a CF mouse model. *Proceedings of the National Academy of Sciences* **105**, 2064-2069 (2008).
65. E. Kerem *et al.*, Effectiveness of PTC124 treatment of cystic fibrosis caused by nonsense mutations: a prospective phase II trial. *The Lancet* **372**, 719-727 (2008).
66. I. Sermet-Gaudelus *et al.*, Ataluren (PTC124) Induces CFTR Protein Expression and Activity in. *J Med* **354**, 229-240 (2006).
67. . (PTC Therapeutics, Inc, PRNewswire).
68. M. El-Etri, J. Cuppoletti, Metalloporphyrin chloride ionophores: induction of increased anion permeability in lung epithelial cells. *Am J Physiol* **270**, L386-392 (1996).
69. D. Wallace *et al.*, A synthetic peptide derived from glycine-gated Cl-channel induces transepithelial Cl-and fluid secretion. *American Journal of Physiology-Cell Physiology* **272**, C1672-C1679 (1997).
70. L. Gao *et al.*, Synthetic chloride channel restores glutathione secretion in cystic fibrosis airway epithelia. *American Journal of Physiology-Lung Cellular and Molecular Physiology* **281**, L24-L30 (2001).
71. J. M. Tomich, U. Bukovnik, J. Layman, B. D. Schultz, in *Cystic Fibrosis-Renewed Hopes Through Research*. (InTech, 2012).
72. C. Jiang *et al.*, Partial correction of defective Cl(-) secretion in cystic fibrosis epithelial cells by an analog of squalamine. *Am J Physiol Lung Cell Mol Physiol* **281**, L1164-1172 (2001).
73. H. Li *et al.*, Efficient, non-toxic anion transport by synthetic carriers in cells and epithelia. *Nat Chem* **8**, 24-32 (2016).
74. B. Shen, X. Li, F. Wang, X. Yao, D. Yang, A synthetic chloride channel restores chloride conductance in human cystic fibrosis epithelial cells. *PLoS One* **7**, e34694 (2012).
75. P.-Y. Liu *et al.*, A small synthetic molecule functions as a chloride–bicarbonate dual-transporter and induces chloride secretion in cells. *Chemical Communications* **52**, 7380-7383 (2016).
76. J. T. Davis *et al.*, Using small molecules to facilitate exchange of bicarbonate and chloride anions across liposomal membranes. *Nat Chem* **1**, 138-144 (2009).
77. D. G. MacArthur *et al.*, A systematic survey of loss-of-function variants in human protein-coding genes. *Science* **335**, 823-828 (2012).
78. J. L. Hartman, B. Garvik, L. Hartwell, Principles for the buffering of genetic variation. *Science* **291**, 1001-1004 (2001).
79. S. H. Friend, E. E. Schadt, Clues from the resilient. *Science* **344**, 970-972 (2014).
80. J. Stelling, U. Sauer, Z. Szallasi, F. J. Doyle, J. Doyle, Robustness of cellular functions. *Cell* **118**, 675-685 (2004).

81. E. Gouaux, R. Mackinnon, Principles of selective ion transport in channels and pumps. *Science* **310**, 1461-1465 (2005).
82. A. S. Grillo *et al.*, Restored iron transport by a small molecule promotes absorption and hemoglobinization in animals. *Science* **356**, 608-616 (2017).
83. M. G. Lee, E. Ohana, H. W. Park, D. Yang, S. Muallem, Molecular mechanism of pancreatic and salivary gland fluid and HCO3 secretion. *Physiol Rev* **92**, 39-74 (2012).
84. L. N. Ermishkin, K. M. Kasumov, V. M. Potzeluyev, Single ionic channels induced in lipid bilayers by polyene antibiotics amphotericin B and nystatine. *Nature* **262**, 698-699 (1976).
85. L. N. Ermishkin, K. M. Kasumov, V. M. Potseluyev, Properties of amphotericin B channels in a lipid bilayer. *Biochim Biophys Acta* **470**, 357-367 (1977).
86. S. A. Davis *et al.*, C3-OH of Amphotericin B Plays an Important Role in Ion Conductance. *J Am Chem Soc* **137**, 15102-15104 (2015).
87. A. Finkelstein, R. Holz, Aqueous pores created in thin lipid membranes by the polyene antibiotics nystatin and amphotericin B. *Membranes* **2**, 377-408 (1973).
88. T. E. Andreoli, THE STRUCTURE AND FUNCTION OF AMPHOTERICIN B‐CHOLESTEROL PORES IN LIPID BILAYER MEMBRANES. *Annals of the New York Academy of Sciences* **235**, 448-468 (1974).
89. J. Bolard, How do the polyene macrolide antibiotics affect the cellular membrane properties? *Biochimica et Biophysica Acta (BBA)-Reviews on Biomembranes* **864**, 257-304 (1986).
90. M. Murata *et al.*, Ion channel complex of antibiotics as viewed by NMR. *Pure and Applied Chemistry* **81**, 1123-1129 (2009).
91. B. de Kruijff, R. A. Demel, Polyene antibiotic-sterol interactions in membranes of Acholeplasma laidlawii cells and lecithin liposomes. 3. Molecular structure of the polyene antibiotic-cholesterol complexes. *Biochim Biophys Acta* **339**, 57-70 (1974).
92. M. Baginski, H. Resat, E. Borowski, Comparative molecular dynamics simulations of amphotericin B-cholesterol/ergosterol membrane channels. *Biochim Biophys Acta* **1567**, 63-78 (2002).
93. A. A. Volmer, A. M. Szpilman, E. M. Carreira, Synthesis and biological evaluation of amphotericin B derivatives. *Nat Prod Rep* **27**, 1329-1349 (2010).
94. M. Chéron *et al.*, Quantitative structure-activity relationships in amphotericin B derivatives. *Biochem Pharmacol* **37**, 827-836 (1988).
95. N. Matsumori, Y. Sawada, M. Murata, Mycosamine orientation of amphotericin B controlling interaction with ergosterol: sterol-dependent activity of conformation-restricted derivatives with an amino-carbonyl bridge. *Journal of the American Chemical Society* **127**, 10667-10675 (2005).
96. D. S. Palacios, I. Dailey, D. M. Siebert, B. C. Wilcock, M. D. Burke, Synthesis-enabled functional group deletions reveal key underpinnings of amphotericin B ion channel and antifungal activities. *Proc Natl Acad Sci U S A* **108**, 6733-6738 (2011).
97. K. C. Gray *et al.*, Amphotericin primarily kills yeast by simply binding ergosterol. *Proc Natl Acad Sci U S A* **109**, 2234-2239 (2012).
98. P. Van Hoogevest, B. De Kruijff, Effect of amphotericin B on cholesterol-containing liposomes of egg phosphatidylcholine and didocosenoyl phosphatidylcholine. A refinement of the model for the formation of pores by amphotericin B in membranes. *Biochimica et Biophysica Acta (BBA)-Biomembranes* **511**, 397-407 (1978).

CHAPTER 2

CHARACTERIZATION OF AMPHOTERICIN B AS A POTENTIAL MOLECULAR PROSTHETIC

Robust networks of pumps and channels are generally responsible for the directional movement of specific ions in organisms ranging from microbes to humans, and deficiencies of these protein ion channels underlie many currently incurable human diseases. This understanding led us to question whether minimally selective small molecule mimics of missing protein channels might be capable of collaborating with the corresponding protein ion pumps to restore physiology. One such ion channel-forming small molecule, amphotericin B (AmB), has remained the powerful but highly toxic last line of defense in treating life-threatening fungal infections in humans for nearly six decades with minimal development of microbial resistance. Understanding how this small molecule kills yeast is critical for determining if its intriguing ability to autonomously form ion channels in lipid membranes could potentially be used to replace protein ion channels in diseases where they are deficient or missing, while avoiding unwanted toxicity.

In the widely accepted ion channel model for its mechanism of cytocidal action, AmB forms aggregates inside lipid bilayers that permeabilize and kill cells. In contrast, we report that AmB exists primarily in the form of large, extramembranous aggregates that kill yeast by extracting ergosterol from lipid bilayers. These findings reveal that extraction of a polyfunctional lipids like sterol underlies the resistance-refractory antimicrobial action of AmB and suggests a roadmap for separating its cytocidal and membrane-permeabilizing activities. This new mechanistic understanding first guided the usage of the AmB channel as a molecular surrogate for missing protein ion channels in a mutant yeast strain missing a potassium transporter. We report vigorous

and sustainable restoration of yeast cell growth by replacing the missing protein ion transporters with AmB acting as an imperfect small molecule mimic. We further provide evidence that this tolerance for imperfect mimicry is attributable to collaboration between the channel-forming small molecule and protein ion pumps. These results illuminate a mechanistic framework for pursuing small molecule replacements for deficient protein ion channels that underlie a range of challenging human diseases.

Contributions to the work presented in this chapter are as follows: Dr. Thomas Anderson, Dr. Alexander Cioffi, and Nashrah Maryum prepared [U-^{13}C]AmB and [^{13}C]Erg. Dr. Thomas Anderson, Dr. Alexander Cioffi, Dr. Mary Clay, Dr. Grant Hisao, Dr. Andrew Nieuwkoop, Dr. Gemma Comellas, and Dr. Brice Uno prepared samples for SSNMR. Dr. Mary Clay, Dr. Grant Hisao, Dr. Andrew Nieuwkoop, Dr. Gemma Comellas, Dr. Marcus Tuttle, and Dr. Chad Rienstra acquired SSNMR data. Dr. Alexander Cioffi and Dr. Tamir Gonen performed liposome microscopy. Dr. Alexander Cioffi performed yeast rescue assays. Jennifer Hou performed cell viability and chemical sensitivity experiments. Dr. Alexander Cioffi and I performed AmB:ergosterol complex assays and Erin Wildeman tested permeabilization by AmB:ergosterol complex in yeast. Portions of this chapter were adapted from Anderson, T. M.; Clay, M. C.; Cioffi, A. G.; Diaz, K. A.; Hisao, G. S.; Tuttle, M. D.; Nieuwkoop, A. J.; Comellas, G.; Wang, S.; Uno, B. E.; Wildeman, E. L.; Maryum, N.; Gonen, T.; Rienstra, C. M.; Burke, M. D. "Amphotericin Forms an Extramembranous and Fungicidal Sterol Sponge" *Nature Chemical Biology* 2014, *10*, 400-406 and Cioffi, A. G.; Hou, J.; Grillo, A. S.; Diaz, K. A.; Burke, M. D. "Restored physiology in protein-deficient yeast by a small molecule channel" *Journal of the American Chemical Society* 2015, *137*, 10096–10099.

2.1 AMPHOTERICIN B AS AN ANTIFUNGAL

With expanding populations of immunocompromised patients, the incidence of life-threatening systemic fungal infections continues to rise (*1*). Substantially exacerbating this problem is the concomitant increase in pathogen resistance to almost all clinically approved antifungal agents. In contrast, AmB (Fig. 2.1A) has served as the gold standard treatment for systemic fungal infections for nearly six decades with minimal development of clinically significant microbial resistance (*2*). This exceptional track record reveals that resistance-refractory modes of antimicrobial action exist, and the mechanism by which AmB kills yeast is one of them. However, because of the often dose-limiting toxicity of this natural product, mortality rates for systemic fungal infections persist near 50% (*3*). As such, there are several research objectives that stand to benefit from a clarified molecular description of the biological activities and biophysical interactions of AmB within living systems: improving the notoriously poor therapeutic index of this drug, developing other resistance-refractory antimicrobial agents, and of utmost interest herein, enabling more effective utilization of its remarkable capacity to perform ion channel-like functions.

For decades, the prevailing theory has been that AmB primarily exists in the form of small ion channel aggregates that are inserted into lipid bilayers and thereby permeabilize and kill yeast cells (Fig. 2.1B) (*4-23*). An extensive series of structural and biophysical studies, including those employing planar lipid bilayers (*4-10*), liposome permeability (*9-13, 17*), Corey-Pauling-Kulton (CPK) modeling (*7-9*), UV/Vis spectroscopy (*9-11, 13, 21*), circular dichroism (*10, 11, 13, 21*), fluorescence spectroscopy (*9, 11*), Raman spectroscopy (*10*), differential scanning calorimetry (*9, 10, 21*), chemical modifications (*11-14, 17*), atomic force microscopy (*21*), transmission electron microscopy (*20*), computer modeling (*11, 15*), electron paramagnetic

resonance (*10*), surface plasmon resonance (*22*), solution NMR spectroscopy (*11*), and solid-state NMR (SSNMR) (*16-19*) spectroscopy have been interpreted through the lens of this ion channel model. Importantly, this model suggests that the path to an improved therapeutic index requires selective formation of ion channels in yeast versus human cells (*10-20*), that the search for other resistance-refractory antimicrobials should focus on membrane-permeabilizing compounds (*24*), and that the ion channel-forming and cytotoxic activities of AmB cannot be separated.

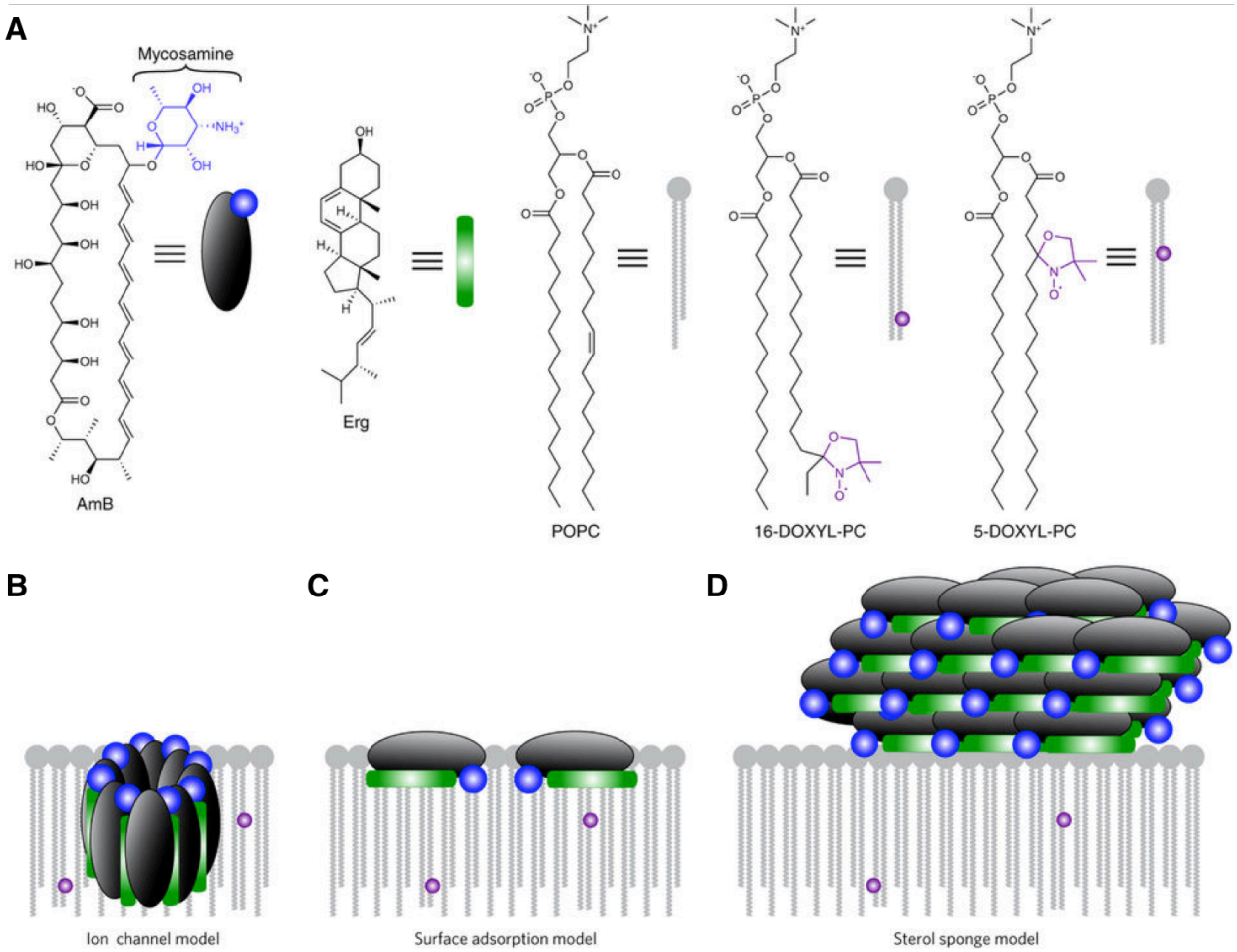

Figure 2.1 (**A**) Structures of AmB, Erg, POPC and paramagnetic probes 5-DOXYL-PC and 16-DOXYL-PC. 5-DOXYL and 16-DOXYL position a paramagnetic functional group at depths of ~12 Å and ~25 Å within the lipid bilayer, respectively. **(B)** The classic ion channel model for the structure and function of AmB. **(C)** Surface adsorption model. **(D)** A new sterol sponge model, in which AmB primarily exists in the form of large extramembranous aggregates that extract Erg from lipid bilayers.

2.2 AMPHOTERICIN B FORMS AN EXTRAMEMBRANOUS AND FUNGICIDAL STEROL SPONGE

Recent studies from our group have demonstrated that the channel-forming capacity of AmB is not required for fungicidal activity, whereas binding ergosterol (Erg) (Fig. 2.1A) is essential (*25-27*). However, the structural and biophysical underpinnings of this rare type of small molecule-small molecule interaction and its connection to cell killing all remained unclear. Sterols such as Erg in yeast play many essential roles in eukaryotic cell physiology, including functional regulation of membrane proteins, microdomain formation, endocytosis, vacuole fusion, cell division, and cell signaling (*28-31*). We thus hypothesized that sequestering Erg and thereby precluding its participation in multiple cellular functions may underlie the fungicidal action of AmB.

Guided by this hypothesis, we considered three possible models for the primary structure and function of AmB in the presence of Erg-containing phospholipid membranes (Fig. 2.1B-D): (i) In the classic channel model, AmB primarily exists in the form of small (~1 nm) ion channel aggregates inserted into the membrane, perpendicular to the membrane surface, with Erg molecules interdigitated between AmB molecules (Fig. 2.1B) (*7-9, 11, 12, 15-19, 22, 23*). (ii) In an alternative surface adsorption model, AmB is primarily positioned in the intermediate/headgroup region, oriented parallel to the plane of the membrane, sequestering Erg to the membrane surface (Fig. 2.1C) (*9, 22*). (iii) In a new sterol sponge model, AmB primarily exists in large extramembranous aggregates that extract Erg from lipid bilayers (Fig. 2.1D). In the latter two models, we envisioned that membrane-permeabilizing ion channels represent relatively minor contributors to both the structure and cytocidal activity of AmB. Here we report

an extensive series of SSNMR, transmission electron microscopy (TEM), and cell-based experiments that all support the new sterol sponge model (Fig. 1D).

Distinguishing amongst the aforementioned structural and functional models (Fig. 2.1B-D) required determining the location of AmB relative to lipid bilayers and the corresponding location of Erg in the absence and presence of AmB. Making these determinations turned out to be exceptionally challenging due to the lack of high-resolution methods for probing small molecule/membrane interactions (*9-13, 15, 17-21*). We developed an experiment based on the NMR paramagnetic relaxation enhancement (PRE) of ^{13}C nuclei caused by lipid-appended spin labels (*32-34*). The ^{13}C nuclei that lay proximal to a stable radical, such as 4,4-dimethyloxazolidine-N-oxyl (DOXYL), experience large enhancements of their longitudinal relaxation rates ($R_1 = 1/T_1$). Due to the high gyromagnetic ratio of the electron spin, the PRE is detectable for distances up to ~20 Å. Harnessing this phenomenon, we designed a magic-angle spinning (MAS) SSNMR PRE experiment based on 16-DOXYL-PC and 5-DOXYL-PC to interrogate proximity to the hydrophobic core and intermediate/headgroup region, respectively (Fig. 2.1A). Importantly, the three models under consideration (Fig. 2.1B-D) each predict distinct PRE effects for AmB. The ion channel model predicts large PREs with both spin labels, the surface adsorption model predicts large PREs only with the 5-DOXYL-PC, and the sterol sponge model predicts little or no PRE effects with either spin label.

To execute this experiment with maximized signal-to-noise ratio, we prepared highly enriched uniformly ^{13}C-labeled AmB ([U-^{13}C]AmB) via development of an improved biosynthetic protocol (*18*). By using uniformly ^{13}C-labeled glucose ([U-^{13}C]glucose) as the primary carbon source, we developed a robust procedure for attaining >80% ^{13}C incorporation, the highest ^{13}C enrichment yet reported for this natural product. This highly enriched [U-

^{13}C]AmB enabled confident assignment of ^{13}C resonances and high sensitivity PRE measurements even at high lipid to AmB ratios.

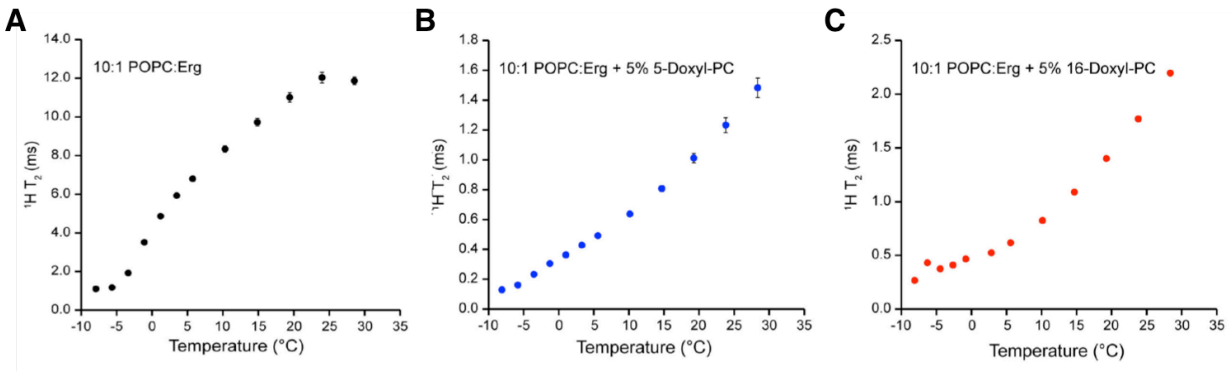

Figure 2.2 ^{1}H T_2 values of the bulk fatty acyl CH_2 peaks of molar ratios of **(A)** 10:1 POPC:Ergosterol **(B)** 10:1 POPC:Ergosterol + 5% 5-DOXYL-PC and **(C)** 10:1 POPC:Ergosterol + 5% 16- DOXYL-PC liposomes as a function of temperature. The data were acquired on a 600 MHz spectrometer over a calibrated temperature range of -8 to 28 °C.

We next identified a physiologically relevant lipid bilayer system in which we could execute the targeted experiments. Our recent structure-function studies with AmB reveal that, in contrast to liposomes comprised of fully saturated lipids, liposomes derived from monounsaturated 1-palmitoyl-2-oleoyl-sn-glycero-3-phosphocholine (POPC) and Erg yield results that mirror those obtained with live yeast cells (*26, 27*). Additionally, unlike membranes derived from fully saturated lipids, the plasma membranes of yeast and bilayers derived from POPC:Erg are both in the liquid crystalline state at 23 °C (*35, 36*). In yeast, POPC is highly abundant, and Erg is the most common sterol (*37*). Moreover, at the minimum inhibitory concentration for AmB against both *Saccharomyces cerevisiae* and *Candida albicans*, there is at least as much AmB as there is Erg (*27*). Based on this finding, we prepared lipid bilayer samples throughout this study with molar ratios of at least 10:1 POPC:Erg; for the samples containing AmB, we used at least 1 equivalent of AmB relative to Erg. These bilayers showed proper phase behavior and retained this behavior upon addition of DOXYL spin labels (Fig 2.2).

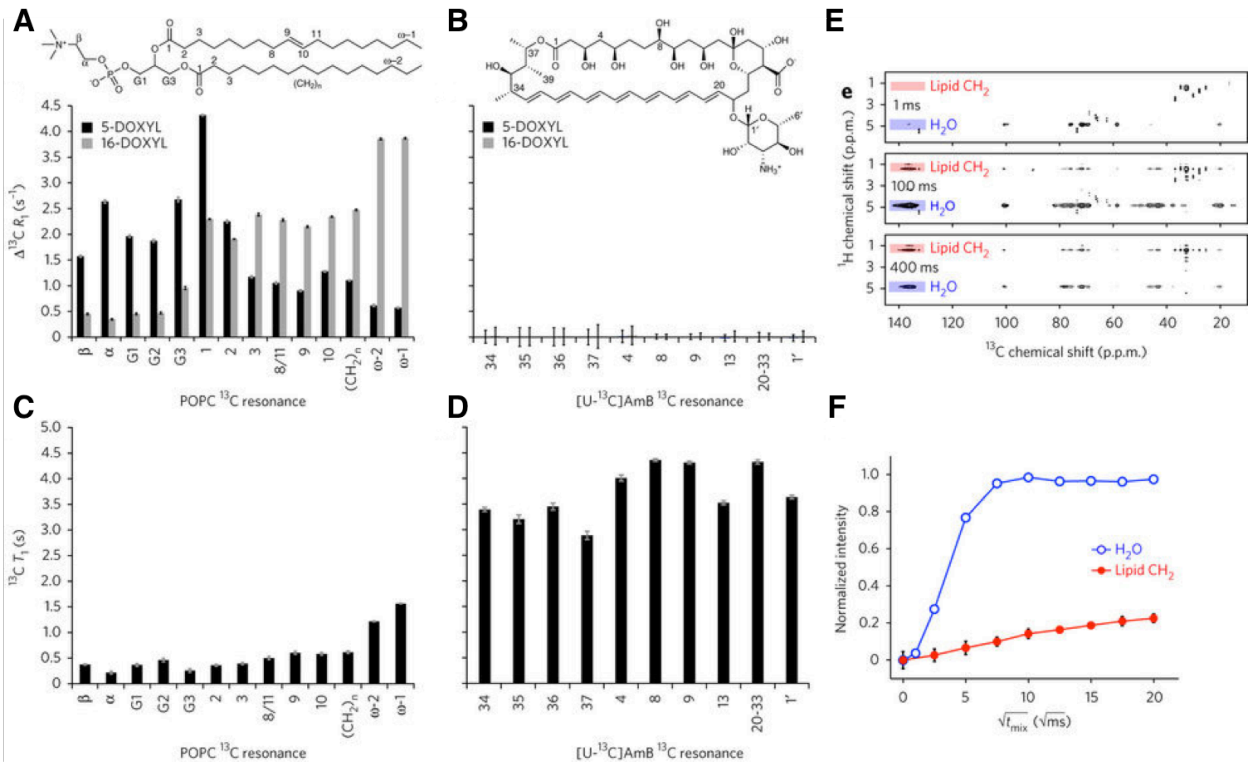

Figure 2.3 **(A)** PRE values have magnitude proportional to $1/r^6$, where r is the distance from spin label to NMR-detected nucleus. POPC controls demonstrated this proportionality in the presence of 5 mol% 5-DOXYL-PC (black) or 16-DOXYL-PC (gray). **(B)** [U-^{13}C]AmB demonstrated no PRE effects >0.03 s^{-1} in the presence of either 5-DOXYL-PC (black) or 16-DOXYL-PC (gray) paramagnetic probes. **(C,D)** Substantial differences were observed between longitudinal (T_1) ^{13}C relaxation times for sites in POPC **(C)** and AmB **(D)**. **(E)** Selected ^{1}H-^{13}C two-dimensional spectra were collected with a 1 ms T_2 filter and ^{1}H-^{1}H spin diffusion times of 1 ms, 100 ms and 400 ms; cross-peaks were from lipid acyl chains (red) and water (blue) to the [U-^{13}C]AmB polyene region. **(F)** The polarization transfer was quantified as a function of spin diffusion time from water and lipid to [U-^{13}C]AmB polyene. PRE values were derived from the difference between ^{13}C R_1 relaxation rates measured via inversion recovery for diamagnetic samples and samples containing 5-DOXYL-PC and 16-DOXYL-PC. Error bars were determined by χ^2 analysis. ^{1}H-^{13}C spin diffusion data were normalized relative to maximum intensity observed for both lipid and watercross-peaks for a given ^{13}C site after correcting for ^{1}H T_1 relaxation. Error bars were derived from the signal-to-noise ratio of the observed cross peak. Spectra were acquired at 14.1 T (600 MHz, ^{1}H frequency) at 20 °C, 10 kHz MAS.

To first confirm the position of each spin label in the bilayer, we determined the respective PREs on ^{13}C resonances in natural abundance POPC lipids with 5 mol% of each DOXYL spin label (Fig. 2.3A). Consistent with the structure of POPC membranes (*35*), bilayers doped with 5% 16-DOXYL-PC demonstrated a maximal PRE at the termini of the POPC fatty acid chains, and the PRE decreased as the distance from the center of the membrane increased (Fig. 2.3A). Similarly, the incorporation of 5-DOXYL-PC yielded maximal PREs in the intermediate and

headgroup regions of the lipid bilayer and much smaller yet still readily observable effects at the membrane interior. Together, these two spin label probes enabled confident and complementary interrogation of the innermost and outermost regions of a lipid bilayer in a straightforward SSNMR experiment.

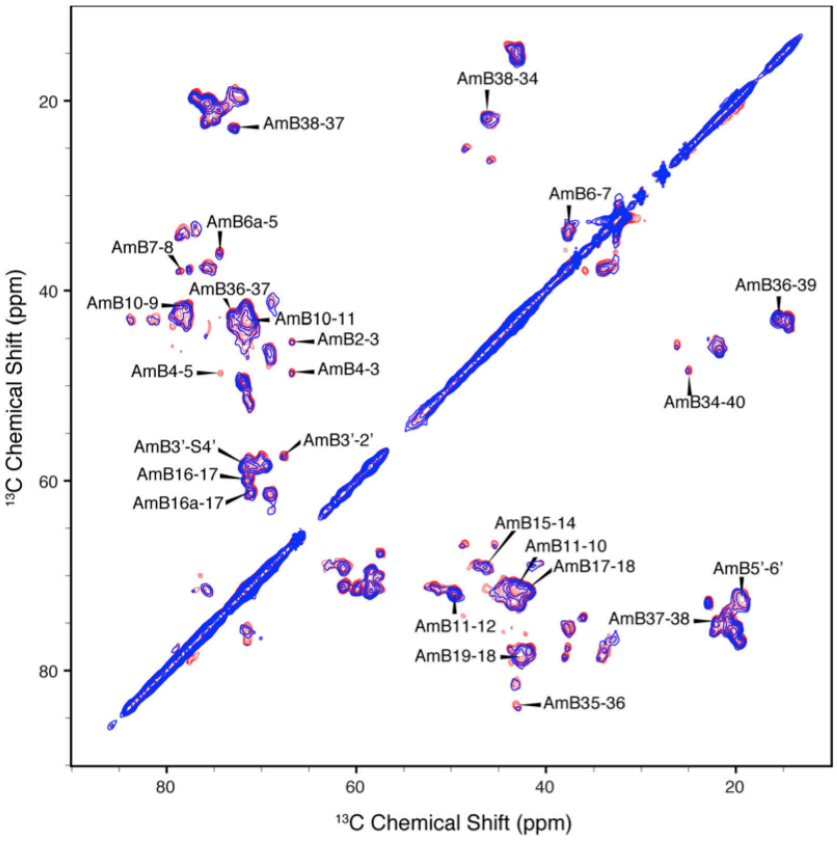

Figure 2.4 ^{13}C-^{13}C 2D spectra of (1.44 ms SPC5 mixing) of 10:1:1 POPC:[U-^{13}C]AmB:Erg (red) and 10:1:1 POPC:[U-^{13}C]AmB:Erg with 5 mol% 5-DOXYL-PC used to make site-specific assignments of the AmB and confirm that the addition of the DOXYL spin labels has no significant effect on AmB. Spectrum was acquired on a 600 MHz spectrometer, at 20 °C with and MAS rate of 10 kHz, and 75 kHz SPINAL 1H decoupling.

We next prepared samples with [U-^{13}C]AmB in POPC/Erg bilayers and used a series of ^{13}C chemical shift correlation experiments (including constant-time uniform-sign cross-peak correlation spectroscopy (CTUC-COSY) (*38*), dipolar-assisted rotational resonance (DARR) (*39*), and supercycled POST-C5 (SPC5) recoupling (*40*) to assign *de novo* the ^{13}C resonances of AmB (Fig. 2.4). We then performed PRE measurements in the presence of 16-DOXYL-PC or 5-

DOXYL-PC spin probes. The results were striking and unambiguous. As predicted by the extramembranous sterol sponge model, and inconsistent with both the membrane-inserted ion channel and surface adsorption models, we observed no significant PREs to any ^{13}C resonances of AmB with either probe (Fig. 2.3B). Therefore, we concluded that the majority of AmB in these samples was >20 Å away from both membrane-embedded spin labels.

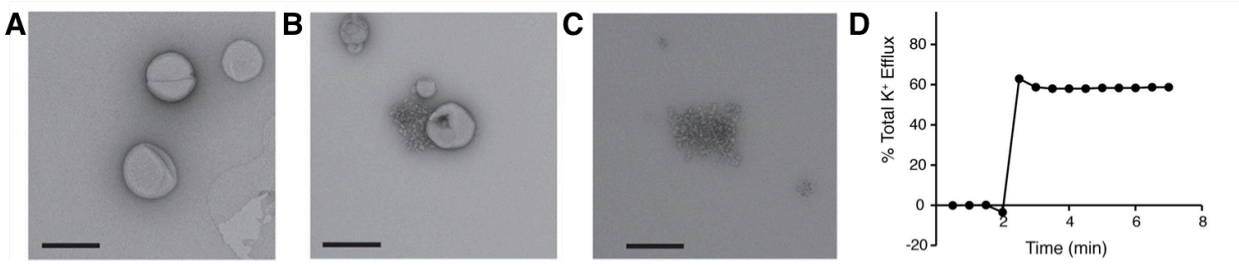

Figure 2.5 **(A)** POPC/Erg 10:1 liposomes. **(B)** POPC/Erg 10:1 liposomes with 1 equiv. (relative to Erg) of added AmB. **(C)** AmB only. Scale bars, 200 nm. **(D)** AmB promotes robust K^+ efflux from 200 mm LUV's composed of 10:1 POPC:Erg. This activity mirrors both the in vitro and in vivo efflux activity of AmB previously reported by our laboratories. 10 mol% AmB was added as a DMSO solution (final AmB concentration of 1 μM) at t = 1.5 min, and efflux is reported as a percentage of total efflux observed upon addition of Triton X-100. The observed plateau at 60% efflux is likely reflective of equilibrium between the bulk solution and the vesicle interior.

A series of additional SSNMR experiments further revealed that AmB exists in the form of large aggregates that are more closely associated with water than lipids. The longitudinal relaxation times (T_1 values) for AmB were substantially longer than those of the lipids, consistent with large and relatively immobile aggregates of AmB (Fig. 2.3C,D). SSNMR spin-diffusion experiments, designed for the purpose of probing membrane protein topology (*41*), revealed that lipid-AmB correlations reached maximum intensity only at very long mixing times (~400 ms) for all resolvable carbons on AmB (Fig. 2.3E,F), indicating that the majority of the lipids were >15 Å away from the AmB. In contrast, we observed strong correlations between water and AmB within just 25 ms, consistent with intimate proximity of the AmB aggregates to water.

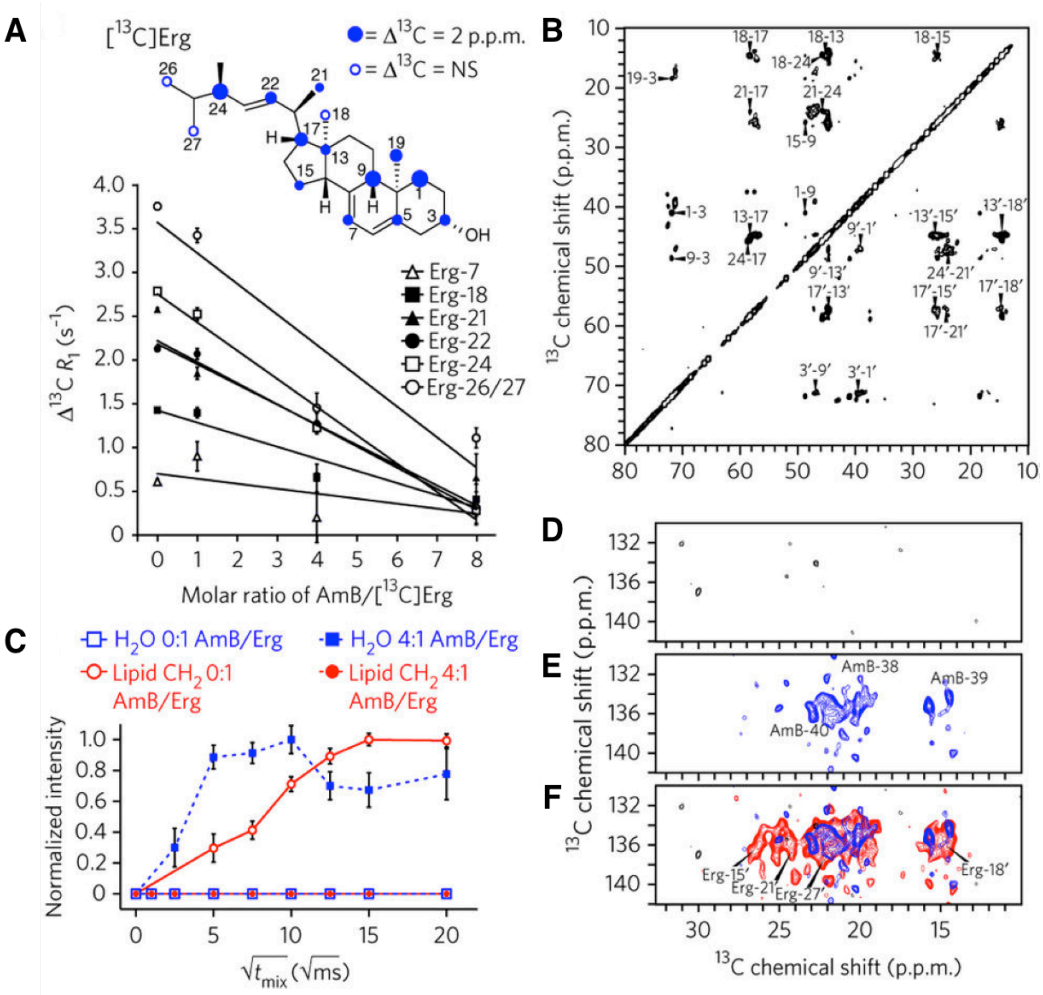

Figure 2.6 (A) Samples prepared using 40:1 POPC/ [^{13}C]Erg ± 5 mol% 16-DOXYL-PC showed a progressive decrease in PRE effects of resolved Erg resonances as the ratio of AmB/[^{13}C]Erg increased. **(B)** The two-dimensional ^{13}C-^{13}C DARR spectrum of [^{13}C]Erg (250-ms mixing, 10:1:1 POPC/AmB/[^{13}C]Erg) changed in the presence of AmB, exhibiting new cross-peaks. **(C)** The ^{1}H-^{13}C polarization transfers from water (blue) and lipid (red) to Erg-7 were substantially different in the absence (closed circles and squares, dashed line) and presence (open circles and squares, solid line) of AmB. **(D-F)** Expansions of the olefin-to-methyl spectral region for two-dimensional [^{1}H]-^{13}C-[^{1}H-^{1}H]-^{13}C spectra[42, 43] of only [^{13}C]Erg (328 h signal averaging time) **(D)**, only [U-^{13}C]AmB (187 h) **(E)** and both [^{13}C]Erg and [U-^{13}C]AmB (187 h) **(F)**. Error bars in **A** were derived from χ^2 analysis of inversion recovery trajectories. The ^{1}H-^{13}C spin diffusion data in **C** were normalized relative to the maximum intensity observed for both lipid and water cross-peaks for a given ^{13}C site after correcting for ^{1}H T_1 relaxation, and error bars were derived from the signal-to-noise of the observed cross-peak. Spectra were acquired at 14.1 T (600 MHz ^{1}H frequency). Data in **A-C** were acquired at 10 kHz MAS, at 20 °C and 10 °C, respectively. The [^{1}H]-^{13}C-[^{1}H-^{1}H]-^{13}C spectra **(D–F)** were acquired at 10 °C, 11.628 kHz MAS; processed with 40-Hz and 75-Hz line broadening in the direct and indirect dimensions, respectively; and were drawn with contour threshold set to four times the r.m.s. noise.

To further probe these aggregates and distinguish between an intramembranous vs. extramembranous location, we also performed transmission electron microscopy analysis of

large unilamellar vesicles (LUVs) comprised of the same ratio of POPC:Erg ± AmB. In the absence of added AmB, we observed well-formed LUVs (Fig. 2.5A). When AmB was added, we observed large extramembranous aggregates (Fig. 2.5B). These aggregates were associated with one or more LUVs, suggesting an interaction between the surfaces of the aggregate and the lipid bilayer. When we added the same amount of AmB to the same volume of LUV-free buffer, similar aggregates of AmB were observed (Fig. 2.5C). These observations are consistent with the spontaneous formation in aqueous buffer of large AmB aggregates that externally associate with the surface of lipid bilayers.

Importantly, parallel potassium efflux experiments revealed readily observable membrane permeabilization upon adding the same concentration of AmB to suspensions of the same POPC:Erg LUVs (Fig. 2.5D). This observation was consistent with a minor fraction of AmB existing in the form of membrane-permeabilizing ion channels that are too small to be visualized by TEM. This analysis was also consistent with all of our SSNMR data, in which the limits of detection permit up to 5% of the AmB existing in the membrane.

With the structural aspects of the sterol sponge model confirmed, we aimed to test the functional prediction that these large extramembranous aggregates of AmB extract Erg from lipid bilayers. We first performed a modified SSNMR PRE experiment in which we analyzed ^{13}C skip-labeled Erg ([^{13}C]Erg, Fig. 2.6A) (*19*) in spin label-containing bilayers as a function of AmB:[^{13}C]Erg ratio (Fig. 2.6A). This labeling pattern provided sufficient sensitivity that the ratio of POPC to Erg was increased to 40:1, readily enabling titrations of the AmB:Erg molar ratio while retaining the biophysical properties of the lipid bilayer. We then prepared bilayers comprised of POPC:[^{13}C]Erg 40:1 ± 5 mol% 16-DOXYL without or with increasing amounts of natural abundance AmB. AmB had minimal effect on the POPC PRE (Fig. 2.7). In contrast, we

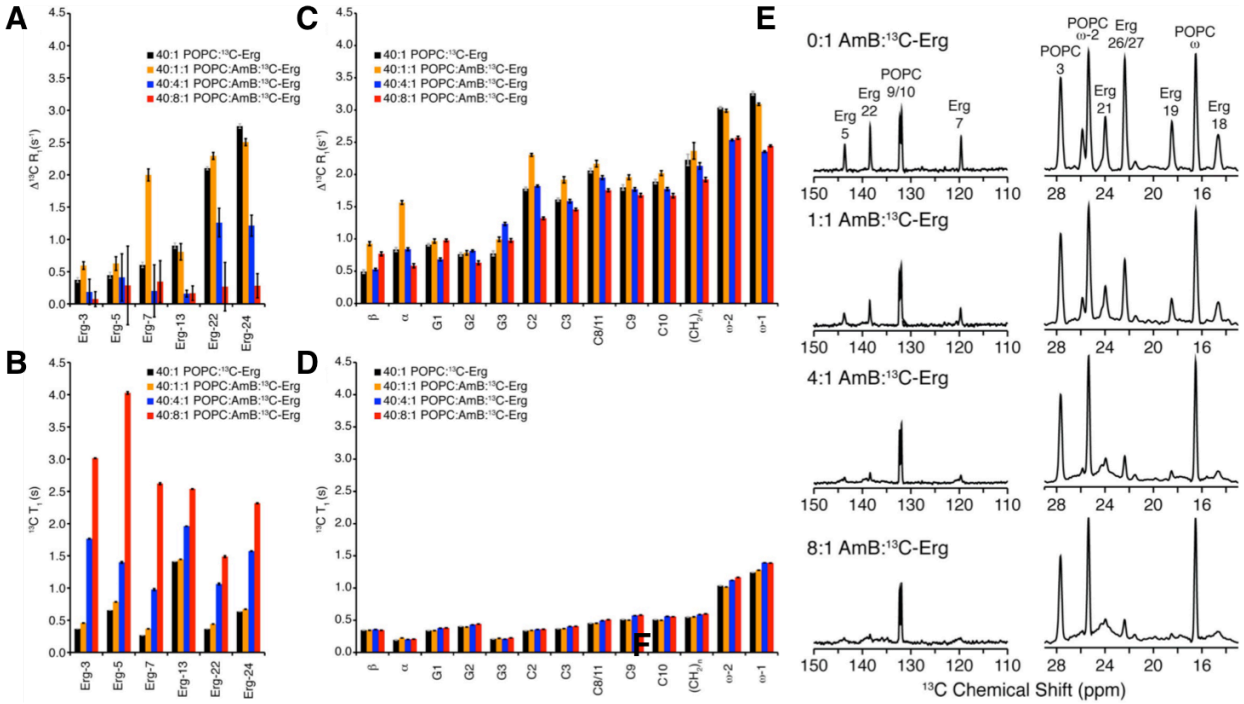

Figure 2.7 The addition of AmB to POPC:Erg liposomes has a large effect on Erg, but a relatively small effect on POPC. The combination of the decrease in (A) PRE and substantial increase in the **(B)** longitudinal relaxation times (T_1) of Erg are consistent with the formation of an AmB:Erg complex that is separated from the lipid bilayer. Note the small relative change in the POPC **(C)** PRE (~20% on average) and **(D)** ^{13}C T1 values (~ 10% on average). (40:1 POPC:[^{13}C]Erg (black), 40:1:1 POPC:AmB:[^{13}C]Erg (orange), 40:4:1 POPC:AmB:[^{13}C]Erg (blue), and 40:8:1 POPC:AmB:[^{13}C]Erg (red) liposomes ± 5 mol% 16-DOXYL-PC.) Only methine (CH) and methylene (CH_2) sites that do not shift significantly (< 0.5 ppm) upon addition of AmB are shown. SSNMR experiments were performed on a 600 MHz spectrometer, at 20 °C with an MAS rate of 10 kHz and 75 kHz ^{1}H decoupling. **(E)** AmB extracts Erg from lipid bilayers. 1D ^{13}C spectra of [^{13}C]Erg titrated with natural abundance AmB. As a function of AmB:Erg ratio, the [^{13}C]Erg resonances broaden from an average linewidth of 0.3 ppm to >1.0 ppm, consistent with formation of an AmB-Erg complex Spectra were acquired at 14.1 T (600 MHz ^{1}H frequency), at 20 °C and 10 kHz MAS rate.

observed a progressive decrease in the [^{13}C]Erg PRE as the amount of AmB increased, indicating that Erg increasingly occupied a position outside the lipid bilayer (Fig. 2.6A, Fig. 2.7A). In the absence of AmB (AmB:[^{13}C]Erg 0:1), we observed substantial PREs for the resolved ^{13}C signals of [^{13}C]Erg; for several sites, such as Erg-18, Erg-21, Erg-22, Erg-24, Erg-26 and Erg-27, the PRE was ~1.5 s−1 or greater, and the ^{13}C T_1 values were relatively short (<1.5 s) (Fig. 2.7B). These findings are consistent with the structure of Erg-containing membranes in which the Erg is inserted into the hydrophobic core of the bilayer (*35*), with the isopropyl tail most deeply inserted and therefore most proximal to the 16-DOXYL label. These conformation-specific PREs

for [^{13}C]Erg decreased markedly upon the addition of AmB (Fig. 2.6A, Fig. 2.7A). Specifically, with increasing amounts of natural abundance AmB (AmB:[^{13}C]Erg ratios of 1:1, 4:1, 8:1), we observed a progressive decrease, with at least a three-fold reduction in observed PRE in the AmB:[^{13}C]Erg 8:1 sample. These results support the interpretation that Erg increasingly occupies a position outside the lipid bilayer membrane in the presence of increasing amounts of AmB.

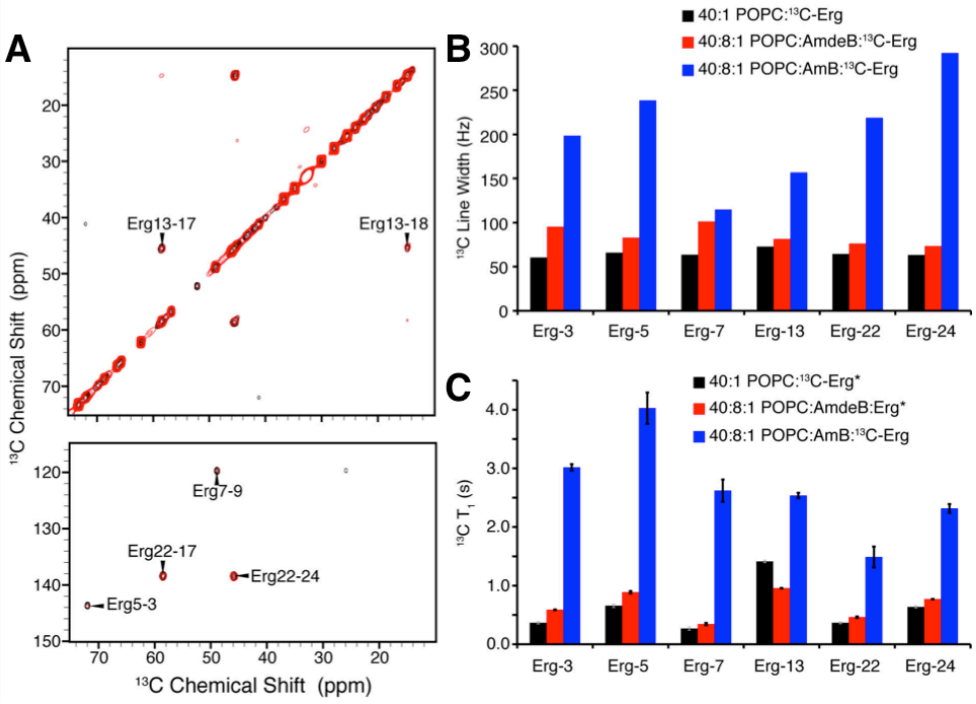

Figure 2.8 As a control experiment we also examined the effect of AmdeB, a derivative of AmB lacking the mycosamine appendage that does not bind Erg. There were no chemical shift perturbations observed upon the addition of AmdeB, as shown in **(A)** the over lay of ^{13}C-^{13}C 2D DARR (500ms mixing) spectra of 40:1 POPC:[^{13}C]Erg (black), 40:8:1 POPC:AmdeB:[^{13}C]Erg (red). This is in stark contrast to the dramatic changes observed with the addition of AmB to POPC:[^{13}C]Erg membranes. Furthermore there were only slight perturbations of the **(B)** ^{13}C linewidth, and **(C)** ^{13}C longitudinal (T_1) relaxation times in comparison to those changes induced by the addition of an equivalent amount of AmB (40:8:1 POPC:AmB:[^{13}C]Erg (blue)). Spectra were acquired on a 14.1 T (600 MHz ^{1}H frequency) spectrometer, at 20 °C with an MAS rate of 10 kHz and 75 kHz ^{1}H decoupling.

Additional SSNMR experiments also supported this conclusion and further demonstrated that the extracted Erg is physically bound to the extramembranous aggregates of AmB. As the ratio of AmB:[^{13}C]Erg increased, Erg resonances, but not those of POPC, demonstrated inhomogeneous broadening (*19*), consistent with a transition from a mobile state to an immobile

state (Fig. 2.7E). The average ^{13}C T_1 relaxation values for [^{13}C]Erg also followed the expected trend, increasing with the AmB:[^{13}C]Erg ratio (Fig. 2.7B). Two-dimensional ^{13}C-^{13}C correlation spectra further revealed several ^{13}C-Erg resonances that shifted significantly upon the addition of AmB (Fig. 2.6B), and resolved bound state resonances exhibited significantly higher linewidth and T_1 values than those of the corresponding unbound state. In the absence of AmB, we observed very strong lipid-Erg correlations and no water-Erg correlations (Fig. 2.6C) (*41*), whereas in the presence of AmB we observed strong water correlations to all resolved Erg sites, with polarization transfer rates similar to those observed for AmB (Fig. 2.6C). We also repeated one- and two-dimensional chemical shift, linewidth, and T_1 analyses of [^{13}C]Erg in the presence of amphoteronolide B (AmdeB), a synthesized derivative of AmB that lacks the mycosamine appendage and does not bind Erg (*26, 27*), and observed no ^{13}C-Erg chemical shift perturbations and only very small changes in linewidths and T_1 values (Fig. 2.8).

To definitively probe whether the extracted Erg is bound to the AmB aggregate, we prepared an additional series of samples in which ^{13}C labels were placed on (i) only Erg (Fig. 4D), (ii) only AmB (Fig. 4E), and (iii) both AmB and Erg (Fig. 4F). [^{1}H]-^{13}C-[^{1}H-^{1}H]-^{13}C spectra (*42, 43*) for the first two samples showed only the anticipated intramolecular correlations (Fig. 4D, 4E), while the sample containing labels on both AmB and Erg revealed many new intermolecular AmB-Erg cross peaks (Fig. 4F), consistent with Erg aligned parallel to the polyene region of AmB and directly confirming the formation of a small molecule-small molecule complex. We also measured the ^{1}H-^{13}C dipolar couplings for resolved sites in both AmB and Erg using the T-MREV recoupling sequence (*44*) (Fig 2.9A-F) and Erg (Fig 2.9G-L) to determine the relative mobility of these sites. In the absence of AmB, Erg was mobile as evidenced by the low order parameters, but in the presence of AmB, the order parameters shifted to the same rigid lattice

limit observed for AmB. Furthermore, we observed line widths of >110 Hz for both AmB and Erg in the sterol sponge. Therefore, we concluded that AmB extracts Erg from lipid bilayers into large, extramembranous aggregates.

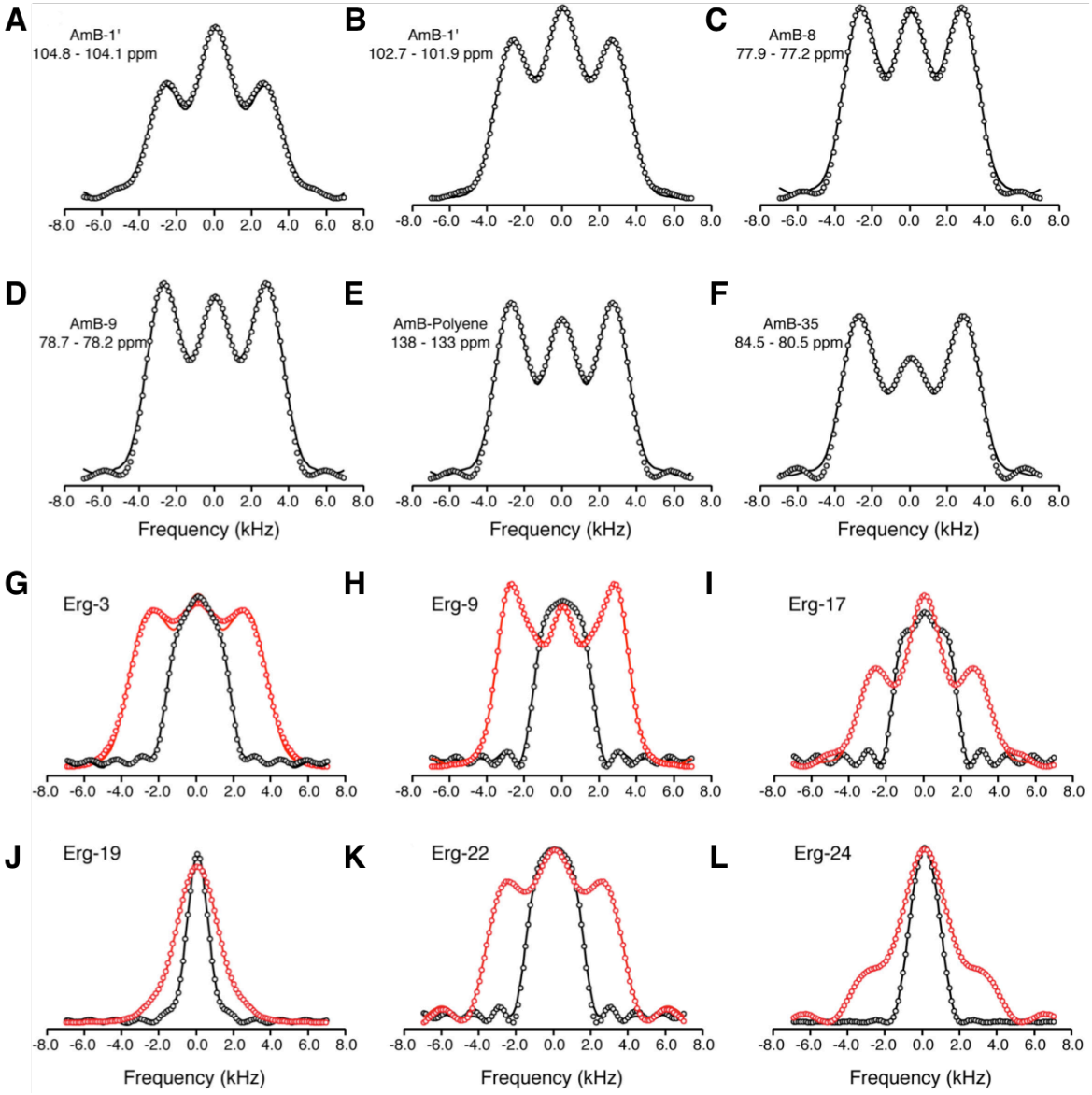

Figure 2.9 (A-F) The T-MREV dipolar lines shapes and order parameter measured select AmB resonances in 10:1:1 POPC:U-13C-AmB:Erg MLVs (black, experimental solid line, simulation open circle) confirm that sterol sponge is rigid. Spectra was acquired on a 600 MHz spectrometer, at 20 °C with and MAS rate of 8.333 kHz, and 85 kHz TPPM 1H decoupling59, using N=4 T-MREV. **(G-L)** The substantial broadening of the T-MREV dipolar lines shapes and order parameter measured for select Erg resonances in 40:0:1 (black, experimental solid line, simulation open circle) and 40:4:1 POPC:AmB:13C-Erg (red, experimental solid line, simulation open circle) further confirms the absorption of Erg by the AmB sterol sponge. Spectra was acquired on a 600 MHz spectrometer, at 20 °C with and MAS rate of 8.333 kHz, and 85 kHz TPPM 1H decoupling, N=4 T- MREV.

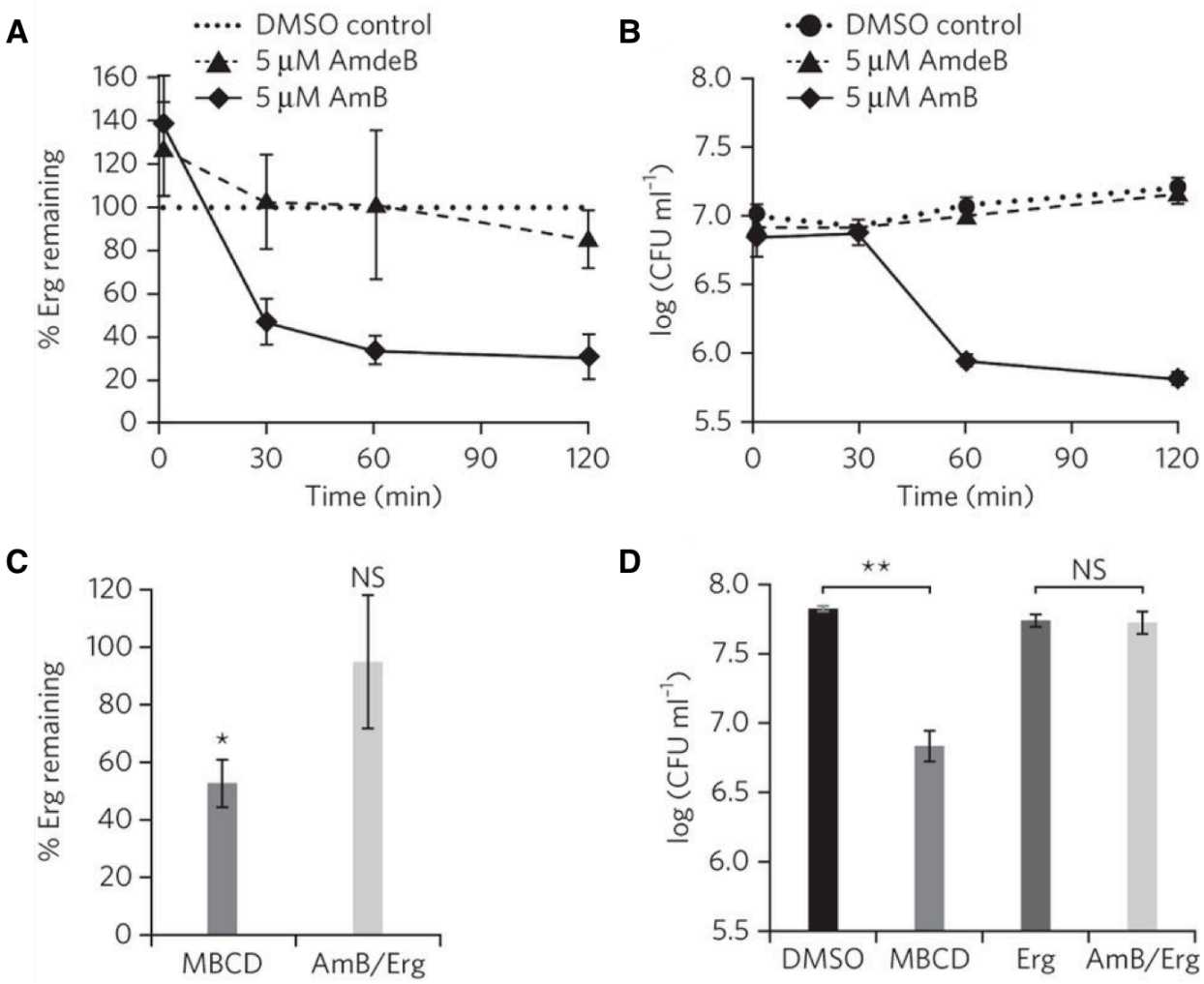

Figure 2.10 **(A)** AmB extracted Erg from the membranes of *S. cerevisiae* cells in a time-dependent manner, whereas the non-Erg-binding derivative AmdeB showed no Erg-extracting activity. The percentage of Erg remaining in the cell membranes was normalized to that measured in DMSO-only treated controls. **(B)** Cell killing paralleled Erg extraction in AmB-treated cells. The non-Erg-extracting derivative AmdeB showed no cell-killing effects. **(C)** Erg extraction after 120 min of incubation. 500 mM MBCD extracted Erg from the membranes of *S. cerevisiae* cells, whereas a pre-formed 5 μM AmB:25 μM Erg complex did not. The percentage of Erg remaining in the cell membranes was normalized to that in DMSO-only and 25 μM Erg in DMSO-only treated controls, respectively. **(D)** Cell killing after 120 min incubation was observed for yeast treated with 500 mM MBCD but not for yeast treated with 5 μM AmB:25 μM Erg complex. Data represent mean ± SEM for at least three independent experiments. *$P < 0.02$; **$P < 0.002$; NS, not significant.

Finally, we tested the validity of the sterol sponge model in cells. First, we probed whether AmB extracts Erg from the cell membrane of yeast by adapting an ultracentrifugation-based membrane isolation assay (*45*) to quantify the amount of Erg in the membranes of live *Saccharomyces cerevisiae* cells in the absence and presence of AmB. As shown in Fig. 2.10A, AmB very effectively extracted Erg in a time-dependent fashion. In contrast, we observed no Erg

extracting effects with the non-Erg-binding derivative AmdeB. It is interesting to note that AmB treatment also extracts lipids as measured by the progressive loss of palmitoyl (Fig. 2.11A) and oleoyl tails (Fig. 2.11B) over 2 hours of treatment.

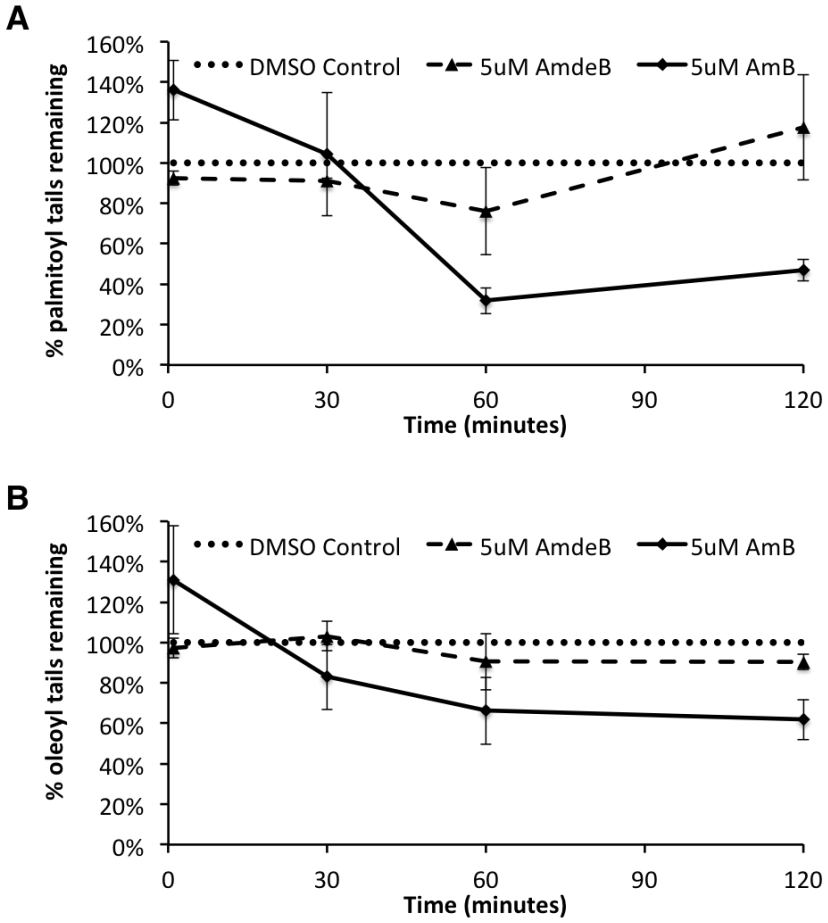

Figure 2.11 AmB extracted lipids **(A)** palmitoyl tails and **(B)** oleoyl tails from the membranes of *S. cerevisiae* cells in a time-dependent manner, whereas the non-Erg-binding derivative AmdeB showed no lipid-extracting activity. The percentage of lipids remaining in the cell membranes was normalized to that measured in DMSO-only treated controls. Data represent mean ± SEM for four independent experiments.

Further experiments demonstrated that the Erg-extracting activity of AmB was responsible for its cell killing effects. As shown in Fig. 2.10B, we observed no cell killing with DMSO or AmdeB, whereas AmB promoted robust cell killing with a time course that paralleled Erg extraction. In addition, methyl-β-cyclodextrin (MBCD), a cyclic oligosaccharide known to extract sterols from membranes (*46*), similarly demonstrated both Erg extracting and cell killing activities (Fig. 2.10C and 2.10D). Finally, the sterol sponge model predicts that AmB aggregates pre-saturated with Erg will lose the ability to extract Erg from membranes and kill yeast. We found conditions that promoted the formation of stable and soluble aggregates of AmB and Erg,

thereby enabling this hypothesis to be tested. As predicted, treating cells with this pre-formed AmB:Erg complex resulted in no Erg extraction (Fig. 2.10C), and no cell killing (Fig. 2.10D).

When we characterized this stable aggregate using UV/Vis, we saw distinct shift in UV spectra between the different forms of AmB and AmB bound to Erg in a complex (Fig. 2.12A). We also confirmed that the AmB aggregates we observed in our SSNMR, TEM, and cell- based experiments are similar (Fig. 2.12B-D). We also performed a series of assays where we heated the aggregates of AmB with different sterols, Erg and the endogenous human sterol cholesterol (Chol) and established melting curves. We found that both AmB:sterol aggregates dissociated at higher temperatures than the AmB only aggregate, which indicates increased thermal stability of the AmB:sterol complex (Fig. 2.12E). Notably, AmB:Erg requires a higher temperature than AmB:Chol to dissociate, which may preliminarily indicate a greater binding affinity for Erg than Chol (Fig. 2.12E). However, the nature of the interaction between AmB and sterol within the aggregate will require further study to fully elaborate.

The sterol sponge model provides a new foundation for better understanding and more effectively harnessing the unique biophysical, biological, and medicinal properties of this small molecule natural product. Based on the classic ion channel model, many efforts over the past several decades to improve the therapeutic index of AmB focused on selectively permeabilizing yeast versus human cells (*11, 13*). This approach has not yielded a clinically viable derivative of the natural product. The sterol sponge model suggests that an alternative approach will be more effective. Specifically, analogous to the now clarified mechanism of antifungal activity, the extraction of cholesterol by large extramembranous aggregates of AmB may be primarily responsible for toxicity to human cells. This, in turn, suggests that the goal should be to maximize the relative binding affinity of AmB aggregates for Erg versus cholesterol. This insight

is already guiding development of the first derivatives of AmB that are toxic to yeast cells but not human cells and thus hold exceptional promise for yielding an improved therapeutic index (*47*).

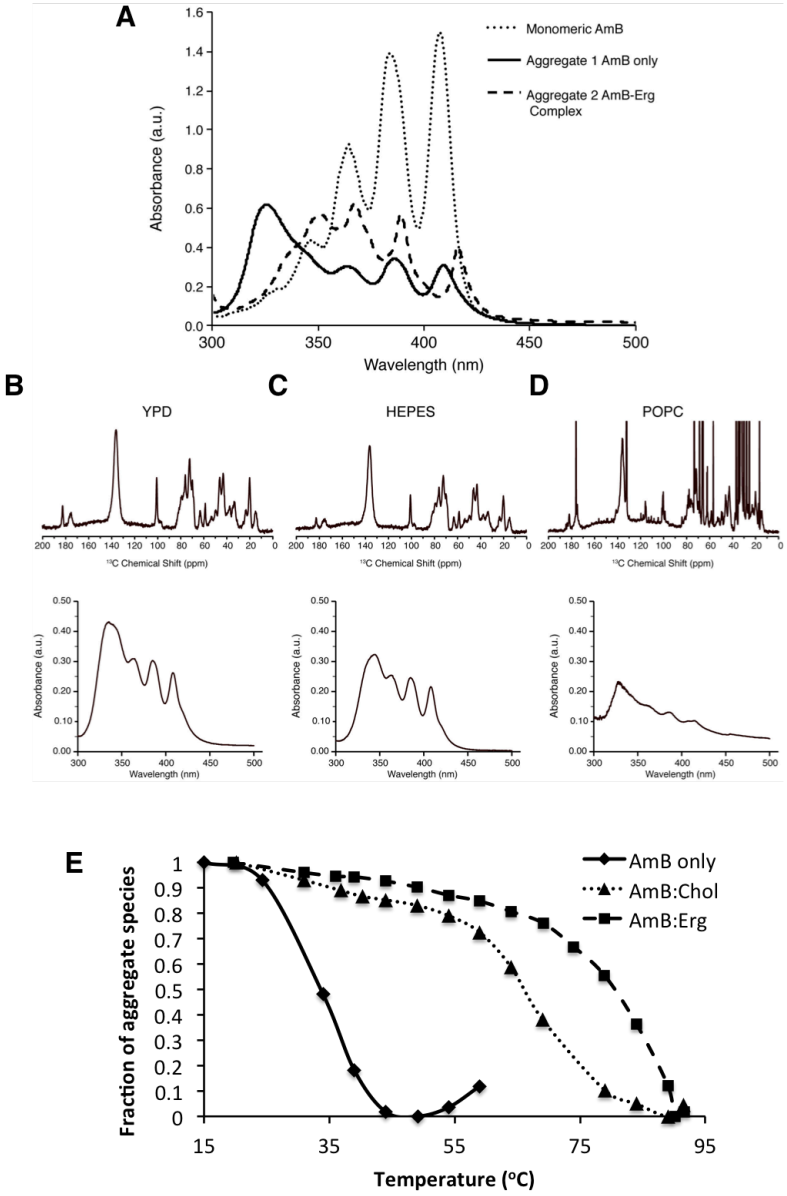

Figure 2.12 (A) Monomeric AmB in PBS:methanol and AmB aggregate in PBS buffer demonstrate spectral signatures by UV spectroscopy. ^{13}C NMR and UV-Vis spectra of **(B)** AmB precipitated in YPD buffer used for *in vivo* studies, **(C)** AmB precipitated in HEPES buffer used for TEM studies, and **(D)** 10:1 mole ratio of POPC:AmB MLVs lyophilized and rehydrated for SSNMR studies.

The sterol sponge model also offers a new rationale for the paucity of clinically relevant microbial resistance that is a hallmark of AmB as a therapeutic. Because the extraction of Erg renders yeast membranes Erg-deficient, AmB may simultaneously perturb all cellular processes that depend on membrane Erg (*28-31, 48*). This likely includes many different membrane

proteins that directly bind Erg (*28-31*), and simultaneous mutation of all such proteins in a manner that alleviates this Erg dependence is highly improbable. It has also remained unclear why, in contrast to the rarity with which AmB resistant mutants are found in patients, it is relatively easy to generate AmB-resistant yeast mutants in cell culture experiments (*49*). The sterol sponge model provides a rationale for this dichotomy. AmB-resistant mutants generated in cell culture generally possess modified sterols in their membranes, e.g., lanosterol (*50*) (and/or other biosynthetic precursors to Erg) to which AmB does not bind (described above) (*26*). It was previously assumed that such changes in sterol content minimize antifungal potency by minimizing membrane-permeabilizing activity (*9, 10, 13, 49*). The sterol sponge model alternatively suggests that, because AmB does not bind or extract lanosterol, this modified sterol remains in the membrane to serve as a surrogate binding partner for sterol-dependent proteins. Due to the structural differences between lanosterol and Erg described above, however, the former is likely only a minimally effective substitute, resulting in reduced activity of many proteins that require specific interactions with Erg to function properly. This, in turn, may translate into substantially reduced pathogenicity of the resulting yeast mutants. Consistent with this notion, strains of yeast with modified sterol content have markedly reduced pathogenicity in animal models (*49*). Such strains may routinely emerge in patients treated with AmB, but, due to their reduced pathogenicity, they cannot thrive and/or are rapidly cleared by the immune system of the host. A recently reported alternative series of studies provide complementary support for these conclusions (*49*).

But most importantly, the clarified picture of the structural and functional underpinnings of AmB activity provided by the sterol sponge model now illuminates a rational roadmap for separating the ion channel forming and cytotoxic activities of AmB. Small, membrane-spanning

ion channel aggregates likely exist as minor components in equilibrium with the large extramembranous assemblies of AmB characterized herein. This proposal is consistent with the weak AmB-lipid correlations observed in the SSNMR spin diffusion experiments, and the limits of detection of the SSNMR PRE and TEM studies. As we have previously demonstrated, binding ergosterol in the absence of channel activity is sufficient for cell killing (*27*). Specifically, the capacity for channel formation can be selectively eliminated while preserving the capacity for both Erg binding and cell killing via deleting the C35 hydroxyl group appended to AmB (*27*). In the sterol sponge model, this result can be rationalized by invoking a selectively destabilizing influence of this functional group deletion on the smaller membrane-inserted channel aggregates. Future studies will aim to determine whether this putative equilibrium between large extramembranous and small membrane-spanning aggregates can be alternatively shifted to favor ion channel formation, thereby maximizing potentially useful membrane-permeabilizing functions (*27*) while minimizing cytotoxic sterol extracting activity.

2.3 THE PROSPECT OF MOLECULAR PROSTHETICS

There are many currently incurable human diseases that are caused by missing protein ion channels, including cystic fibrosis, Bartter syndrome, Dravet syndrome, and Dent's disease (*51, 52*). Like many other human diseases caused by missing proteins, these diseases are difficult to treat, and new approaches are needed. Some small molecules can perform ion channel-like functions (*4, 53-61*), suggesting the possibility of replacing missing protein ion channels with small molecule mimics. Closely replicating the functions of ion selective and tightly regulated protein channels with small molecules is challenging. However, robust protein networks comprising pumps and channels drive specific ions in targeted directions throughout the spectrum of living systems (*62*). We then questioned if relatively unselective and unregulated

small molecule mimics of missing protein channels might be capable of collaborating with the endogenous protein ion pumps and channels to restore physiology.

Yeast represents an excellent model system for studying eukaryotic physiology (*63, 64*). Moreover, deficiencies of specific protein ion transporters in yeast are known to lead to dramatic no-growth phenotypes, therefore providing a unique opportunity for using cell growth as a marker for physiology restoration. In yeast, ATP-driven V-ATPase and Pma1 proton pumps in the vacuolar and plasma membranes, respectively, collaborate with passive Trk potassium transporters in the plasma membrane to achieve intracellular movement of potassium required for cell growth (Fig. 2.13A, left) (*65*). Loss of Trk transporters impairs uptake of environmental potassium and results in a no-growth phenotype (Fig. 2.13A, middle) (*66-68*). Because the ATP-driven pumps, the primary drivers of ion movement, are still active in this yeast, we hypothesized that a small molecule ion channel permeable to potassium could collaborate with V-ATPase and Pma1 to restore cell growth (Fig. 2.13A, right).

Following our previous work on AmB, we identified this ion channel-forming natural product (Fig. 2.13B) as a viable candidate to test this hypothesis (*4*). AmB is known to permeabilize yeast cells to potassium and other ions (*10, 69*). As discussed previously, AmB is also highly toxic to yeast, and this toxicity was considered inextricably linked to its membrane permeabilization. However, we found a synthesized derivative of AmB lacking a single oxygen atom at C35 (C35deOAmB) (Fig. 2.13B) does not form ion channels and yet still maintains potent fungicidal activity (*27*). AmB and C35deOAmB, which differ via a single atom, represent a unique pair of probes for determining the impact of small molecule-mediated ion channel activity on organismal physiology. This finding combined with the studies discussed in section 2.2 suggested that the channel activity of AmB might be separated from its cytocidal activity by

simply adding this compound at low concentrations, staying below the toxic ratio of AmB to sterol.

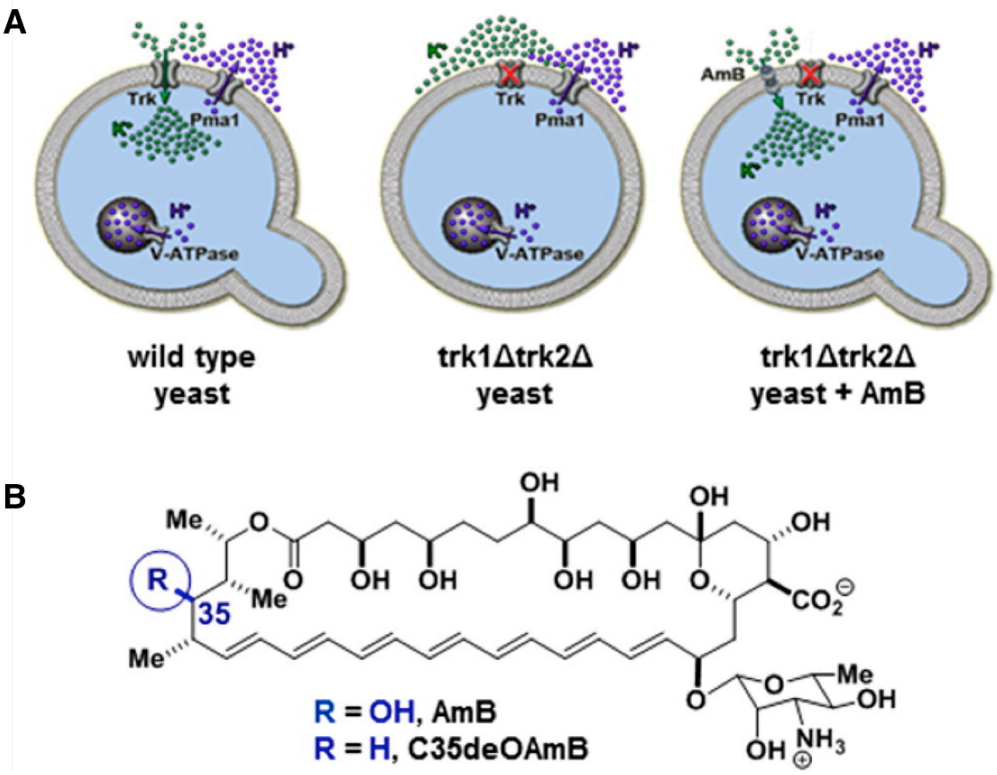

Fig 2.13 (A) Prospect of replacing missing protein ion transporters with small molecule mimics. **(B)** Chemical structures of the archetypical ion channel-forming small molecule amphotericin B and its single atom-deficient and channel-inactivated derivative C35-deoxy amphotericin B (C35deOAmB).

2.4 RESTORED PHYSIOLOGY IN PROTEIN-DEFICIENT YEAST BY THE SMALL MOLECULE AMB CHANNEL

We first tested the hypothesis that AmB could restore cell growth in potassium transporter-deficient yeast with a modified functional complementation experiment (*70*). Consistent with prior reports (*66, 67*), growth was observed when wild type *Saccharomyces cerevisiae* were streaked onto agar plates containing normal concentrations of potassium (10 mM) (Fig. 2.14A, left), and no growth was observed for the potassium transporter-deficient strain (trk1Δtrk2Δ)

under the same conditions (Fig. 2.14A, middle). Strikingly, the addition of a low concentration of AmB (125 nM) to an otherwise identical agar plate vigorously restored growth of the trk1Δtrk2Δ mutant (Fig 2.14A, right).

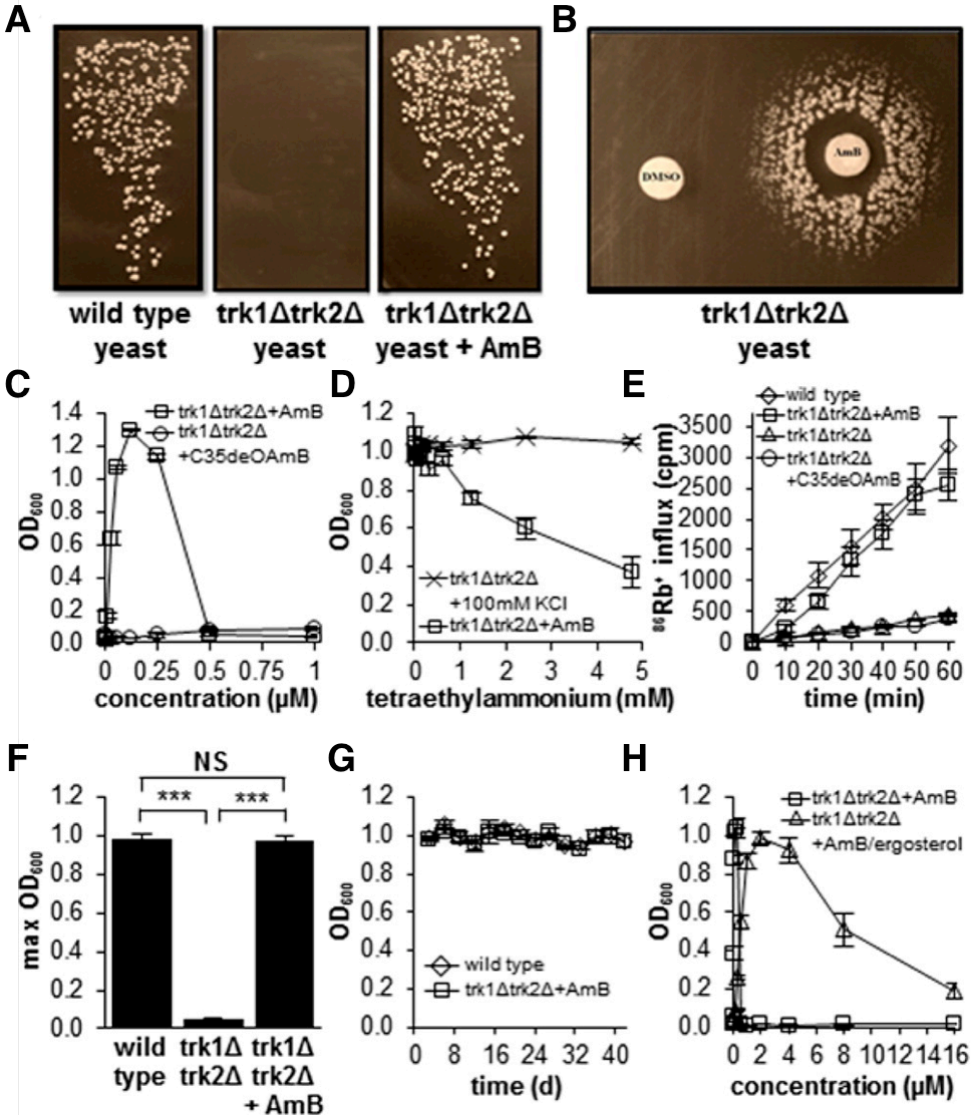

Figure 2.14. **(A)** Restoration of yeast cell growth under normal potassium conditions (10 mM) with a small molecule mimic of missing protein potassium transporters. **(B)** Disc diffusion with AmB on a plate of trk1Δtrk2Δ cells. **(C)** AmB restores cell growth at concentrations below its minimum inhibitory concentration, while C35deOAmB does not restore growth. **(D)** Tetraethylammonium diminishes AmB-mediated growth restoration in trk1Δtrk2Δ cells but has no effect on trk1Δtrk2Δ cells grown under permissive conditions (100 mM KCl). **(E)** AmB restores uptake of extracellular $^{86}Rb^{+}$, a tracer for K^{+}, in trk1Δtrk2Δ cells, but C35deOAmB does not. **(F)** Vigorous restoration of cell growth is observed upon treating trk1Δtrk2Δ cells with AmB. **(G)** Similar to wild type cells, AmB-rescued trk1Δtrk2Δ cells show sustained growth over a period of >40 days. **(H)** A preformed AmB-ergosterol complex dramatically increases the range of concentrations over which physiology is restored. NS, not significant. ***$P \leq 0.0001$. Graphs depict means ± SEM.

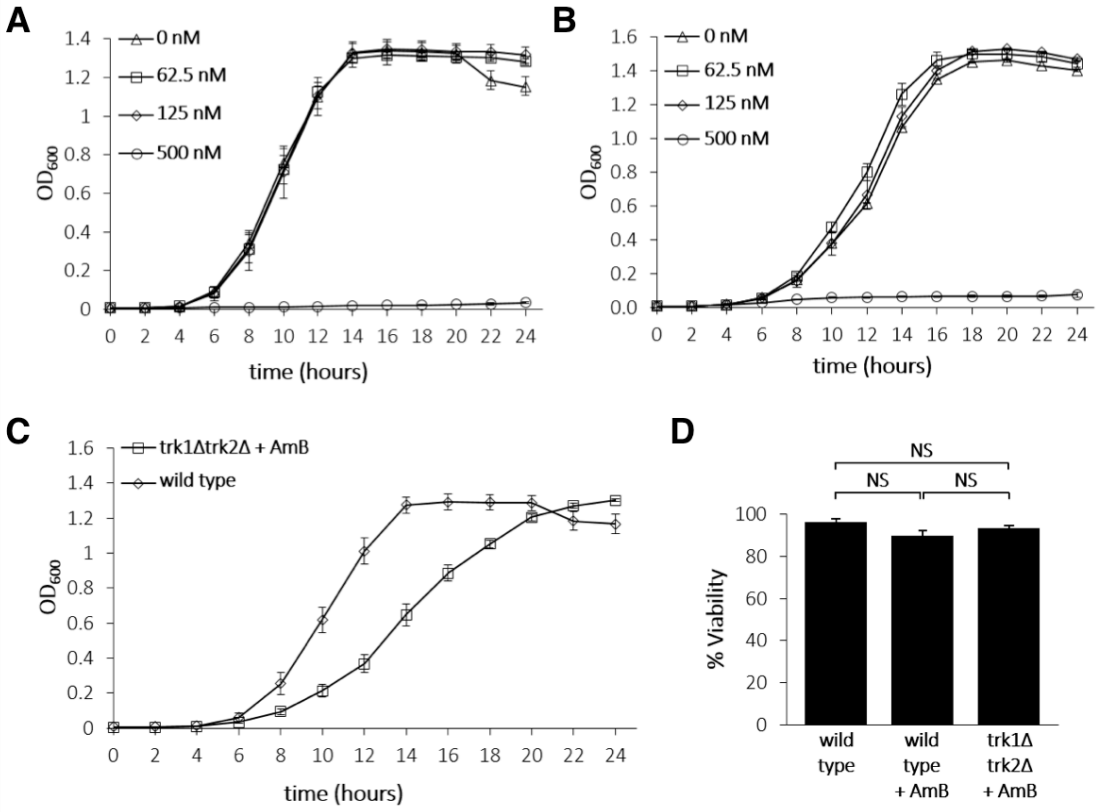

Figure 2.15 AmB does not cause growth stimulatory effects to wild type yeast or trk1Δtrk2Δ yeast when both are grown under permissive high potassium (100 mM KCl) conditions. **(A)** AmB does not cause growth stimulatory effects in wild type cells grown in the presence of 100 mM KCl. Curves represent AmB concentrations of 0 nM, 62.5 nM, and 125 nM. No growth is observed at or above the minimum inhibitory concentration of 500 nM AmB. **(B)** AmB does not cause growth stimulatory effects on trk1Δtrk2Δ cells grown under permissive conditions (100 mM KCl). Curves represent AmB concentrations of 0 nM, 62.5 nM, and 125 nM. No growth is observed at or above the minimum inhibitory concentration of 500 nM AmB. **(C)** Wild type and AmB-rescued (125 nM) trk1Δtrk2Δ yeast growth curve for 24 hours. The same potassium concentration (10 mM) was used in both experiments. The doubling time for wild type and AmB-rescued trk1Δtrk2Δ yeast was 86 ± 2.4 minutes and 144 ± 2.8 minutes, respectively. **(D)** AmB-treated wild type and AmB-rescued trk1Δtrk2Δ cells show no decrease in cell viability compared to wild type as judged by propidium iodide staining. NS, not significant. Graph depicts means ± SEM.

A series of additional experiments confirmed that the observed restoration of cell growth is caused by the small molecule-based ion channel activity. A disc diffusion assay visually revealed the predicted dependence of this growth rescue on the concentration of AmB (Fig. 2.14B). To quantify this concentration dependence and eliminate the potentially complicating issue of plating efficiency (*71*), we also measured trk1Δtrk2Δ yeast cell growth in a broth dilution assay using media containing a normal concentration of potassium (10 mM) (Fig. 2.14C). Consistent

with the disc diffusion results, no cell growth was observed in the absence of AmB, a dose-dependent increase of growth was observed at intermediate concentrations, and no growth was observed at or above the minimum inhibitory concentration of this antifungal agent. Further ruling out any type of generic hormetic effects (*72*), no growth stimulatory effects were observed when wild type cells or trk1Δtrk2Δ cells grown under permissive conditions were treated with AmB (Fig. 2.15A,B). AmB at 125 nM also did not cause any toxicity in these experiments.

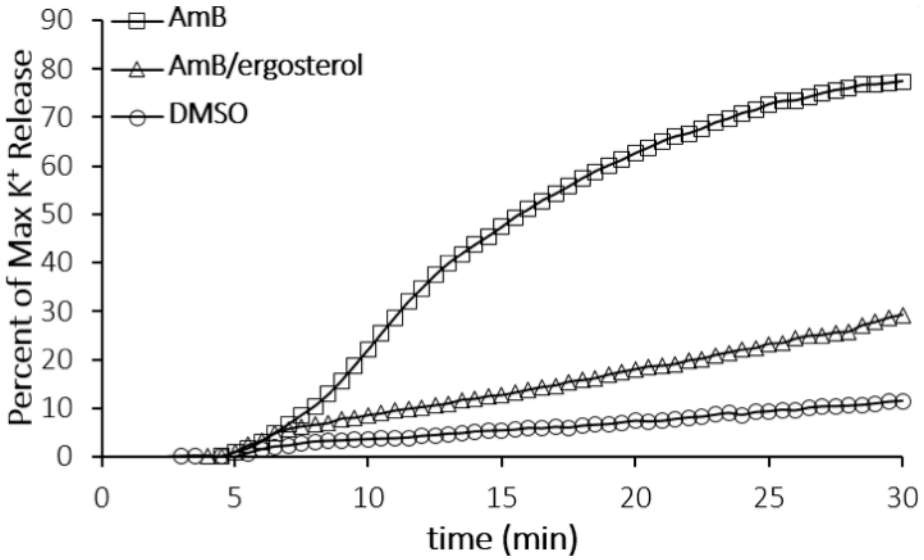

Figure 2.16 Potassium efflux in wild type *S. cerevisiae*. AmB readily permeabilizes wild type *S. cerevisiae* compared to DMSO vehicle. A pre-formed AmB-ergosterol complex still permeabilizes yeast cells. Experiment was performed in triplicate. Plot is representative of each replicate.

To directly probe the importance of the ion channel activity of AmB, we also tested the single atom-deficient variant C35deOAmB, which does not form ion channels (Fig. 2.13B) (*27*). This derivative failed to restore growth in trk1Δtrk2Δ cells at any tested concentration (Fig. 2.14C). In a complementary experiment, we utilized the sterically bulky tetraethylammonium cation to block the AmB-based ion channel (*73*). This cation inhibited the functional complementation observed with AmB in a dose-dependent manner without causing general toxicity (Fig. 2.14D). We also monitored uptake of radioactive $^{86}Rb^{+}$ as a reporter of transmembrane potassium movement (Fig. 2.14E) (*74*). $^{86}Rb^{+}$ uptake was observed in wild

typeyeast but not in the trk1Δtrk2Δ mutant, and no uptake was observed when the trk1Δtrk2Δ mutant was treated with the channel-inactivated derivative C35deOAmB. In contrast, $^{86}Rb^{+}$ uptake was restored when trk1Δtrk2Δ cells were treated with AmB.

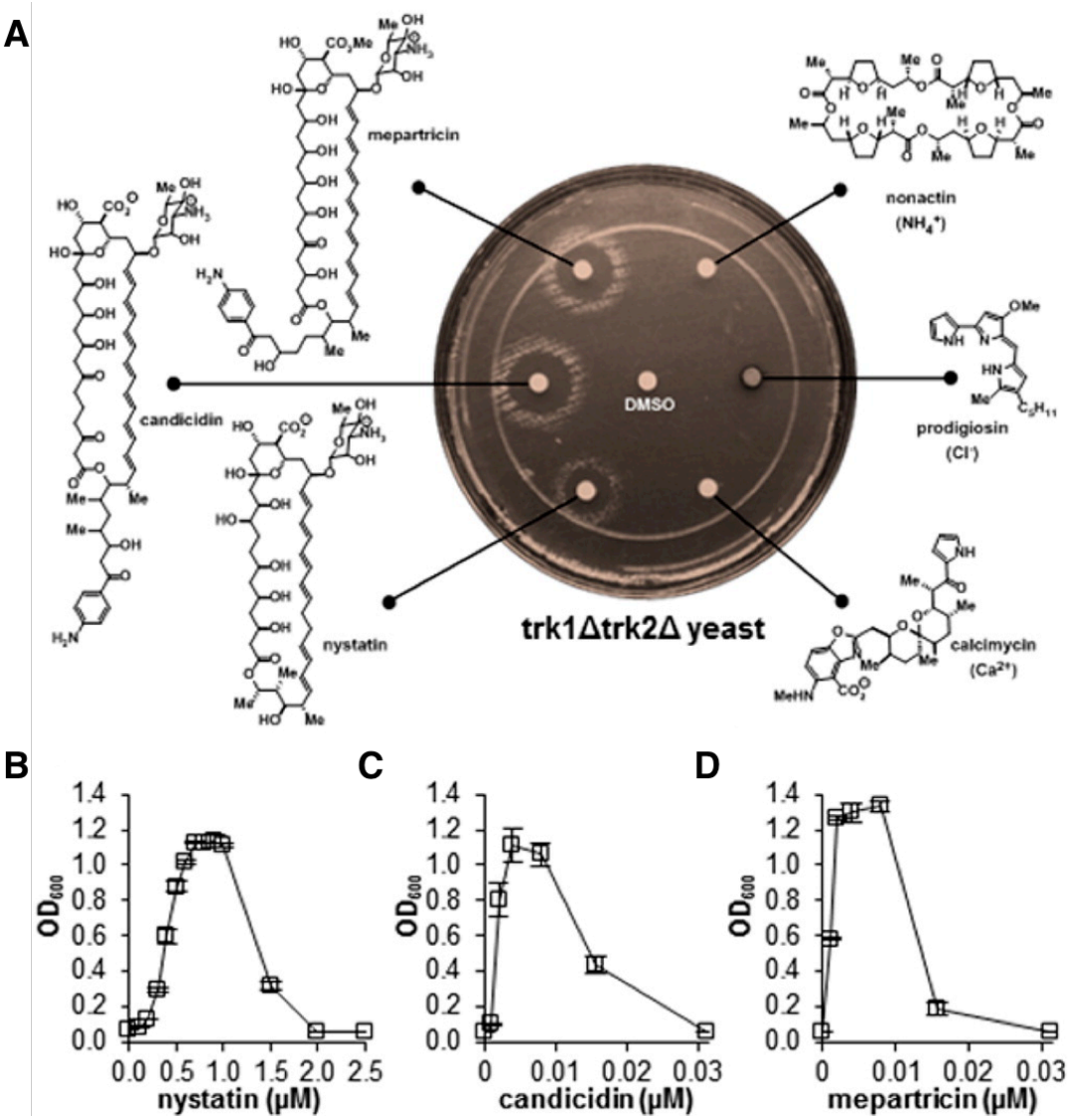

Figure 2.17 Series of potassium-transporting polyene macrolide natural products restore vigorous cell growth in trk1Δtrk2Δ yeast, whereas **(A)** no growth is observed upon treating with other small molecules that selectively transport other ions. **(C-D)** Nystatin, candicidin, and mepartricin were similarly able to restore physiology in a liquid broth dilution assay over a variety of concentrations. Graphs depict means ± SEM.

We further quantified the vigor and sustainability of this AmB ion channel-mediated restoration of yeast cell growth. AmB-treated trk1Δtrk2Δ cells reached a maximum cell density

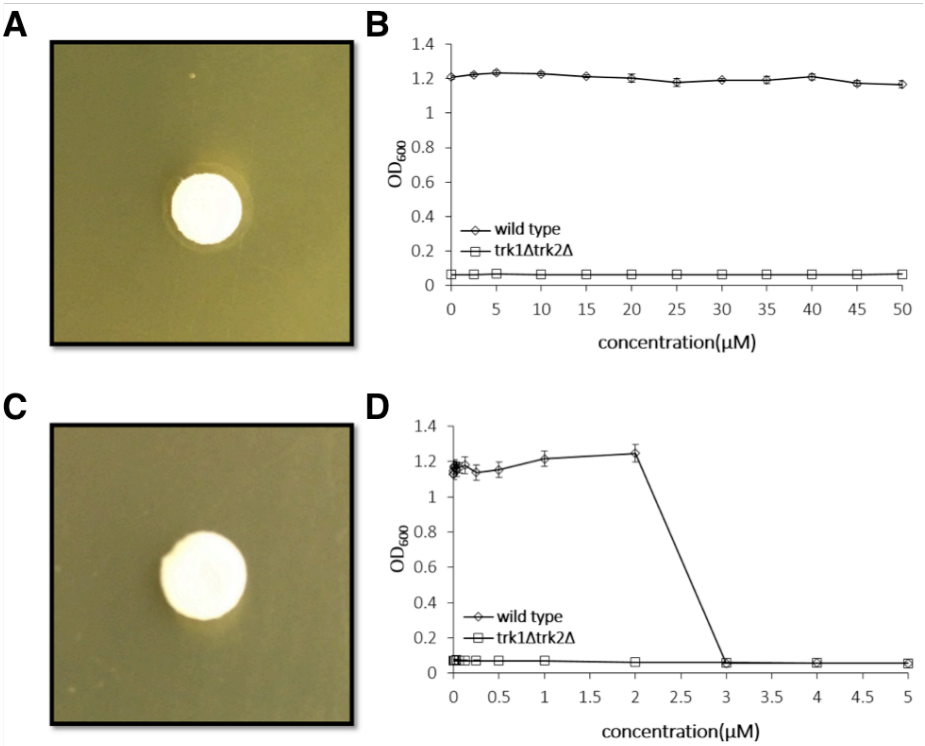

Figure 2.18 (A) The potassium ion carrier valinomycin does not restore trk1Δtrk2Δ cell growth. Disc diffusion assay with valinomycin (4 mg/mL) on an agar plate containing 10 mM potassium and streaked with trk1Δtrk2Δ cells. **(B)** Broth microdilution assay with valinomycin. **(C)** Polyene macrolide natamycin does not restore trk1Δtrk2Δ cell growth. Disc diffusion assay with natamycin (4 mg/mL) on an agar plate containing 10 mM potassium and streaked with trk1Δtrk2Δ cells. **(D)** Broth microdilution assay with natamycin. Graph depicts means ± SEM.

that matched that of the wild type (Fig. 2.14F) and the doubling time for AmB-rescued trk1Δtrk2Δ cells was only 1.7 times longer (Fig. 2.15C). We also observed equivalent levels of cell viability in wild type yeast, wild type yeast treated with 125 nM AmB, and trk1Δtrk2Δ cells rescued with 125 nM AmB (Fig. 2.15D). To probe the sustainability of this rescue effect, we reiterated the max cell density and doubling time experiments for over a month. Like wild type cells, the AmB-rescued trk1Δtrk2Δ cells showed sustained vigorous cell growth throughout this entire period of time (Fig. 2.14G). Removing AmB from the media at any point resulted in rapid loss of growth for the trk1Δtrk2Δ cells. We further confirmed the mechanism-based hypothesis that the preformed AmB:Erg complex discussed in section 2.2 should retain the capacity to permeabilize yeast cells (Fig. 2.16) but show substantially decreased cell killing (*75*). This

preformed complex dramatically extended the range of concentrations over which rescue is observed (Fig. 2.14H).

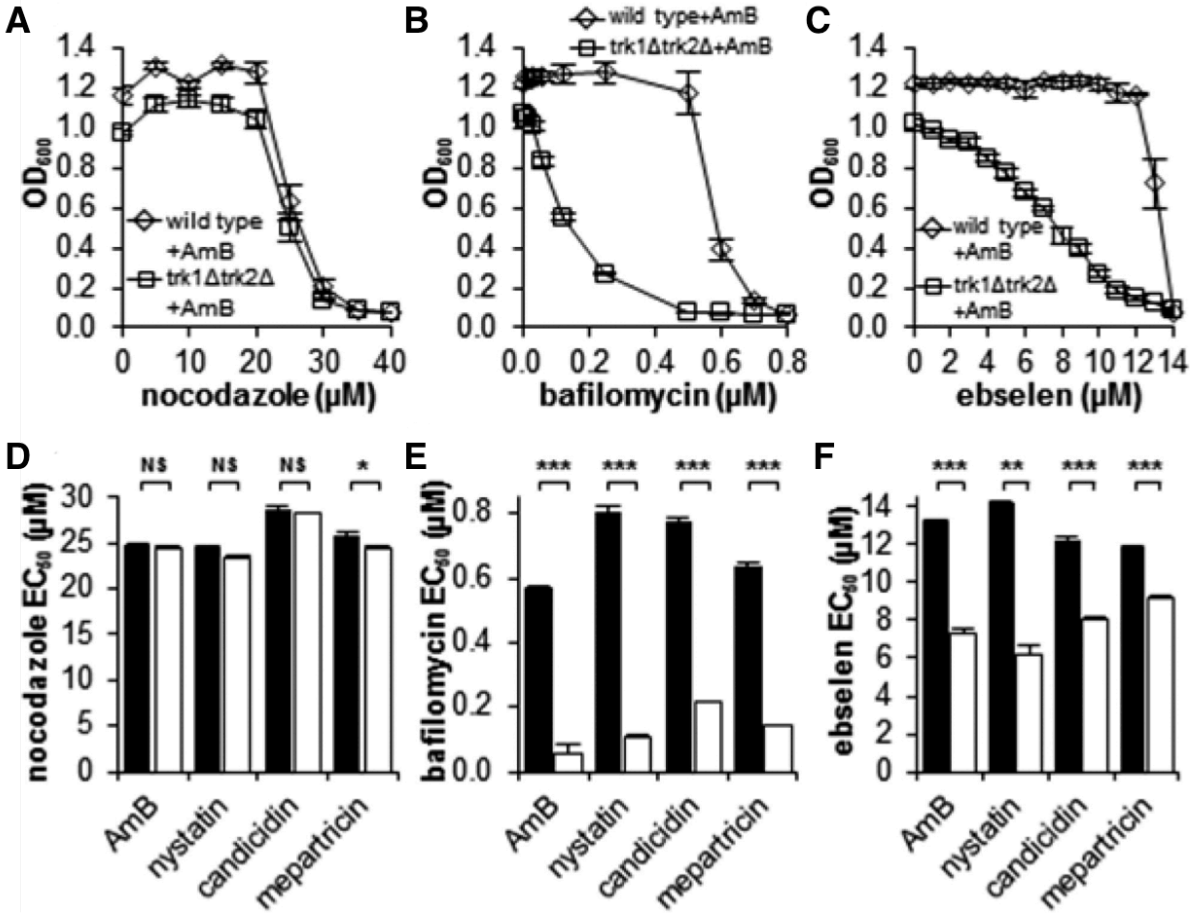

Figure 2.19 (A) AmB-treated wild type *S. cerevisiae* and trk1Δtrk2Δ cells are equally sensitive to the off-pathway microtubule inhibitor nocodazole. **(B)** AmB-rescued trk1Δtrk2Δ cells are substantially more sensitive to the V-ATPase inhibitor bafilomycin compared to wild type cells. **(C)** AmB-rescued trk1Δtrk2Δ cells are substantially more sensitive to the Pma1 inhibitor ebselen than wild type cells. **(D-F)** EC_{50} values for various inhibitors of cell growth against wild type (black bars) and trk1Δtrk2Δ cells (white bars) treated with optimum rescue concentrations of potassium-transporting polyene macrolide natural products AmB, nystatin, candicidin, and mepartricin. NS, not significant. $*P \leq 0.05$. $**P \leq 0.001$. $***P \leq 0.0001$. Graphs depict means ± SEM.

To probe the scope and limitations of this tolerance for imperfect mimicry of missing proteins with small molecules, a series of additional ion transporting natural products were evaluated. Vigorous restoration of trk1Δtrk2Δ cell growth was observed with other small molecules that form potassium ion channels, including nystatin, candicidin, and mepartricin, (Fig. 2.17B-D) but not with those that selectively transport NH_4^+ (nonactin), Cl^- (prodigiosin),

and Ca_2^+ (calcimycin) (Fig. 2.17A). Interestingly, the potassium ion carrier valinomycin (*76*) is unable to restore cell growth (Fig. 2.18A,B).

Finally, we tested the mechanistic hypothesis that these potassium channel-forming small molecules restore physiology by collaborating with the V-ATPase and Pma1 proton pumps. Such a model predicts selective sensitivity of the small molecule-rescued mutants to chemical inhibition of these pumps. As a negative control, AmB-treated wild type and AmB-rescued trk1Δtrk2Δ cells were equally sensitive to nocodazole, an off-pathway inhibitor of microtubule dynamics (Fig. 2.19A). In contrast, AmB-rescued trk1Δtrk2Δ cells were exceptionally sensitive to inhibition of V-ATPase with bafilomycin (Fig. 2.19B) and Pma1 with ebselen (Fig. 2.19C). Similar results were observed with nystatin-, candicidin-, and mepartricin-rescued trk1Δtrk2Δ cells (Figure 2.19D-F).

2.5 SUMMARY

The ability of AmB to form membrane-spanning ion channels has long been thought to primarily contribute to its structure and antifungal activity, seemingly precluding it as a viable candidate for a small molecule prosthetic (*4-23*). In contrast, we found that AmB predominantly forms large extramembranous aggregates that extract Erg from lipid bilayers and thereby kill yeast. Membrane-inserted ion channels are relatively minor contributors, both structurally and functionally, to the antifungal action of this natural product. While previous studies have reported large aggregates of AmB or its derivatives (*17, 21*), the interpretation of these findings has been in terms of the ion channel model. Here we described PRE, ^{1}H spin diffusion trajectory, and TEM studies that collectively demonstrated that AmB primarily exists in the form of large extramembranous aggregates. Moreover, changes in PREs, ^{1}H spin diffusion trajectories, T_1 relaxation, order parameters, line widths, and chemical shift perturbations, as well as the

observation of direct intermolecular cross peaks and the results of cell-based ergosterol extraction experiments demonstrated that extramembranous aggregates of AmB directly bind Erg. We further confirmed that the AmB aggregates we observed in our SSNMR, TEM, and cell-based experiments were similar. Collectively, these results strongly support the proposed sterol sponge model in which extramembranous aggregates of AmB extract ergosterol from phospholipid bilayers and thereby kill yeast, independent of channel formation.

These findings revealed two unique strategies with which to approach testing AmB as a small molecule ion channel mimic. Our first approach to separating the channel activity of AmB from its cell killing activity was simply using low concentrations, staying below the toxic ratio of AmB to sterol. The second approach was to use a preformed AmB:Erg complex, which maintains its channel-forming capacity while mitigating toxicity. Using these two strategies guided by our previous work, we concluded that imperfect small molecule mimics of missing protein ion transporters can restore physiology in yeast, and evidence supports that this phenomenon is attributable to functional collaboration between small molecule channels and protein ion pumps. A common channels and pumps architecture is responsible for directional ion movement in organisms from yeast to humans (*62*), suggesting that the same type of functional collaboration observed herein might enable small molecule surrogates for missing protein ion channels to have an impact on human health. Therefore, our two strategies for AmB as a molecular prosthetic are well positioned for further testing in a human disease model system.

2.6 METHODS

Materials. Commercially available materials were purchased from Sigma-Aldrich, Alfa Aesar, Avanti Polar Lipids, Cambridge Isotope Laboratories, or Fisher Scientific and were used without further purification unless stated otherwise. Natural abundance amphotericin B (AmB) was

purchased from Sigma-Aldrich or a gift from Bristol-Myers Squibb Company. Unless stated otherwise, all solvents were dispensed from a solvent purification system that passes solvents through packed columns according to the method of Pangborn and coworkers (*77*) (THF, Et_2O, CH_2Cl_2, toluene, dioxane, hexanes: dry neutral alumina; DMSO, DMF, CH_3OH: activated molecular sieves). Water was dispensed from a MilliQ water purification system (Millipore Corporation, Billerica, MA).

Purification and analysis. Preparative scale HPLC purification was performed using an Agilent 1260 series instrument equipped with a multiple-wavelength detector and a Waters SunFire Prep C18 OBD 5 μm 30×150 mm column at a flow rate of 25 mL/min. All HPLC solvents were filtered through 0.2 μm Millipore filters prior to use. UV/Vis analyses were performed on a Shimadzu PharmaSpec UV-1700 spectrophotometer. Electrospray ionization mass spectra (ESI-MS) were obtained at the University of Illinois mass spectrometry facility.

Amphotericin and amphoteronolide B. Due to light and air sensitivity of polyenes, all manipulations of AmB and amphoteronolide B (AmdeB) were carried out under low-light conditions and compounds were stored under a dry argon atmosphere at −20 °C. AmdeB was prepared synthetically from natural abundance AmB as previously described (*25-27*). All AmB and AmdeB used for current experiments were purified by preparative scale HPLC. All manipulations of HPLC-purified AmB and AmdeB were performed using either Optima MeOH, 0.2 μm-filtered HPLC grade solvents, or solvents dispensed from a solvent purification system (*77*).

For purification, solid AmB was dissolved in DMSO (10 mg/mL), filtered through Celite 545 and purified (100 μL injections) with gradient of 5% to 65% MeCN / 5 mM ammonium acetate (NH_4OAc) over 12 minutes with detection at 406 nm. The column was subsequently flushed

with isocratic 95% MeCN / 5 mM NH4OAc for 2 min and re-equilibrated to 5% MeCN / 5 mM NH_4OAc prior to the next injection. The combined AmB solution was concentrated in vacuo, with filtered (0.2 μm) MeCN added back to the flask as needed for azeotropic removal of water. The resulting yellow solid was suspended via bath sonication in 1:1 MeCN:toluene and again concentrated *in vacuo* for azeotropic removal of residual NH_4OAc. Residual solvent was removed under high vacuum for ≥ 8 h to furnish a pale yellow solid, which was stored under argon at −20 °C.

AmdeB was dissolved in DMF, filtered (Celite 545), injected, and eluted with a mobile phase gradient of 5% to 95% MeCN / 5 mM NH_4OAc over 25 min.

Biosynthesis of [U-^{13}C]AmB. [U-^{13}C]AmB was prepared using a modified version of the method previously reported (*18*), with [U-^{13}C]glucose replacing natural abundance fructose in the culture medium. All simple carbon sources were thus uniformly ^{13}C-labeled, resulting in unprecedented isotopic enrichment of >80%, as measured by mass spectrometry. After work up and precipitation, [U-^{13}C]AmB was purified by gradient C18 chromatography followed by HPLC.

Erg preparation. Natural abundance Erg was purchased from Sigma-Aldrich and recrystallized from EtOH before use. Stock solutions of 4 mg/mL Erg in $CHCl_3$ were stored under argon at −20 °C for up to 1 month. [^{13}C]Erg was prepared biosynthetically using the method previously described (*19, 78*).

Solid-state NMR spectroscopy. SSNMR experiments were performed using a 600 MHz InfinityPlus spectrometer (Varian, now a subsidiary of Agilent Technologies, Inc.) equipped with a 3.2 mm T3 HXY MAS probe tuned to ^{1}H-^{31}P-^{13}C mode. Pulse widths (π/2) for ^{1}H, ^{13}C, and ^{31}P were 2–2.5 μs, 3.2 μs, and 3.2 μs, respectively. Spinning was controlled with a Varian MAS

controller to 10,000 ± 2 Hz. SPINAL-64 decoupling (~75 to 80 kHz) was used during evolution and acquisition periods.53 The flow rate of sample cooling gas was maintained at 100 scfh at 20 °C, resulting in a calibrated sample temperature of 19.2±1 °C. Chemical shifts were referenced externally with adamantane, with the downfield ^{13}C resonance referenced to 40.48 ppm (*79*).

^{13}C T_1 and PRE experiments. T_1 values were measured using standard T_1 inversion recovery pulse sequence with a 5 second pulse delay. Data were processed and fit with Varian Spinsight software version 4.3.2. For each of the resolved methine and methylene in [U-^{13}C]AmB and [^{13}C]Erg, the longitudinal ^{13}C PRE was obtained by calculating the difference between the ^{13}C R_1 values for sample with and without 5 mol% of the DOXYL lipids, determined by modeling the individual relaxation trajectories as single exponential decays. T_1 trajectories were fit using the integrated volume of a given peak as a function of delay time (tau_1); integration boundaries were set to the linewidth at half height. The average line widths were ~40–60 Hz for POPC, ~50 Hz for Erg with no AmB present, 127 Hz with AmB present, and ~187 Hz for AmB alone.

^{1}H-^{13}C spin-diffusion experiments. We performed ^{1}H-^{13}C spin-diffusion correlation experiments as previously described (*41*) using a 1 ms T_2 filter, to detect interactions between the mobile 1H signals of lipid acyl chains (1.35 ppm) and/or water (4.7 ppm) with the [U-^{13}C]AmB, and [^{13}C]Erg in the presence and absence of AmB. ^{1}H-^{13}C polarization transfer trajectories were extracted from ^{1}H-^{13}C two-dimensional spectra collected with ^{1}H-^{13}C mixing times ranging from 1 ms to 625 ms, by fitting peaks with a minimum signal to noise of 5, using a box integration method in Sparky. Trajectories were then normalized based on maximum observed intensity for a single resolved water or lipid ^{1}H-^{13}C cross peak after correction for ^{1}H T_1 relaxation, which was measured in a separate T_1 inversion recovery experiment. Error bars are derived from the signal-to-noise ratios observed for each crosspeak.

Order parameters from ^{1}H-^{13}C dipolar couplings. Dipolar order parameters (S) were measured using the T-MREV pulse sequence (*44*) at an MAS rate of 8.333 kHz (N=4 condition, 100 kHz ^{1}H decoupling nutation frequency, 2.5 μs ^{1}H π/2 pulse length). The T-MREV ^{13}C-^{1}H dephasing was incremented by 30 μs and a total of 25 increments were recorded in t1. Fortran fitting routines (*80*) were used to determine the ^{13}C-^{1}H dipolar coupling, taking into account the effects of relaxation and contributions from weaker couplings from neighboring protons. We calibrated the scaling factor of the T-MREV sequence by measuring the ^{13}C-^{1}H dipolar coupling for crystalline N-acetyl-L-valine under the identical experimental conditions.

[^{1}H]-^{13}C-[^{1}H-^{1}H]- ^{13}C correlation spectra. [^{1}H]-^{13}C-[^{1}H-^{1}H]- ^{13}C SSNMR experiments to yield performed at 10 °C, at an MAS rate 11.628 kHz, with the heteronuclear contact time (t_{HC}) set to 400 μs, and 1H-1H mixing time of 400 μs. These conditions reveal cross peaks for internuclear ^{13}C-^{13}C distances of ~4–6 Å. In order to properly identify new intermolecular AmB-Erg cross peaks the [^{1}H]-^{13}C-[^{1}H-^{1}H]- ^{13}C spectra were acquired back-to-back under identical conditions, including and signal averaging, adjusting the total measurement time based on the amount of material. The rotors of POPC/[U-^{13}C]AmB/Erg (10:1:1 molar ratio) and POPC/[U-^{13}C]AmB/[^{13}C]Erg (10:1:1 molar ratio) were packed with ~25 mg and the spectra signal averaged for 7.8 days each. The 10:1:1 POPC/AmB/[^{13}C]Erg sample was ~16 mg and therefore signal averaged for 13.6 days. The three spectra were all processed identically, with 40 and 75 Hz ^{13}C line broadening applied in the direct and indirect dimensions, respectively.

Preparation of stock solutions for SSNMR. A fresh stock solution of HPLC-purified AmB (natural abundance or [U-^{13}C]AmB) was prepared for each experiment by dissolving AmB in a large volume of Optima methanol, typically 75–100 mL for 10 mg of AmB. Stock solution

concentration was measured in triplicate by dilution in MeOH and measuring absorbance at 406 nm (ε_{406} = 146000 M^{-1} cm^{-1}) (*25*).

Stock solutions of Erg were prepared by dissolving recrystallized (commercial) or HPLC-purified (biosynthetic) Erg in a minimum volume of $CHCl_3$ and the concentration determined by UV/Vis spectroscopy (ε_{282} = 10,400 M^{-1} cm^{-1}) (*26*). Erg stock solutions were stored in I-Chem vials under a dry argon atmosphere at −20 °C for up to 1 month.

Phospholipids were purchased as stock solutions in $CHCl_3$ and these solutions were used directly for liposome preparation. Unused phospholipid solutions were stored in vials/bottles under a dry argon atmosphere at −20 °C, and discarded after 1 month.

Preparation of liposome vesicles for SSNMR. Liposomes were prepared using a modified version of the protocol previously reported (*18*). A suspension of POPC/Erg/AmB in 1:1 $CHCl_3$/MeOH was prepared as follows: The desired amount of AmB stock solution (typically 30–40 mL) was concentrated *in vacuo* to 2–3 mL and transferred to a 7 mL Wheaton vial, with three Optima MeOH washes to ensure complete transfer. This resulting AmB suspension was concentrated *in vacuo*. The desired amounts of stock solutions of phospholipid and Erg were then added via Hamilton gastight syringe, and an equivalent volume of Optima MeOH was added to resuspend the AmB. The vial was capped and this suspension was briefly vortexed and bath-sonicated until no AmB remained adherent to the sides of the vial (2–3 cycles). Solvent was removed under a gentle stream of nitrogen gas. Residual solvent was removed under high vacuum for ≥8 h.

To the dried solid was added filter-sterilized 0.3 mM HEPES buffer, pH 7.0 to yield a final phospholipid concentration of 40 mM. This aqueous suspension was vortexed and sonicated 3 times or until a homogeneous suspension was observed. Samples were then submitted to 5

freeze/thaw cycles (liquid nitrogen, lukewarm tap water). Samples were again frozen in liquid nitrogen and lyophilized for ≥8 h. The lyophilization chamber was then back-filled with dry argon to prevent samples from absorbing ambient water. Samples were immediately capped and packed into rotors for SSNMR as soon as possible.

Dry samples were packed in 3.2-mm-diameter-limited-speed SSNMR rotors (Agilent Technologies, Inc.) and hydrated with 8–10 μL of MilliQ H_2O. Rubber discs were used in the rotors to maintain hydration levels by creating a seal. Samples were placed at 4 °C for at least 24 hours to allow water to equilibrate.

General information for electron microscopy. LUVs were prepared by the method reported previously (*26, 27*), and AmB was added to the LUV suspension as a freshly-prepared DMSO stock solution. Microscopy was performed using a 120-keV FEI Spirit Transmission Electron Microscope. Images were recorded using a bottom mount TVIPS CMOS based camera system at nominal magnifications of 23,000–49,000x at the specimen level. Measurements were taken in ImageJ32 (v 1.47).

Sample preparation for electron microscopy. AmB was prepared as a stock DMSO solution (8.82 mM). 5 μL of the stock AmB solution was added to 95 μL of the 50x-diluted LUV solutions. For AmB-free samples, 5 μL of DMSO was added to 95 μL of the 50x-diluted LUV solutions. Samples were vortexed gently for 5 seconds then incubated at 37 °C for 1 hour. EM samples were prepared as previously described (*81*) with the following modifications. A 4 μL drop of the sample was applied to a negatively charged carbon-coated copper grid (Gilder 200 mesh, Ted Pella, Inc., Redding CA) for 30 seconds. Subsequently, two drops of freshly prepared 2% uranyl acetate were added to the sample and incubated for 1 minute before drying via aspiration. Samples were then screened on the electron microscope.

Growth conditions for *S. cerevisiae* for *in vivo* sterol extraction and membrane isolation. *S. cerevisiae* was grown in autoclave-sterilized yeast peptone dextrose (YPD) media consisting of 10 g/L yeast extract, 20 g/L peptone and 20 g/L of filter-sterilized dextrose added as a sterile 40% w/v solution in water. Solid media was prepared by pouring sterile media containing agar (20 g/L) onto Corning (Corning, NY) 100×20 mm polystyrene plates. Liquid cultures were incubated at 30 °C on a rotary shaker and solid cultures were maintained at 30 °C in an incubator.

Sample preparation for *in vivo* sterol extraction and membrane isolation. 750 mL overnight cultures of *S. cerevisiae* were grown to stationary phase (OD_{600} of ~1.7 as measured with a Shimadzu PharmaSpec UV-1700 UV/Vis spectrophotometer). This culture was divided equally into 50 mL Falcon centrifuge tubes.

Stock solutions of AmdeB, AmB, and Erg were prepared in DMSO. Methyl-β-cyclodextrin (MBCD) was added directly to the liquid culture. Cells were treated with either a DMSO only control, 5 μM AmdeB, or 5 μM AmB for 1, 30, 60, or 120 minutes. Cells were treated with DMSO control, 500 mM MBCD, 25 μM Erg control, and the 5 μM AmB:25 μM Erg complex for 120 minutes. Treated tubes were incubated on the rotary shaker (200 rpm) at 30°C for the time of exposure.

For the quantification of colony forming units (CFUs), at the end of exposure, aliquots were taken from the samples, diluted, and plated on YPD agar plates. The plates were then incubated for 48 hours at 30°C and colony-forming units were counted.

For the quantification of percent ergosterol remaining, yeast membranes were isolated using a modified version of Haas' spheroplasting and isosmotic cell lysis protocol and simple differential ultracentrifugation (*45*). At the end of the exposure time, tubes were removed from

the shaker and centrifuged for 5 minutes at 3000 μg at room temperature. The supernatant was decanted and 5 mL of wash buffer (dH_2O, 1M DTT, 1M Tris-HCl, pH 9.4) was added. The tubes were vortexed to resuspend and incubated in a 30°C water bath for 10 minutes. Tubes were then centrifuged again for 5 minutes at 3000 μg and the supernatant decanted.

1 mL of spheroplasting buffer (1M KPi, YPD media, 4M sorbitol) and 100 μL of a 5 mg/mL solution of lyticase from *Arthrobacter luteus* (L2524 Sigma-Aldrich) was added to each tube, and each tube was then vortexed to resuspend. Tubes were incubated in a 30°C water bath for 30 minutes, with occasional swirling. After incubation, tubes were centrifuged for 10 minutes at 1080 μg at 4 °C and the supernatant decanted.

1 mL of PBS buffer and 20 μL of a 0.4 mg/ml dextran in 8% Ficoll solution was added to each tube, mixed very gently to resuspend. This suspension was placed on ice for 4 minutes and then heat-shocked in a 30°C water bath for 3 minutes.

The suspensions were then transferred to Eppendorf tubes, vortexed to ensure complete lysis, and centrifuged at 15000 μg at 4 °C for 15 minutes to remove un-lysed cells and cell debris. The resulting supernatants were transferred to thick-wall polycarbonate ultracentrifuge tubes (3.5 mL, 13×51 mm, 349622 Beckman Coulter) and spun for 1 hour at 100,000 μg at 4°C in a Beckman Coulter TLA-100.3 fixed-angle rotor in a Beckman TL-100 Ultracentrifuge. The supernatant was poured off. The remaining membrane pellet was resuspended in 1 mL PBS buffer and stored at −80 °C until further analysis.

Gas chromatography quantification of sterols. 750 μL of each membrane pellet sample and 20 μL of internal standard (4 mg/mL cholesterol in chloroform) were dissolved in 3 mL 2.5% ethanolic KOH in a 7 mL vial, which was then vortexed gently, capped, and heated in a heat block on a hot plate at 90°C for 1 hour. The vials were then removed from the heat source and

allowed to cool to room temperature. 1 mL of brine was added to the contents of each vial. Extraction was performed twice, each with 3 mL of hexane. Organic layers were removed in both extractions, dried over magnesium sulfate, filtered through Celite® 545 (Sigma-Aldrich), and transferred to another 7 mL vial. The contents of the vial were then concentrated in vacuo in a 30°C water bath.

The resulting sterol films were resuspended in 100 µL pyridine and 100 µL *N,O*-bis-(trimethylsilyl)-trifluoroacetamide with 1% trimethylchlorosilane (T6381-10AMP Sigma-Aldrich) by vortexing gently (*82*). This solution was heated at 60 °C for 1 hour. The vials were placed on ice and the solvent was evaporated off by nitrogen stream. Vials must be kept at a low temperature to prevent evaporation of the sterol TMS ethers along with the solvent. The resulting films were resuspended in 100 µL of decane, filtered and transferred to a GC vial insert for analysis.

Gas chromatography analysis was carried out on an Agilent 7890A gas chromatograph equipped with a FID, an Agilent GC 7693 Autosampler, and a Dell computer running Microsoft XP that utilizes ChemStation v.B.04.02 SP1. Samples were separated on a 30 m, 0.320 mm ID, 0.25 um film HP-5 capillary column (19091J-413 Agilent) using hydrogen as a carrier gas with an average velocity of 84.8 cm/s. Nitrogen make-up gas, hydrogen and compressed air were used for the FID. A split/splitless injector was used in a 20:1 split. The injector volume was 2 µL. The column temperature was initially held at 250 °C for 0.5 min, then ramped to 265 °C at a rate of 10 °C /min with a final hold time of 12.5 min. The injector and detector temperature were maintained at 270 °C and 290 °C, respectively. The value reported for each time point was calculated by dividing the value for the treatment group by the value for the DMSO control at the same time point, and then normalizing the DMSO control to 100%.

Preparation of an AmB:Erg complex. Erg was prepared as a stock solution, 4 mg/mL in $CHCl_3$, and the solvent removed under a gentle stream of nitrogen gas. Residual solvent was removed under high vacuum for at least 8 h. A DMSO solution of 5 μM AmB was then added to this solid Erg (25 μM final Erg concentration, 5:1 mole ratio Erg:AmB). The resulting suspension was gently vortexed and then heated to 80 °C for one hour in an aluminum heating block to allow Erg to fully dissolve. The resulting AmB/Erg solution was then allowed to cool to room temperature. This solution was left to complex at room temperature for another hour before use.

The absorbance spectra of the two types of aggregate, (1) 5 μM AmB only in PBS buffer, (2) 5 μM AmB:25 μM Erg complex in PBS buffer, and the monomeric form of AmB (AmB in 25% PBS buffer, 75% methanol) were investigated using a Shimadzu PharmaSpec UV-1700 UV/Vis spectrophotometer (*83*).

UV/Vis melting curve assays. 200 μM stock solutions of the compounds to be tested were prepared. The AmB:sterol complex was prepared as described in the previous section. A UV/Vis spectrophotometer with a Peltier temperature module was used for these assays. The UV/Vis was first blanked with a solution of 2 mL methanol and 50 μL DMSO at room temperature (~25^{o}C). 50 μL of the compound solution was added to 2 mL methanol, pipetted into the cuvette, and read from 300 to 500 nm. The monomer peak was at around 409 nm (rightmost peak). To examine aggregate melting, 50 μL of the compound solution was added to 2 mL PBS buffer, pipetted into the cuvette, and read from 300 to 500 nm. The aggregate appears as a large peak on the left. The Peltier temperature control was set to take a new scan every 5^{o}C. The leftmost aggregate peak disappeared and the monomer peak at 409nm increased with temperature, indicating movement

towards the monomeric species. The absorbance value was plotted at the 409nm peak versus temperature.

Growth conditions for *S. cerevisiae* for rescue experiments. All growth rescue experiments were performed using the same normal concentration of potassium (10 mM) for both wild type *S. cerevisiae* (ATCC 9763) and trk1Δtrk2Δ *S. cerevisiae* (SGY 1528). This yeast peptone adenine dextrose (YPAD) growth media consisted of 10 g/L yeast extract, 20 g/L peptone, 20 g/L dextrose, 0.015 g/L adenine hemisulfate salt (final potassium concentration = 10 mM), and the media was adjusted to pH 5.0 using citric acid. For culturing on solid media, 20 g/L agar was added to this same mixture. After autoclave sterilization, dextrose was subsequently added as a sterile 40% w/v solution in water (dextrose solutions were filter-sterilized using a 0.22 μm filter). As previously described (*84*), to culture trk1Δtrk2Δ prior to performing these experiments, additional potassium was added in the form of potassium chloride (100 mM KCl) to the same (YPAD) growth media ("permissive conditions"). To ensure the same conditions for both strains, wild type yeast were also cultured prior to performing these experiments under the same permissive conditions. Overnight liquid cultures were incubated at 30 °C on a rotary shaker (200 rpm). Wild type stock cultures were maintained on solid YPAD media at 4 °C, and trk1Δtrk2Δ stock cultures were maintained on solid YPAD media under permissive conditions (100 mM KCl) at 4 °C.

Growth rescue assay on solid media. These growth rescue experiments were performed using solid media prepared as described above containing normal concentrations of potassium (10 mM). For solid media containing AmB (AK Scientific), the same media was allowed to cool for 15 minutes before addition of AmB as a solution in DMSO to provide a final concentration of

125 nM AmB. Cultured yeast diluted to an OD_{600} of 0.1 was streaked onto these plates, and plates were examined for growth after 24-48 hours of incubation.

Disc diffusion assay. The assay was performed using a previously described protocol (*85*). Discs containing either DMSO vehicle or the indicated small molecule were added. For AmB, nystatin, candicidin, and mepartricin, 10 μL of either a 4 mg/mL or 1 mg/mL solution were added to the disc and growth was observed in all cases. The data pictured in Figs. 2.12 and 2.15 represent the results observed with 1 mg/mL. For nonactin, prodigiosin, calcimycin, natamycin, and valinomycin, 10 μL of a 4 mg/mL solution were added to the discs, and in all cases no growth was observed. A normal media concentration of potassium (10 mM) was used for all experiments.

Broth microdilution assay. The protocol was adapted from the minimum inhibitory concentration assay described in the Clinical and Laboratory Standards Institute document M27-A23 with the following modifications: After culturing as described above, wild type or trk1Δtrk2Δ yeast were transferred to normal potassium (10 mM) YPAD liquid media adjusted to pH 5.0 using citric acid containing DMSO vehicle or the indicated concentration of the indicated small molecule and growth was monitored at 24 h via UV/Vis spectroscopy (OD_{600}). The experiments in Fig. 2.13 were performed the same way but using media to which was added 100 mM KCl.

Tetraethylammonium block assay. The broth microdilution assay described above was performed with the addition of the indicated concentration of tetraethylammonium to trk1Δtrk2Δ yeast in YPAD media containing the normal concentration of potassium (10 mM) and 125 nM AmB. The control experiment was performed by adding the indicated concentration of tetraethylammonium to trk1Δtrk2Δ yeast in YPAD media to which was added KCl (100 mM).

$^{86}Rb^{+}$ uptake assay. The procedure for $^{86}Rb^{+}$ uptake was adapted from Mulet and coworkers (*86*). Yeast were cultured overnight as described above. After centrifugation, the supernatant was poured off, and the cells were resuspended in sterile water. This wash was repeated two more times. The cells were then resuspended in 40 mL of the potassium starvation/uptake buffer (50 mM succinic acid, 2% glucose, adjusted to pH 5.5 with Tris). The same buffer was used for all experiments for both trk1Δtrk2Δ and wild type yeast. After 3-hour incubation in the potassium starvation buffer, cells were centrifuged and washed twice with sterile water. Cells were resuspended in 1 mL of the potassium starvation/uptake buffer. Cell concentration was determined using an INCYTO Neubauer disposable hemocytometer, and wild type *S. cerevisiae* and trk1Δtrk2Δ cells were diluted to the same cell density ($3x10^7$ cells/mL). 700 µL of the yeast suspension was added to a 1.5 mL Eppendorf tube. After a 5-minute preincubation in the potassium starvation/uptake medium, trk1Δtrk2Δ yeast were then treated with DMSO solutions of AmB or C35deOAmB (final concentration 3 µM). $^{86}RbCl$ (1.1 µCi) was then added to the reaction mixtures. Reaction mixtures were vortexed to ensure a homogeneous solution. At the indicated times, the uptake reaction was stopped by taking a 100 µL aliquot from the reaction mixture and diluting with 10 mL of ice-cold 20 mM $MgCl_2$. Cells were then collected via vacuum filtration through a 0.45-µm-pore-size nitrocellulose filter (Millipore HAWP). Cells were washed with two 15 mL aliquots of 20 mM ice-cold $MgCl_2$. Moist filters were transferred to plastic vials for measuring radioactivity. Radioactivity was monitored using a Perkin Elmer Wizard2 automatic gamma counter. Results are reported in counts per minute as an average of three biological replicates.

Cell viability assay. Assay was adapted from Corliss and coworkers (*87*). Wild type and trk1Δtrk2Δ cells were inoculated in high potassium (100 mM KCl) YPAD media. Starter

cultures were grown at 30 °C for 14-15 hours. Cells were then cultured in high potassium YPAD at 30 °C for 2-2.5 hours. 100 µL of a 0.25 mg/mL propidium iodide (PI, Sigma-Aldrich P4864) solution was prepared. After 2-2.5 hours, cells were centrifuged at 23 °C at 800g for 5 minutes. The supernatant was decanted, cells were resuspended in 40 mL of high potassium YPAD, vortexed, and centrifuged. The wash step was repeated. After pouring off the supernatant, cells were resuspended in 15 mL of high potassium YPAD, vortexed, and diluted to an OD_{600} of 0.5. To set one (WT, WT + PI, trk1Δtrk2Δ, and trk1Δtrk2Δ + PI) and set two (WT + PI + AmB, trk1Δtrk2Δ + PI + AmB), 26.4 µL of DMSO were added to 1 mL aliquots of WT and trk1Δtrk2Δ, and incubated at 30 °C for 30 minutes. A 1% w/v low gelling temperature agarose (Sigma-Aldrich A9414) was prepared in normal potassium (10 mM) YPAD. When set one incubation completed, cells were pulse centrifuged, supernatant was removed, and cells were resuspended in normal potassium YPAD to wash. Cells were centrifuged and resuspended in 250 µL of normal potassium YPAD. Afterwards, 1 µL of 0.25 mg/mL PI dye was added to appropriate samples and 250 µL of 1% agarose was added. Samples were plated onto microscope slides with cover slips and were incubated in humidity chambers for 24 hours at 30°C. For set two, cells were resuspended in normal potassium YPAD containing 125 nM AmB. Cells were resuspended in 250 µL of normal potassium YPAD containing 250 nM AmB before adding to 1% agarose (to obtain 125 nM AmB final). Confocal microscope (Zeiss LSM700) images were taken at 40x where ~15 random images were taken per slide, per treatment group, per experiment. The total number of PI stained cells was subtracted from the total cells recorded, and divided by total cells to give % viability. At least 200 cells were recorded per treatment group and 4 independent sets of data were obtained.

Doubling time and sustainable restoration of cell growth assay. Wild type and trk1Δtrk2Δ yeast were treated as described in the broth microdilution assay described above, with the trk1Δtrk2Δ yeast treated with 125 nM AmB. The OD_{600} was measured at time zero and then every hour for 24 hours. Wild type yeast were then streaked onto normal potassium (10 mM) YPAD agar plates and AmB-rescued trk1Δtrk2Δ yeast were streaked onto AmB-containing (125 nM) normal potassium (10 mM) YPAD agar plates. These agar plates were then incubated at 30 °C for about 48 hours. The same procedure was then repeated for over 42 days, measuring the max OD_{600} and doubling time every three days. Doubling time was determined using the following equation: $T_d = (t_2\text{-}t_1) \times [\log(2)/\log (q_2/q_1)]$, where t_2 and t_1 represent the time at the two points and q_2 and q_1 represent the OD_{600} values in the exponential phase of growth (OD_{600} from 0.2 to 0.6).

Potassium efflux assay. Performed as previously described (*27*).

Sensitivities to chemical inhibitors assay. Broth microdilution assays were performed as described above with the following changes: prior to harvesting cells, small molecules AmB, nystatin A1 (Riedel-de-Haen), candicidin (TOKU-E), or mepartricin B (Santa Cruz Biotechnology) and chemical inhibitors nocodazole (Sigma-Aldrich), ebselen (Cayman Chemical) (*88*), or bafilomycin B1 (Santa Cruz Biotechnology) (*89*) were prepared as stock solutions in DMSO. Saturated cell cultures were centrifuged for 5 minutes at 1000g. The supernatant was poured off, and cells were resuspended in sterile MilliQ water. Cells were centrifuged again, and supernatant was poured off. The wash step was repeated. The supernatant was poured off, and cells were resuspended in normal potassium (10 mM) YPAD. Cells were diluted with normal potassium (10 mM) YPAD to an OD_{600} of 0.01. Next, an appropriate volume of AmB, nystatin A1, candicidin, or mepartricin B solution was added to give a final rescuing

concentration of 125 nM, 1000 nM, 8 nM, and 8 nM, respectively. A control was prepared by adding the corresponding volume of DMSO to trk1Δtrk2Δ cells. 195 uL of WT + small molecule, 195 uL of trk1Δtrk2Δ + small molecule, and 195 uL of trk1Δtrk2Δ + DMSO were added to a 96 well plate. Next, 5 μL of DMSO or chemical inhibitor was added to each well, with each concentration tested in triplicate for both WT and trk1Δtrk2Δ. The plate was covered and incubated at 30 °C for 24 hours. A BioTek Synergy H1 Hybrid Reader was used to measure the OD_{600}. Utilizing GraphPad PRISM, data were fitted by nonlinear regression, inhibition dose response, variable slope (four parameters) to yield EC_{50} values with SEM. For statistical analysis, EC_{50} values from the two treatment groups were compared by unpaired t-test.

2.7 REFERENCES

1. R. D. Cannon *et al.*, Candida albicans drug resistance another way to cope with stress. *Microbiology* **153**, 3211-3217 (2007).
2. J. Mora-Duarte *et al.*, Comparison of caspofungin and amphotericin B for invasive candidiasis. *New England Journal of Medicine* **347**, 2020-2029 (2002).
3. B. C. Monk, A. Goffeau, Outwitting multidrug resistance to antifungals. *Science* **321**, 367-369 (2008).
4. L. N. Ermishkin, K. M. Kasumov, V. M. Potzeluyev, Single ionic channels induced in lipid bilayers by polyene antibiotics amphotericin B and nystatine. *Nature* **262**, 698-699 (1976).
5. T. E. Andreoli, M. Monahan, The interaction of polyene antibiotics with thin lipid membranes. *The Journal of general physiology* **52**, 300-325 (1968).
6. A. Cass, A. Finkelstein, V. Krespi, The ion permeability induced in thin lipid membranes by the polyene antibiotics nystatin and amphotericin B. *The Journal of general physiology* **56**, 100-124 (1970).
7. A. Finkelstein, R. Holz, Aqueous pores created in thin lipid membranes by the polyene antibiotics nystatin and amphotericin B. *Membranes* **2**, 377-408 (1973).
8. T. E. Andreoli, The structure and function of amphotericin B-cholesterol pores in lipid bilayer membranes. *Ann N Y Acad Sci* **235**, 448-468 (1974).
9. B. de Kruijff, R. A. Demel, Polyene antibiotic-sterol interactions in membranes of Acholeplasma laidlawii cells and lecithin liposomes. 3. Molecular structure of the polyene antibiotic-cholesterol complexes. *Biochim Biophys Acta* **339**, 57-70 (1974).
10. J. Bolard, How do the polyene macrolide antibiotics affect the cellular membrane properties? *Biochimica et Biophysica Acta (BBA)-Reviews on Biomembranes* **864**, 257-304 (1986).
11. A. A. Volmer, A. M. Szpilman, E. M. Carreira, Synthesis and biological evaluation of amphotericin B derivatives. *Nat Prod Rep* **27**, 1329-1349 (2010).
12. D. M. Cereghetti, E. M. Carreira, Amphotericin B: 50 years of chemistry and biochemistry. *Synthesis* **2006**, 0914-0942 (2006).
13. M. Chéron *et al.*, Quantitative structure-activity relationships in amphotericin B derivatives. *Biochem Pharmacol* **37**, 827-836 (1988).
14. M. P. Croatt, E. M. Carreira, Probing the role of the mycosamine C2'-OH on the activity of amphotericin B. *Org Lett* **13**, 1390-1393 (2011).
15. M. Baginski, H. Resat, E. Borowski, Comparative molecular dynamics simulations of amphotericin B-cholesterol/ergosterol membrane channels. *Biochim Biophys Acta* **1567**, 63-78 (2002).
16. M. Murata *et al.*, Ion channel complex of antibiotics as viewed by NMR. *Pure and Applied Chemistry* **81**, 1123-1129 (2009).
17. N. Matsumori, Y. Sawada, M. Murata, Large molecular assembly of amphotericin B formed in ergosterol-containing membrane evidenced by solid-state NMR of intramolecular bridged derivative. *Journal of the American Chemical Society* **128**, 11977-11984 (2006).
18. S. Matsuoka, H. Ikeuchi, Y. Umegawa, N. Matsumori, M. Murata, Membrane interaction of amphotericin B as single-length assembly examined by solid state NMR for uniformly 13C-enriched agent. *Bioorg Med Chem* **14**, 6608-6614 (2006).

19. Y. Umegawa *et al.*, Head-to-tail interaction between amphotericin B and ergosterol occurs in hydrated phospholipid membrane. *Biochemistry* **51**, 83-89 (2012).
20. A. J. Verkleij *et al.*, Freeze-etch electron microscopy of erythrocytes, Acholeplasma laidlawii cells and liposomal membranes after the action of filipin and amphotericin B. *Biochim Biophys Acta* **291**, 577-581 (1973).
21. J. Milhaud, V. Ponsinet, M. Takashi, B. Michels, Interactions of the drug amphotericin B with phospholipid membranes containing or not ergosterol: new insight into the role of ergosterol. *Biochimica et Biophysica Acta (BBA)-Biomembranes* **1558**, 95-108 (2002).
22. R. Mouri, K. Konoki, N. Matsumori, T. Oishi, M. Murata, Complex formation of amphotericin B in sterol-containing membranes as evidenced by surface plasmon resonance. *Biochemistry* **47**, 7807-7815 (2008).
23. B. G. Katzung, S. B. Masters, A. J. Trevor, Basic & clinical pharmacology. (2004).
24. S. Fernandez-Lopez, K. Hui-Sun, E. C. Choi, M. Delgado, Antibacterial agents based on the cyclic D, L-alpha-peptide architecture. *Nature* **412**, 452 (2001).
25. D. S. Palacios, T. M. Anderson, M. D. Burke, A post-PKS oxidation of the amphotericin B skeleton predicted to be critical for channel formation is not required for potent antifungal activity. *Journal of the American Chemical Society* **129**, 13804-13805 (2007).
26. D. S. Palacios, I. Dailey, D. M. Siebert, B. C. Wilcock, M. D. Burke, Synthesis-enabled functional group deletions reveal key underpinnings of amphotericin B ion channel and antifungal activities. *Proc Natl Acad Sci U S A* **108**, 6733-6738 (2011).
27. K. C. Gray *et al.*, Amphotericin primarily kills yeast by simply binding ergosterol. *Proc Natl Acad Sci U S A* **109**, 2234-2239 (2012).
28. H. Jin, J. M. McCaffery, E. Grote, Ergosterol promotes pheromone signaling and plasma membrane fusion in mating yeast. *J Cell Biol* **180**, 813-826 (2008).
29. Y. M. te Welscher, M. R. van Leeuwen, B. de Kruijff, J. Dijksterhuis, E. Breukink, Polyene antibiotic that inhibits membrane transport proteins. *Proc Natl Acad Sci U S A* **109**, 11156-11159 (2012).
30. M. Kato, W. Wickner, Ergosterol is required for the Sec18/ATP-dependent priming step of homotypic vacuole fusion. *EMBO J* **20**, 4035-4040 (2001).
31. A. Heese-Peck *et al.*, Multiple functions of sterols in yeast endocytosis. *Mol Biol Cell* **13**, 2664-2680 (2002).
32. I. Solomon, Relaxation processes in a system of two spins. *Physical Review* **99**, 559 (1955).
33. P. S. Nadaud, J. J. Helmus, N. Höfer, C. P. Jaroniec, Long-range structural restraints in spin-labeled proteins probed by solid-state nuclear magnetic resonance spectroscopy. *J Am Chem Soc* **129**, 7502-7503 (2007).
34. M. B. Sankaram, T. E. Thompson, Cholesterol-induced fluid-phase immiscibility in membranes. *Proc Natl Acad Sci U S A* **88**, 8686-8690 (1991).
35. Y. W. Hsueh *et al.*, Ergosterol in POPC membranes: physical properties and comparison with structurally similar sterols. *Biophys J* **92**, 1606-1615 (2007).
36. K. Watson, E. Bertoli, D. E. Griffiths, Phase transitions in yeast mitochondrial membranes. The effect of temperature on the energies of activation of the respiratory enzymes of Saccharomyces cerevisiae. *Biochem J* **146**, 401-407 (1975).
37. C. S. Ejsing *et al.*, Global analysis of the yeast lipidome by quantitative shotgun mass spectrometry. *Proc Natl Acad Sci U S A* **106**, 2136-2141 (2009).

38. L. Chen *et al.*, Constant-time through-bond 13C correlation spectroscopy for assigning protein resonances with solid-state NMR spectroscopy. *J Am Chem Soc* **128**, 9992-9993 (2006).
39. K. Takegoshi, S. Nakamura, T. Terao, 13C–1H dipolar-assisted rotational resonance in magic-angle spinning NMR. *Chemical physics letters* **344**, 631-637 (2001).
40. M. Hohwy, C. Rienstra, C. Jaroniec, R. Griffin, Fivefold symmetric homonuclear dipolar recoupling in rotating solids: Application to double quantum spectroscopy. *The Journal of chemical physics* **110**, 7983-7992 (1999).
41. D. Huster, X. Yao, M. Hong, Membrane protein topology probed by 1H spin diffusion from lipids using solid-state NMR spectroscopy. *Journal of the American Chemical Society* **124**, 874-883 (2002).
42. A. Lange, S. Luca, M. Baldus, Structural constraints from proton-mediated rare-spin correlation spectroscopy in rotating solids. *J Am Chem Soc* **124**, 9704-9705 (2002).
43. M. Tang, A. J. Waring, M. Hong, Intermolecular packing and alignment in an ordered beta-hairpin antimicrobial peptide aggregate from 2D solid-state NMR. *J Am Chem Soc* **127**, 13919-13927 (2005).
44. M. Hohwy, C. Jaroniec, B. Reif, C. Rienstra, R. Griffin, Local Structure and Relaxation in Solid-State NMR: Accurate Measurement of Amide N− H Bond Lengths and H− N− H Bond Angles. *Journal of the American Chemical Society* **122**, 3218-3219 (2000).
45. A. Haas, A quantitative assay to measure homotypic vacuole fusion in vitro. *Methods in cell science* **17**, 283-294 (1995).
46. P. G. Yancey *et al.*, Cellular cholesterol efflux mediated by cyclodextrins demonstration of kinetic pools and mechanism of efflux. *Journal of Biological Chemistry* **271**, 16026-16034 (1996).
47. B. C. Wilcock, M. M. Endo, B. E. Uno, M. D. Burke, C2'-OH of amphotericin B plays an important role in binding the primary sterol of human cells but not yeast cells. *J Am Chem Soc* **135**, 8488-8491 (2013).
48. C. K. Kang *et al.*, Visualization analysis of the vacuole-targeting fungicidal activity of amphotericin B against the parent strain and an ergosterol-less mutant of Saccharomyces cerevisiae. *Microbiology* **159**, 939-947 (2013).
49. B. M. Vincent, A. K. Lancaster, R. Scherz-Shouval, L. Whitesell, S. Lindquist, Fitness trade-offs restrict the evolution of resistance to amphotericin B. *PLoS Biol* **11**, e1001692 (2013).
50. D. Sanglard, F. Ischer, T. Parkinson, D. Falconer, J. Bille, Candida albicans mutations in the ergosterol biosynthetic pathway and resistance to several antifungal agents. *Antimicrob Agents Chemother* **47**, 2404-2412 (2003).
51. C. A. Hübner, T. J. Jentsch, Ion channel diseases. *Human molecular genetics* **11**, 2435-2445 (2002).
52. G. Rouleau, C. Gaspar, *Ion Channel Diseases*. (Academic Press, 2011), vol. 63.
53. M. El-Etri, J. Cuppoletti, Metalloporphyrin chloride ionophores: induction of increased anion permeability in lung epithelial cells. *Am J Physiol* **270**, L386-392 (1996).
54. N. Busschaert *et al.*, Tripodal transmembrane transporters for bicarbonate. *Chem Commun (Camb)* **46**, 6252-6254 (2010).
55. N. Busschaert *et al.*, Synthetic transporters for sulfate: a new method for the direct detection of lipid bilayer sulfate transport. *Chemical Science* **5**, 1118-1127 (2014).

56. C. Jiang *et al.*, Partial correction of defective Cl(-) secretion in cystic fibrosis epithelial cells by an analog of squalamine. *Am J Physiol Lung Cell Mol Physiol* **281**, L1164-1172 (2001).
57. A. V. Koulov *et al.*, Chloride transport across vesicle and cell membranes by steroid-based receptors. *Angew Chem Int Ed Engl* **42**, 4931-4933 (2003).
58. B. Shen, X. Li, F. Wang, X. Yao, D. Yang, A synthetic chloride channel restores chloride conductance in human cystic fibrosis epithelial cells. *PLoS One* **7**, e34694 (2012).
59. N. Sakai, S. Matile, Synthetic ion channels. *Langmuir* **29**, 9031-9040 (2013).
60. T. M. Fyles, How do amphiphiles form ion-conducting channels in membranes? Lessons from linear oligoesters. *Accounts of chemical research* **46**, 2847-2855 (2013).
61. G. W. Gokel, S. Negin, Synthetic ion channels: from pores to biological applications. *Accounts of chemical research* **46**, 2824-2833 (2013).
62. E. Gouaux, R. Mackinnon, Principles of selective ion transport in channels and pumps. *Science* **310**, 1461-1465 (2005).
63. M. Bolotin-Fukuhara, B. Dumas, C. Gaillardin. (Blackwell Publishing Ltd Oxford, UK, 2010).
64. A. H. Kachroo *et al.*, Systematic humanization of yeast genes reveals conserved functions and genetic modularity. *Science* **348**, 921-925 (2015).
65. M. S. Cyert, C. C. Philpott, Regulation of cation balance in Saccharomyces cerevisiae. *Genetics* **193**, 677-713 (2013).
66. R. F. Gaber, C. A. Styles, G. R. Fink, TRK1 encodes a plasma membrane protein required for high-affinity potassium transport in Saccharomyces cerevisiae. *Molecular and Cellular Biology* **8**, 2848-2859 (1988).
67. C. H. Ko, R. F. Gaber, TRK1 and TRK2 encode structurally related K+ transporters in Saccharomyces cerevisiae. *Molecular and Cellular Biology* **11**, 4266-4273 (1991).
68. D. L. Minor, S. J. Masseling, Y. N. Jan, L. Y. Jan, Transmembrane structure of an inwardly rectifying potassium channel. *Cell* **96**, 879-891 (1999).
69. L. N. Ermishkin, K. M. Kasumov, V. M. Potseluyev, Properties of amphotericin B channels in a lipid bilayer. *Biochim Biophys Acta* **470**, 357-367 (1977).
70. M. G. Lee, P. Nurse, Complementation used to clone a human homologue of the fission yeast cell cycle control gene cdc2. *Nature* **327**, 31-35 (1987).
71. J. Brajtburg, S. Elberg, G. Medoff, G. Kobayashi, Increase in colony-forming units of Candida albicans after treatment with polyene antibiotics. *Antimicrobial agents and chemotherapy* **19**, 199-200 (1981).
72. J. Kaiser, Sipping from a poisoned chalice. *Science* **302**, 376 (2003).
73. M. Borisova, L. Ermishkin, A. Y. Silberstein, Mechanism of blockage of amphotericin B channels in a lipid bilayer. *Biochimica et Biophysica Acta (BBA)-Biomembranes* **553**, 450-459 (1979).
74. H. Sentenac *et al.*, Cloning and expression in yeast of a plant potassium ion transport system. *Science*, 663-665 (1992).
75. T. M. Anderson *et al.*, Amphotericin forms an extramembranous and fungicidal sterol sponge. *Nat Chem Biol* **10**, 400-406 (2014).
76. P. Bhattacharyya, W. Epstein, S. Silver, Valinomycin-induced uptake of potassium in membrane vesicles from Escherichia coli. *Proceedings of the National Academy of Sciences* **68**, 1488-1492 (1971).

77. A. B. Pangborn, M. A. Giardello, R. H. Grubbs, R. K. Rosen, F. J. Timmers, Safe and convenient procedure for solvent purification. *Organometallics* **15**, 1518-1520 (1996).
78. S. Seo *et al.*, Biosynthesis of sitosterol, cycloartenol, and 24-methylenecycloartanol in tissue cultures of higher plants and of ergosterol in yeast from [1, 2-13 C 2]-and [2-13 C 2 H 3]-acetate and [5-13 C 2 H 2] MVA. *Journal of the Chemical Society, Perkin Transactions 1*, 2407-2414 (1988).
79. C. R. Morcombe, K. W. Zilm, Chemical shift referencing in MAS solid state NMR. *J Magn Reson* **162**, 479-486 (2003).
80. C. M. Rienstra *et al.*, Determination of Multiple Torsion-Angle Constraints in U− 13C, 15N-Labeled Peptides: 3D 1H− 15N− 13C− 1H Dipolar Chemical Shift NMR Spectroscopy in Rotating Solids. *Journal of the American Chemical Society* **124**, 11908-11922 (2002).
81. M. Ohi, Y. Li, Y. Cheng, T. Walz, Negative Staining and Image Classification - Powerful Tools in Modern Electron Microscopy. *Biol Proced Online* **6**, 23-34 (2004).
82. J. K. Winkler, K. A. Rennick, F. J. Eller, S. F. Vaughn, Phytosterol and tocopherol components in extracts of corn distiller's dried grain. *Journal of agricultural and food chemistry* **55**, 6482-6486 (2007).
83. Z. Shervani, H. Etori, K. Taga, T. Yoshida, H. Okabayashi, Aggregation of polyene antibiotics as studied by electronic absorption and circular dichroism spectroscopies. *Colloids and Surfaces B: Biointerfaces* **7**, 31-38 (1996).
84. D. Bichet *et al.*, Evolving potassium channels by means of yeast selection reveals structural elements important for selectivity. *Proceedings of the National Academy of Sciences of the United States of America* **101**, 4441-4446 (2004).
85. J. A. Kiehlbauch *et al.*, Use of the National Committee for Clinical Laboratory Standards guidelines for disk diffusion susceptibility testing in New York state laboratories. *Journal of clinical microbiology* **38**, 3341-3348 (2000).
86. J. M. Mulet *et al.*, A novel mechanism of ion homeostasis and salt tolerance in yeast: the Hal4 and Hal5 protein kinases modulate the Trk1-Trk2 potassium transporter. *Molecular and cellular biology* **19**, 3328-3337 (1999).
87. D. Corliss, W. White Jr, Fluorescence of yeast vitally stained with ethidium bromide and propidium iodide. *Journal of Histochemistry & Cytochemistry* **29**, 45-48 (1981).
88. G. Chan, D. Hardej, M. Santoro, C. Lau‐Cam, B. Billack, Evaluation of the antimicrobial activity of ebselen: Role of the yeast plasma membrane H+‐ATPase. *Journal of biochemical and molecular toxicology* **21**, 252-264 (2007).
89. G. Kallifatidis, D. Hoepfner, T. Jaeg, E. A. Guzmán, A. E. Wright, The marine natural product manzamine A targets vacuolar ATPases and inhibits autophagy in pancreatic cancer cells. *Marine drugs* **11**, 3500-3516 (2013).

CHAPTER 3

AMPHOTERICIN B RESTORES AIRWAY SURFACE PHYSIOLOGY IN CYSTIC FIBROSIS HUMAN LUNG EPITHELIA AND ANIMALS

Small molecule ion transporters have been shown to restore physiology in protein-deficient cells and animals, and could potentially address diseases such as cystic fibrosis (CF) caused by a deficiency of protein function even in cases of severely reduced or absent protein production. Loss-of-function mutations in the CFTR anion channel result in reduced apical bicarbonate transport and decreased airway surface liquid (ASL) pH, which impairs respiratory host defenses and leads to chronic lung infections. Because basolateral pumps and channels remain active in the absence of functional CFTR, we hypothesized that an outward-facing bicarbonate gradient would develop across the apical membrane, which could be harnessed by a bicarbonate-permeable small molecule channel. Here we report the small molecule amphotericin B (AmB) facilitates apical bicarbonate transport thereby increasing ASL pH. This effect is sustained for at least 48 hours and restores ASL viscosity and antimicrobial activity in CF patient-derived human lung epithelia across a range of genotypes, including those with little to no production of CFTR. AmB similarly increases ASL pH in $CFTR^{-/-}$ piglets. Dependence of the AmB-mediated rescue on Na^+/K^+ ATPase indicates that this unselective CFTR surrogate is functionally interfaced with the endogenous ion transport network driving transepithelial bicarbonate movement. These results suggest a potential CFTR-independent mechanism for addressing CF.

Contributions to the work presented in this chapter are as follows: Rajeev Chorghade performed ^{13}C-NMR bicarbonate efflux assays, proton, potassium, and chloride efflux assays, ^{14}C bicarbonate transport assays, and ^{36}Cl transport assays. Dr. Bo Ram Kim, Rajeev Chorghade, and I performed $CFTR^{-/-}$ pig experiments. Dr. Viral Shah and I performed ASL antibacterial

activity assays. Dr. Xiao Xiao Tang performed ASL viscosity assays. Philip Karp cultured and maintained primary human lung epithelia. Page N. Daniels performed Ussing chamber experiments specifically for assessing CFTR surface expression. Dr. Anthony S. Grillo synthesized compounds **2**-**4**. Rajeev Chorghade, Page N. Daniels and I cultured and maintained all cell lines and epithelial monolayers. Portions of this chapter were adapted from Muraglia, K.A.; Chorghade, R.S.; Kim, B.K.; Tang, X.X.; Shah, V.S.; Grillo, A.S.; Daniels, P.N.; Cioffi, A.G.; Karp, P.H.; Zhu, L.; Welsh, M.J.; Burke, M.D. "CFTR-independent rescue of cystic fibrosis with a small molecule bicarbonate channel" *Manuscript in preparation.*

3.1 CYSTIC FIBROSIS: A DISEASE CAUSED BY PROTEIN DEFICIENCY

As discussed in previous chapters, many human diseases are caused by a deficiency of protein function, and therefore are refractory to conventional pharmacological strategies. One such disease is cystic fibrosis (CF), a genetic disorder caused by loss-of-function mutations in the CF transmembrane conductance regulator (CFTR) protein ion channel and characterized by abnormal epithelial anion transport, elevated sweat chloride concentrations, pancreatic insufficiency, and chronic lung infection and bronchiectasis (*1, 2*). There are almost 2000 known CFTR mutations, hundreds of which cause disease in CF patients through at least five different mechanisms of functional loss (*1*). About 10% of all CF-causing mutations in the CFTR anion channel are Class I nonsense and splice defects that result in little to no functional CFTR at the apical membrane (*2*). Major clinical advances have been made with genotype-specific small molecule-based therapies, which were detailed in the introduction chapter. However, because these therapeutics require a CFTR protein substrate, this subset of mutations remains inherently unaddressable (*3*). Therefore, this creates an unmet medical need for an alternative small molecule approach that is fundamentally CFTR-independent, and thus could be applied across all

classes of CFTR mutations. We have recently reported that small molecules with the capacity to autonomously transport ions across lipid membranes can restore physiology in protein-deficient cells and animal models by functionally interfacing with the endogenous ion transport system (*4, 5*). We saw CFTR deficiency, particularly in cases where protein production is significantly reduced or absent, as another opportunity to test the mechanistic hypothesis that an independently functioning small molecule mimic of a protein could interface with the existing network of protein ion transporters and thereby restore physiology.

CFTR is an anion channel and is able to transport both chloride and bicarbonate ions. In contrast to dysfunctional chloride transport, recent studies have revealed that maintenance of airway surface liquid (ASL) pH is critical in the prevention of chronic lung infections seen in CF patients (*6, 7*). It has been hypothesized that this requires a balance between proton export through the nongastric H^+/K^+ adenosine triphosphatase proton pump ATP12A and bicarbonate ion secretion through CFTR (*6*). Loss of CFTR therefore leads to a decrease in ASL pH, which in turn increases ASL viscosity and decreases activity of pH-sensitive antimicrobial proteins (*6, 8*). The decrease in ASL pH and its downstream effects largely contribute in the chronic airway infections that cause morbidity and mortality in CF patients (*6, 8*). Consistent with this mechanism, potentiation of the CFTR channel by the clinically approved drug ivacaftor increased ASL pH by 0.20 units and decreased viscosity by about 1.5 units relative to untreated controls in primary sinonasal epithelia from a patient with a G551D mutation, and this seemingly small correction of ASL physiology translates to substantial clinical impact (*9, 10*). Respiratory pathogens such as *Pseudomonas aeruginosa* can also contribute to the observed decrease in ASL pH by secreting protons through monocarboxylate lactate-H^+ co-transporters, a process countered by bicarbonate secretion in normal airways but not in CF (*11*). Notably, administration

of aerosolized bicarbonate or buffers to CF epithelia also increased ASL pH and normalized antimicrobial activity. However, these effects are transient and clinically impractical, with pH returning to baseline values within an hour (*7*).

3.2 THE PROSPECT OF MOLECULAR PROSTHETICS IN CYSTIC FIBROSIS

Importantly, partial restoration of CFTR function has significant clinical impact (*3*). Ivacaftor restores only about 30% of open time probability in G551D CFTR, yet in large-scale clinical trials yielded a substantial increase in forced expiratory volume, increased body weight and quality of life, and decreased incidence of pulmonary exacerbation (*10, 12*). The combination of ivacaftor and correctors such as lumacaftor and tezacaftor targets patients with the most common ΔF508 mutation, and while only about 23% and 47% of wild type short-circuit current are restored by each respective combination, clinical trials have been reported to show promise (*3, 13*). Therefore, if we were able to even partially restore ion channel function with an imperfect small molecule mimic of CFTR, it may have the potential for clinical impact. To test this hypothesis, we looked within the specific framework of the ASL pH-based pathophysiology and built upon concepts established in previous studies of small molecule mimics (*4, 5*). In the lung, a network of pumps and channels on the basolateral membrane of epithelial cells, driven by the sodium gradient created by the Na^+/K^+ ATPase, normally facilitates transepithelial bicarbonate transport (Fig. 3.1A). In the absence of CFTR, bicarbonate ions continue to be brought into cells through the basolateral membrane but apical release is abated, yielding increased intracellular pH (*14*). We reasoned that this would results in a large outward-facing pH gradient across the apical membrane that could move ions through a passive small molecule ion channel (Fig. 3.1B). We thus hypothesized that even an unregulated and non-selective small molecule ion channel capable of permeabilizing the apical membrane to bicarbonate ions could functionally interface

with the endogenous protein network that drives and regulates transepithelial bicarbonate transport to increase ASL pH and restore downstream physiology in CF epithelia (Fig. 3.1C).

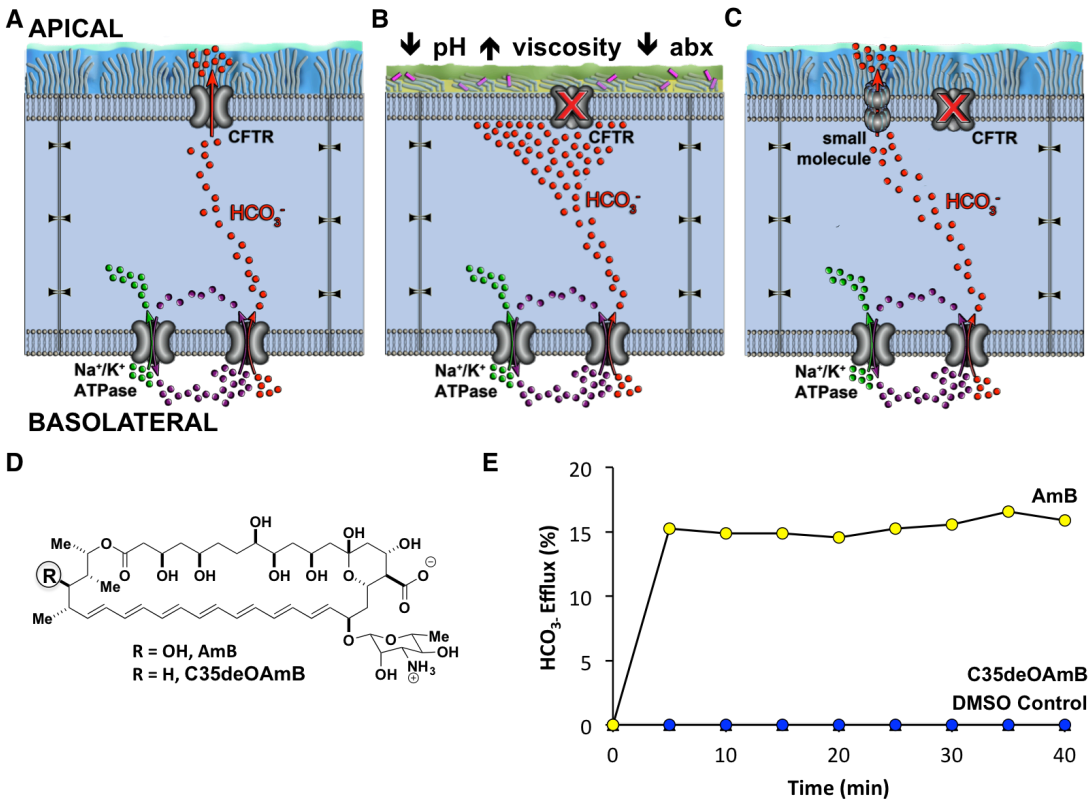

Fig. 3.1. Proposed model and small molecule probe for genotype-agnostic rescue of CF. (**A**) Schematic showing transepithelial bicarbonate transport in a normal airway epithelial cell. Red spheres represent bicarbonate (HCO_3^-) ions. Green and purple spheres represent sodium (Na^+) and potassium (K^+) ions, respectively. (**B**) A large transapical gradient of bicarbonate is hypothesized in CF epithelia lacking the CFTR bicarbonate channel. (**C**) A small molecule-based channel is predicted to leverage this transapical gradient to promote bicarbonate secretion into the ASL and thereby restore physiology in CF lung epithelia. (**D**) Structures of amphotericin B (AmB) and channel-inactivated derivative C35-deoxyamphotericin B (C35deOAmB). (**E**) Efflux studies of $H^{13}CO_3^-$-loaded POPC/10% cholesterol liposomes show that AmB is able to facilitate transmembrane bicarbonate efflux while C35deOAmB or DMSO control do not. In (**E**), a representative graph from at least three independent experiments is shown.

The pair of molecular probes we used to test our hypothesis consists of the clinically approved antifungal natural product amphotericin B (AmB), which is known to form ion channels in lipid membranes, and C35deOAmB, a single-atom-deficient synthetic derivative that we previously showed to lack ion channel activity (*15*) (Fig. 3.1D), thus making this derivative an important negative control. Previous studies on these molecules showed that AmB treatment

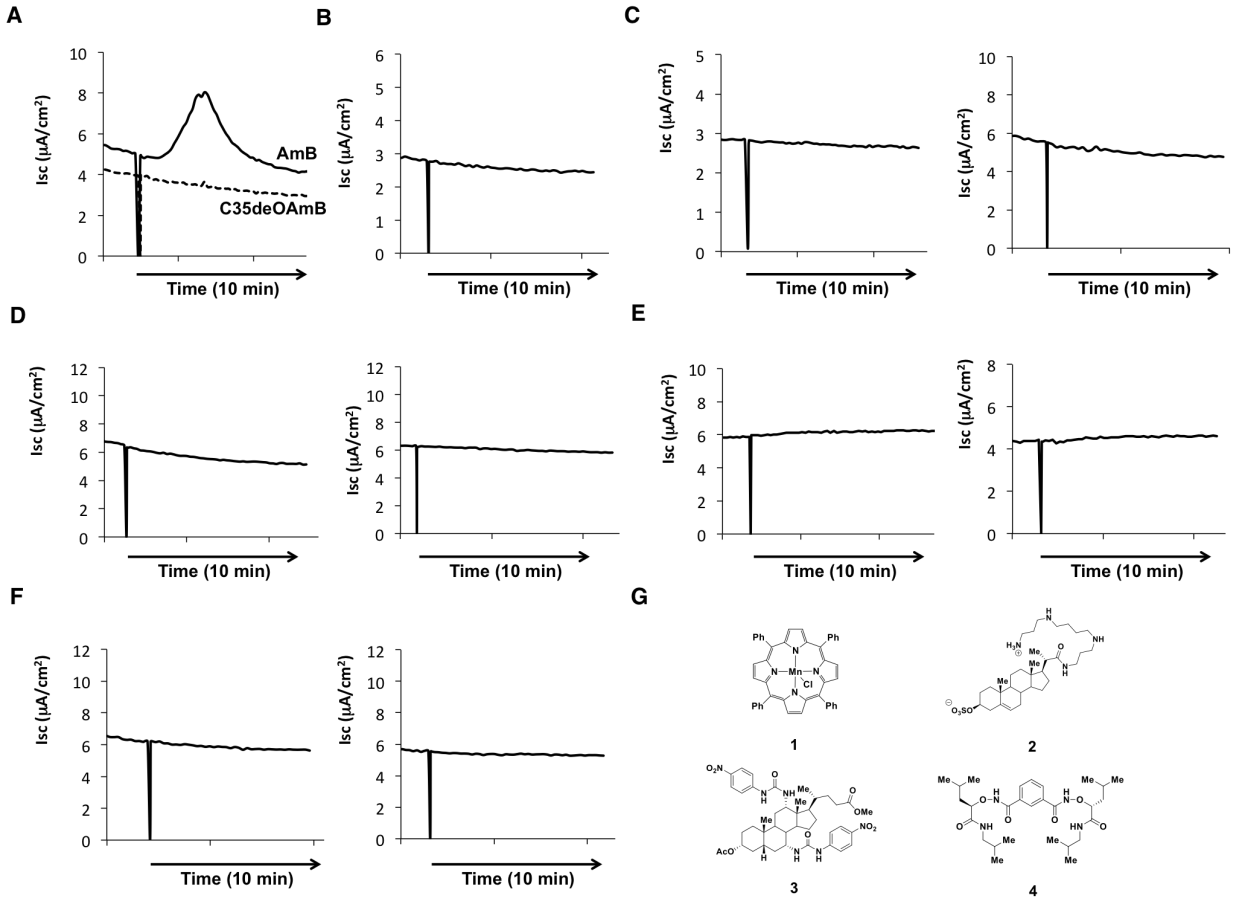

Figure 3.2. Amphotericin B can permeabilize human cultured lung epithelia. Ussing traces of (**A**) 0.5 μM amphotericin B vs. 0.5 μM C35deOAmB, (**B**) 5 μL DMSO vehicle, (**C**) TPPMn(III) 35 μM (left) and 350 μM (right), (**D**) Yang Channel 1 μM (left) and 10 μM (right), (**E**) Cholapod 2e 80 μM (left) and 800 μM (right), (**F**) GL-172 50 μM (left) and 500 μM (right). No permeabilization was observed with small molecules previously described to permeabilize liposomes, non-human tissues, or other human lung tissues, or with the channel-inactivated AmB derivative, C35deOAmB. (**G**) Structures of compounds used in Ussing studies.

restored growth to a strain of *Saccharomyces cerevisiae* missing the Trk 1 and 2 potassium transporters (trk1Δtrk2Δ) and therefore unable to grow under normal potassium conditions (*4*). The channel-inactivated derivative C35deOAmB failed to restore growth in trk1Δtrk2Δ cells at any tested concentration (*4*). With this promising validation of our small molecule ion channel approach in yeast, we prepared to test them in CF human lung epithelia. We first determined if AmB and C35deOAmB had the capacity to transport bicarbonate, the relevant ion in this system, across cholesterol-containing POPC liposomes using an adapted ^{13}C NMR-based assay (*16*). We observed robust and rapid release of ^{13}C-labeled bicarbonate from liposomes treated with AmB,

but not from those treated with C35deOAmB (Fig. 3.1E, Fig. 3.3). We confirmed that AmB also transports potassium (*4, 15, 17*), sodium and chloride ions (Fig. 3.4) and hypothesized that in the absence of CFTR, there would be a gradient-driven selective transport of bicarbonate ions that is independent of the inherent selectivity of the molecule.

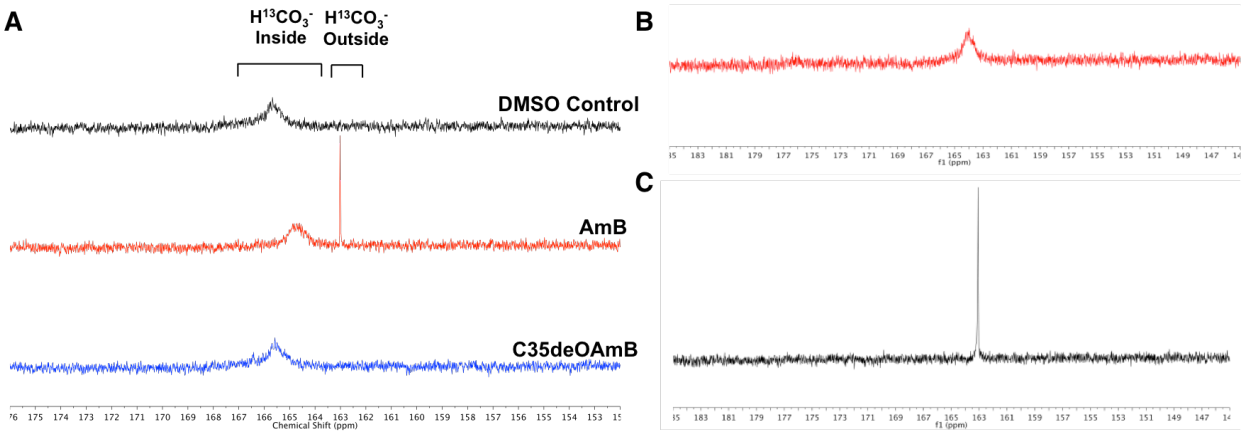

Figure 3.3. Amphotericin B can transport bicarbonate ions across a lipid membrane. (**A**) ^{13}C-NMR spectra of $H^{13}CO_3^-$-loaded POPC/10% cholesterol liposomes showing the appearance of a bicarbonate ^{13}C resonance in the external solution after addition of 1:1000 AmB but not C35deOAmB or DMSO control, demonstrating that AmB is able to facilitate bicarbonate efflux. (**B**) $MnCl_2$ quenching of the external bicarbonate ^{13}C resonance. (**C**) Triton X lysing of liposomes at the conclusion of the experiment. For (**A**) to (**C**), representative spectra from at least three independent experiments are shown.

3.3 AMB INCREASES ASL PH IN CYSTIC FIBROSIS LUNG EPITHELIA

We then grew human airway epithelial cultures derived from a CF patient with the most common ΔF508/ΔF508 mutation (CuFi-1). In an Ussing chamber, we tested if AmB, along with a series of natural products and synthetic compounds previously reported to permeabilize liposomes, cells, and/or nasal epithelia of mice to anions (Fig. 3.2G) (*18-21*), could permeabilize the apical membrane of these epithelia, which have fully differentiated apical and basolateral sides. AmB (Fig. 3.1D) (*22*) was exceptionally effective in causing an increase in short circuit current (Fig. 3.2A), but little or no permeabilization was observed with any of the other compounds tested, including the channel-inactivated derivative C35deOAmB. We then tested the hypothesis that there will be an actionable increase in pH gradient across the apical membrane in

CF vs. normal lung epithelia (Fig. 3.1A,B). Fluorescent pH dyes (*6, 23*) confirmed that relative to differentiated epithelial monolayers derived from a normal individual (NuLi) (*24*), CuFi-1 epithelia have both an increased intracellular pH (Fig. 3.5A) and a decreased ASL pH (Fig. 3.5B), creating an outward-facing pH gradient across the apical membrane.

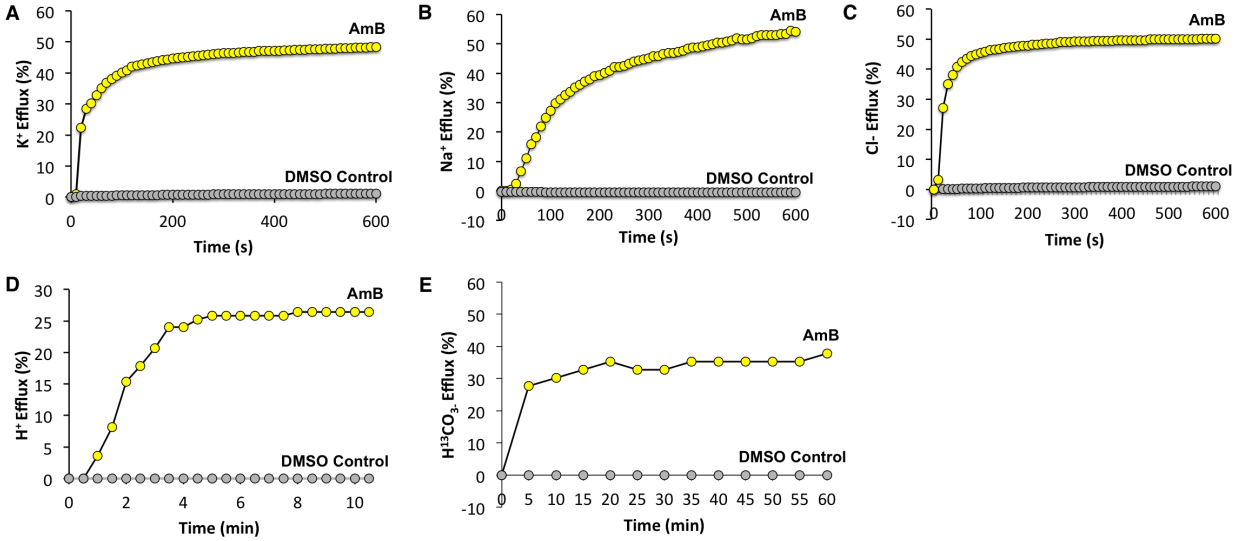

Figure 3.4. Amphotericin B can transport potassium, sodium, and chloride, protons, and bicarbonate across a lipid membrane. (**A**) 1:1000 AmB:lipid can promote potassium efflux from POPC/10% cholesterol liposomes in the presence of a potassium gradient but DMSO control does not, as measured by a potassium-selective electrode. (**B**) 1:1000 AmB:lipid can promote sodium efflux from POPC/10% cholesterol liposomes in the presence of a sodium gradient but DMSO control does not, as measured by a sodium-selective electrode. (**C**) 1:1000 AmB:lipid can promote chloride efflux from POPC/10% cholesterol liposomes in the presence of a chloride gradient but DMSO control does not, as measured by a chloride-selective electrode. (**D**) 1:1000 AmB:lipid can promote proton efflux demonstrated from POPC/10% cholesterol liposomes in the presence of a pH gradient but DMSO control does not, as measured by a pH electrode. (**E**) 1:1000 AmB:lipid can promote bicarbonate efflux demonstrated from POPC/10% cholesterol liposomes in the presence of a bicarbonate gradient but DMSO control does not, as measured by ^{13}C NMR. In (**A**) to (**E**), a representative graph from at least three independent experiments is shown.

Addition of AmB (2 μM) to the apical membrane of CuFi-1 epithelia caused a progressive increase in pH over 2 hours (Fig. 3.5C). Remarkably, this increase in pH was then sustained for at least 48 hours, contrasting sharply with the transient effect on ASL pH caused by aerosolized bicarbonate buffer (*7*). No increase in pH was observed with apical addition of the non-channel-forming variant C35deOAmB, basolateral addition of AmB, or addition of the genotype-specific potentiator ivacaftor, which is specific for a different mutation than that of CuFi-1 epithelia (Fig.

3.5D). Importantly, AmB-treated CuFi-1 epithelia did not respond to chemical activation of CFTR with forskolin/IBMX, providing evidence that the AmB-mediated increase in ASL pH is not due to increasing CFTR activity/trafficking to the surface (Fig. 3.6). AmB addition also did not disrupt membrane integrity (Fig. 3.6). Notably, no increase in ASL pH was observed with apical AmB addition to NuLi epithelia (Fig. 3.7), which provides important evidence for the gradient-driven selective transport of bicarbonate ions independent of inherent AmB selectivity.

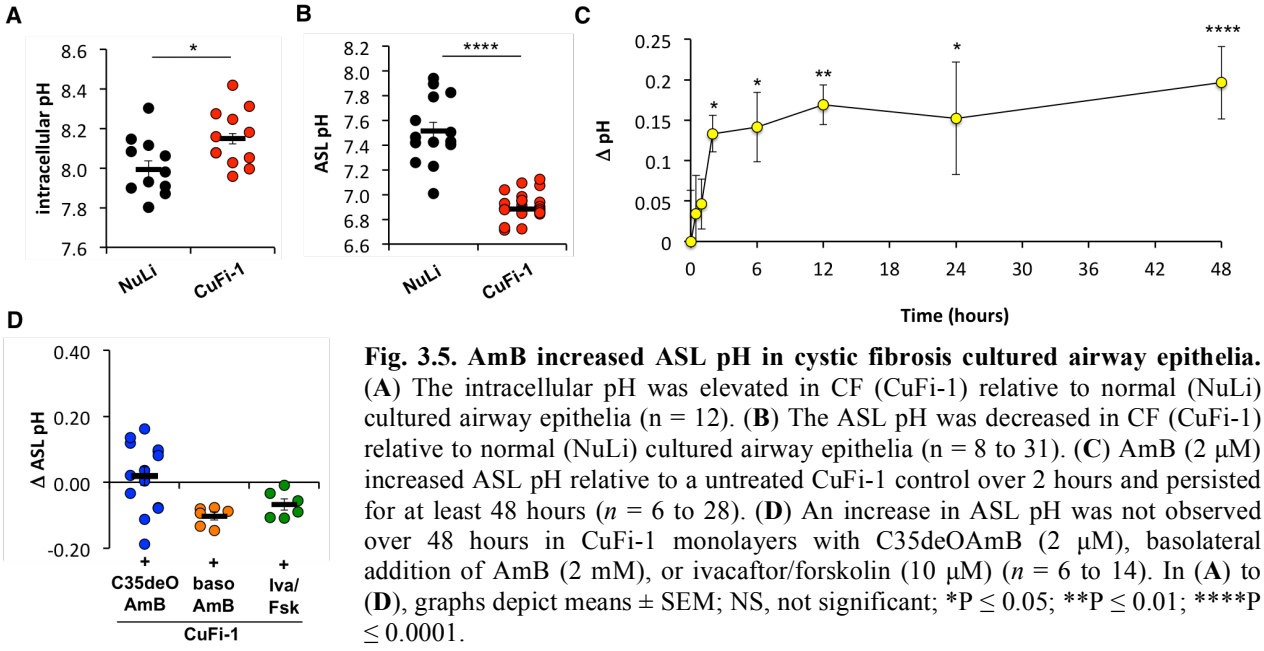

Fig. 3.5. AmB increased ASL pH in cystic fibrosis cultured airway epithelia. (**A**) The intracellular pH was elevated in CF (CuFi-1) relative to normal (NuLi) cultured airway epithelia (n = 12). (**B**) The ASL pH was decreased in CF (CuFi-1) relative to normal (NuLi) cultured airway epithelia (n = 8 to 31). (**C**) AmB (2 μM) increased ASL pH relative to a untreated CuFi-1 control over 2 hours and persisted for at least 48 hours (*n* = 6 to 28). (**D**) An increase in ASL pH was not observed over 48 hours in CuFi-1 monolayers with C35deOAmB (2 μM), basolateral addition of AmB (2 mM), or ivacaftor/forskolin (10 μM) (*n* = 6 to 14). In (**A**) to (**D**), graphs depict means ± SEM; NS, not significant; *P ≤ 0.05; **P ≤ 0.01; ****P ≤ 0.0001.

3.4 MECHANISM OF AMB-MEDIATED ASL PH INCREASE

We next interrogated the mechanism by which AmB mediates this increase in ASL pH. We hypothesized that AmB increases ASL pH by promoting the efflux of bicarbonate ions across the apical membrane. However, AmB is also permeable to protons (Fig. 3.4) and thus proton absorption represents an alternative or complementary mechanistic possibility that would increase ASL pH even in the absence of basolateral bicarbonate ions. To probe this, we performed pH-stat titration experiments in large NuLi and CuFi-1 epithelia (*25*). These epithelia were mounted in an Ussing-type chamber and either bicarbonate (25 mM) or bicarbonate-free

buffer was placed in the basolateral chamber. Subsequent pH changes in the apical chamber solution simulate changes in ASL pH due to transepithelial ion movement. As expected, we observed that NuLi epithelia have a higher rate of ASL pH increase over 20 minutes than CuFi-1 epithelia when bicarbonate buffer is present on the basolateral side. With bicarbonate-free buffer on the basolateral side, we did not observe a difference in rate of pH change between NuLi and CuFi-1 epithelia, consistent with the known bicarbonate-dependence of CFTR (*26*) (Fig. 3.8A). AmB addition caused a dose-dependent rise in the rate of ASL pH increase with basolateral bicarbonate buffer but not with bicarbonate-free buffer (Fig. 3.8A). These findings are consistent with bicarbonate efflux and not proton influx underlying the AmB-mediated increase in ASL pH.

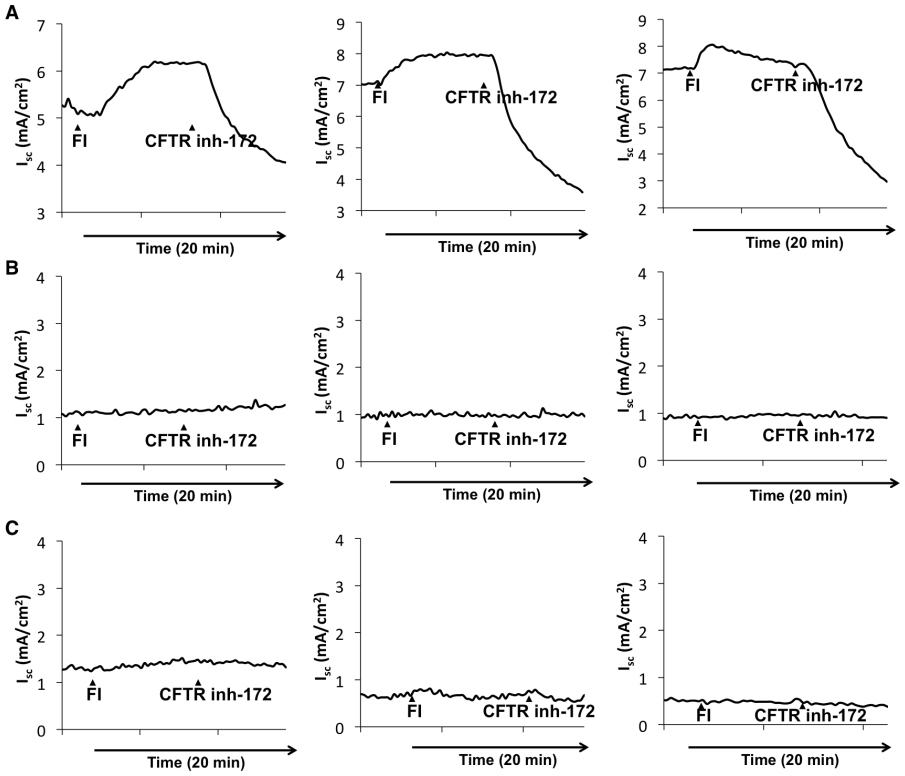

Figure 3.6. Increase in AmB-mediated transepithelial permeabilization is not due to increased CFTR activity. Ussing traces of (**A**) NuLi cultured epithelia, (**B**) CuFi-1 cultured epithelia, and (**C**) CuFi-1 epithelia treated with AmB for 48 hours. NuLi cultured epithelia have increased short-circuit current and therefore permeabilization in response to activation of CFTR with 10 μM forskolin/IBMX (FI), and conversely have decreased current in response to inhibition of CFTR with administration of 1 μM CFTR inh-172. Consistent with the lack of functional CFTR, no response is observed with CuFi-1 epithelia cultures to either activator of inhibitor treatment. A similar lack of response is observed in CuFi-1 epithelia treated with AmB for 48 hours, indicative that CFTR activity is not increased in the presence of AmB. In (**A**) to (**C**), three representative graphs from at least six independent experiments are shown.

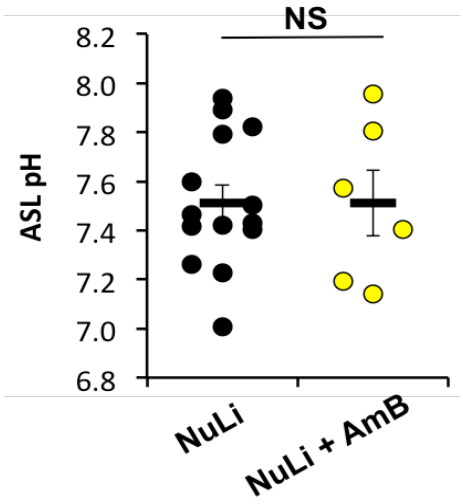

Fig. 3.7. AmB does not increase ASL pH in WT epithelia. AmB (2 uM) does not increase ASL pH in NuLi cultured epithelia (*n* = 6 to 14). Graph depicts means ± SEM; NS, not significant.

To directly probe whether AmB promotes bicarbonate efflux into the ASL, we spiked the basolateral buffer with ^{14}C bicarbonate and quantified the amount of radiolabel that reaches the ASL over 10 minutes. As expected, relative to NuLi, there is a substantial reduction in the rate of ^{14}C bicarbonate efflux in CuFi-1 epithelia (Fig. 3.8B). Apical addition of AmB increased the rate of ^{14}C bicarbonate to a level similar to that observed in NuLi epithelia (Fig. 3.8B). The channel-inactivated derivative C35deOAmB, basolateral addition of AmB, and addition of ivacaftor caused no increase in the rate of ASL ^{14}C bicarbonate efflux (Fig. 3.8B).

We then used the clinically approved potentiator ivacaftor as a genotype-specific (G551D and similar gating mutations) comparator to AmB and clinically relevant positive control. Due to this genotype specificity, we had observed in CuFi-1 epithelia (ΔF508/ΔF508) that ivacaftor treatment showed no increase in ASL pH or bicarbonate efflux (Fig. 3.5D, 3.8B). Consistent with previous reports (*9, 10*), treating CuFi-4 epithelia (G551D/ΔF508) with ivacaftor increased ASL pH by about 0.2 units (Fig. 3.8C). We found that AmB was also able to similarly increase ASL pH in this second cell line, implying that AmB is able to act in a genotype-agnostic manner and potentially be effective across different classes of mutations (Fig. 3.8C).). Importantly, we

also for the first time directly linked apical bicarbonate efflux to ASL pH increase, as CFTR potentiation by ivacaftor in fact leads to increased rate of apical bicarbonate efflux (Fig. 3.8D). This validates our bicarbonate hypothesis with a clinically impactful positive control. The rate of bicarbonate efflux is also increased with AmB treatment, consistent with the observed increase in ASL pH (Fig. 3.8D).

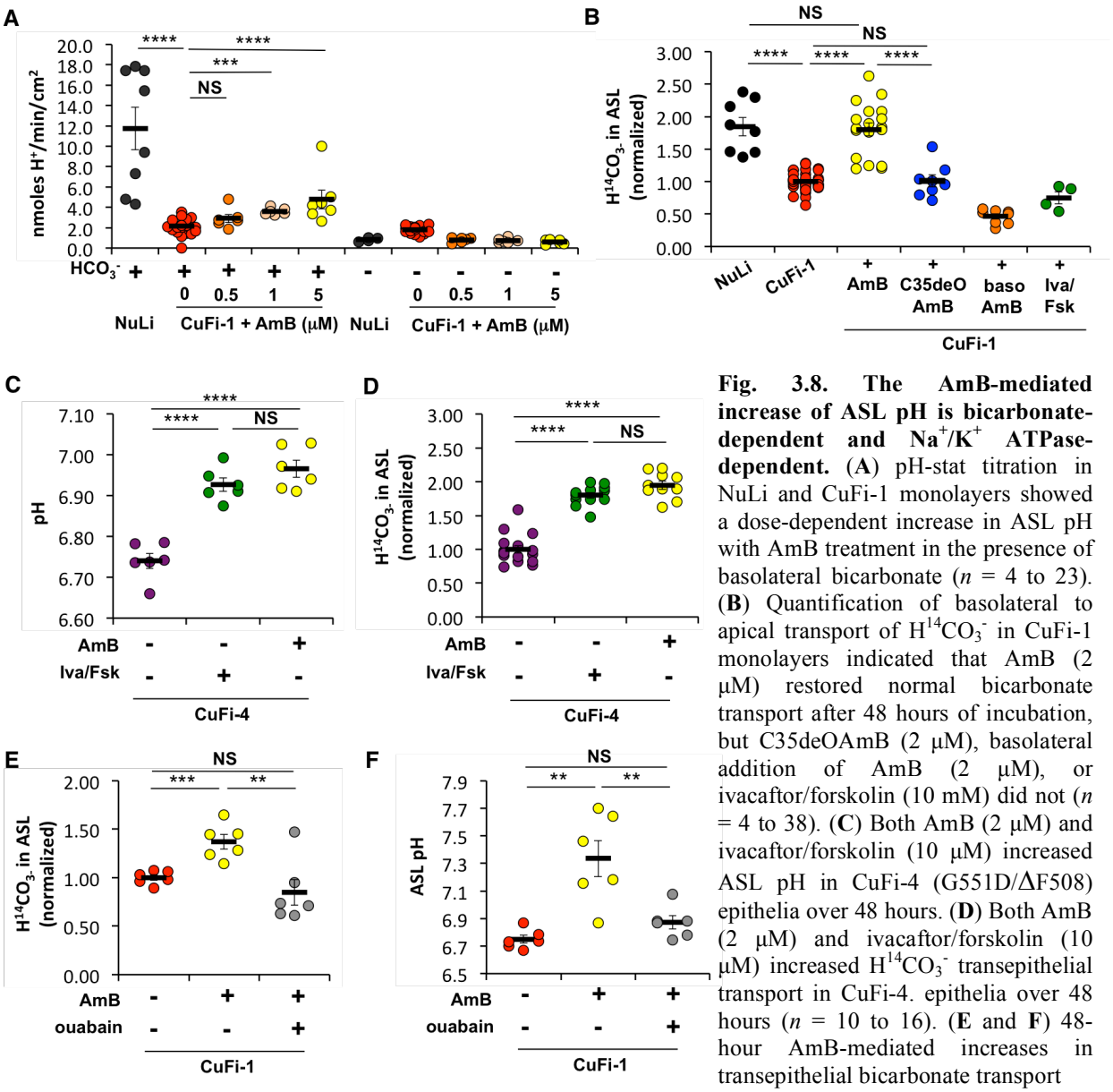

Fig. 3.8. The AmB-mediated increase of ASL pH is bicarbonate-dependent and Na^+/K^+ ATPase-dependent. (**A**) pH-stat titration in NuLi and CuFi-1 monolayers showed a dose-dependent increase in ASL pH with AmB treatment in the presence of basolateral bicarbonate (n = 4 to 23). (**B**) Quantification of basolateral to apical transport of $H^{14}CO_3^-$ in CuFi-1 monolayers indicated that AmB (2 μM) restored normal bicarbonate transport after 48 hours of incubation, but C35deOAmB (2 μM), basolateral addition of AmB (2 μM), or ivacaftor/forskolin (10 mM) did not (n = 4 to 38). (**C**) Both AmB (2 μM) and ivacaftor/forskolin (10 μM) increased ASL pH in CuFi-4 (G551D/ΔF508) epithelia over 48 hours. (**D**) Both AmB (2 μM) and ivacaftor/forskolin (10 μM) increased $H^{14}CO_3^-$ transepithelial transport in CuFi-4. epithelia over 48 hours (n = 10 to 16). (**E** and **F**) 48-hour AmB-mediated increases in transepithelial bicarbonate transport and ASL pH were abrogated by chemical blocking of Na^+/K^+ ATPase with ouabain (10 mM) (n = 6). In (**A**) to (**F**), graphs depict means ± SEM; NS, not significant; **P ≤ 0.01; ***P ≤ 0.001; ****P ≤ 0.0001.

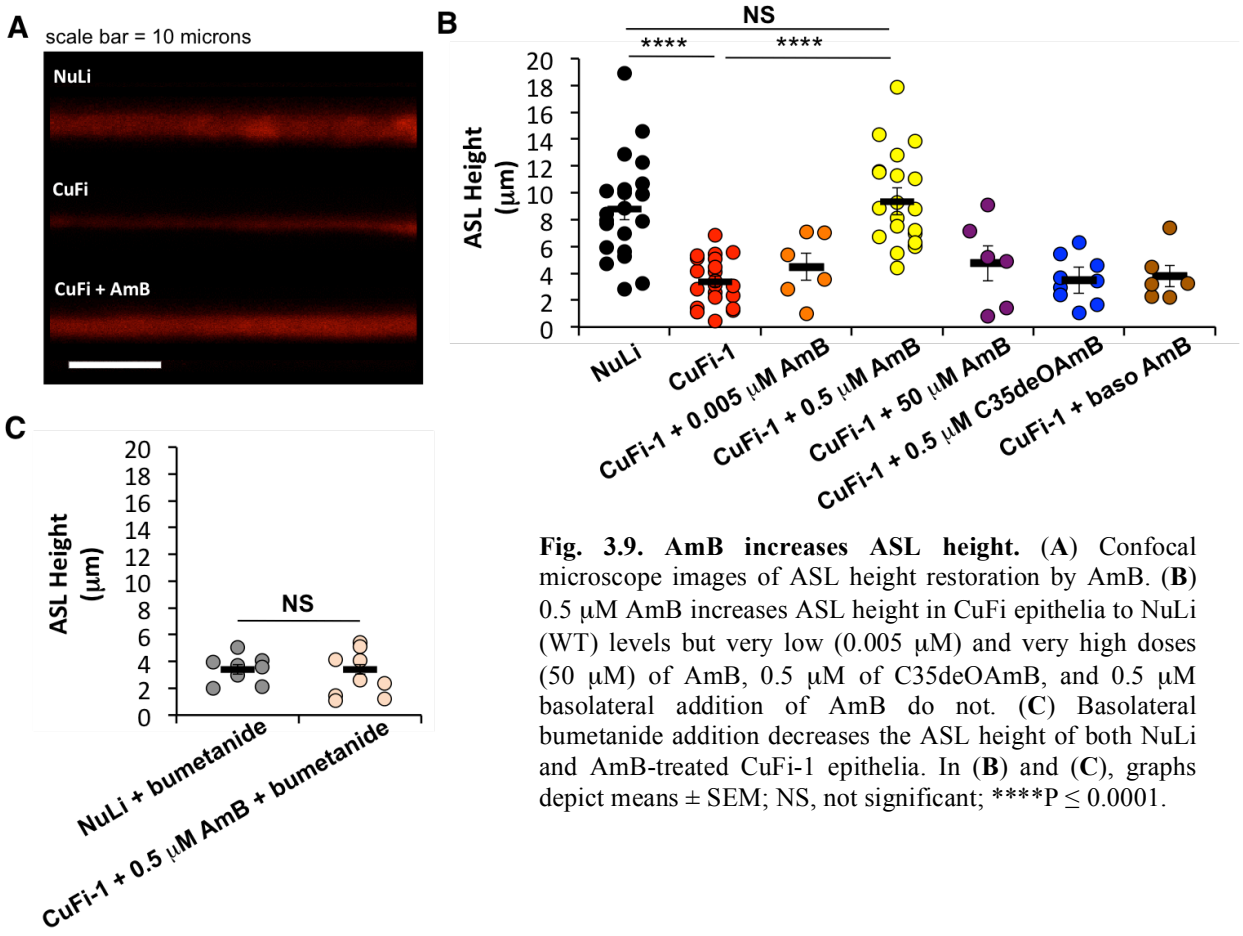

Fig. 3.9. AmB increases ASL height. (**A**) Confocal microscope images of ASL height restoration by AmB. (**B**) 0.5 μM AmB increases ASL height in CuFi epithelia to NuLi (WT) levels but very low (0.005 μM) and very high doses (50 μM) of AmB, 0.5 μM of C35deOAmB, and 0.5 μM basolateral addition of AmB do not. (**C**) Basolateral bumetanide addition decreases the ASL height of both NuLi and AmB-treated CuFi-1 epithelia. In (**B**) and (**C**), graphs depict means ± SEM; NS, not significant; ****P ≤ 0.0001.

As AmB is still permeable to other ions, we sought to determine if salt/fluid homeostasis of the epithelia is maintained. ASL height serves as a phenomenological readout for hyperabsorption of other ions through the AmB channel, particularly sodium. It has been previously reported that in normal lungs, the ASL is approximately the same height as the length of the cilia when it is fully outstretched (7 μm) and allows for normal beating movement unimpeded by the mucus layer above. In CF tissues, this is depleted to 3 μm, as the airway surface may be dehydrated from sodium hyperabsorption and the lack of anion transport through CFTR and subsequently water movement across the epithelia (*27, 28*). Confocal images showed that CuFi-1 epithelia treated with FC-72 vehicle were markedly dehydrated relative to NuLi (Fig. 3.9A,B). Apical AmB treatment (0.5 μM) increases the ASL height in CuFi-1 epithelia to match NuLi (Fig. 3.9A,B). It is interesting to note that very low (0.005 μM) and very high (50 μM)

AmB doses do not have this effect (Fig. 3.9B). Basolateral addition of AmB and treatment with the channel-inactivated derivative C35deOAmB also had no effect (Fig. 3.9B). AmB-mediated restoration of ASL height was blocked via inhibition of NKCC with bumetanide (Fig. 3.9C) supporting collaboration with basolateral chloride transporters. Interestingly, NuLi ASL height is also reduced with chemical inhibition of NKCC with bumetanide (Fig. 3.9C). It is yet unclear if this is due to an importance of transepithelial chloride transport or if basolateral sodium, potassium or chloride entry through NKCC has some downstream impact on apical bicarbonate release, and will require further study.

The rate of bicarbonate import through the basolateral membrane is primarily driven by a sodium gradient created by Na^+/K^+ ATPase. The tissue-specific activity of Na^+/K^+ ATPase is largely regulated by the FXYD family of proteins, and is modulated based on physiological stimuli (*29*). Previous studies showed that FXYD5 is increased three-fold and Na^+/K^+ ATPase activity is increased twofold in CF vs. non-CF epithelial cells (*29, 30*). As discussed in Chapter 2, potassium influx into yeast through Trk transporters is similarly driven by a proton gradient generated by V-ATPase and Pma1, and AmB-mediated growth rescue in Trk-deficient yeast is highly sensitive to V-ATPase or Pma1 chemical inhibition (*4*). We thus hypothesized that the AmB-mediated rescue of ASL pH in CF epithelia would be mitigated by chemically blocking Na^+/K^+ ATPase. Adding ouabain, a specific inhibitor of Na^+/K^+ ATPase, to basolateral buffer of CuFi-1 epithelia in fact abolished the AmB-mediated increase in rate of ^{14}C bicarbonate efflux and increase in ASL pH (Fig. 3.8D,E). This is preliminary evidence for a functional interface of AmB to the endogenous protein network.

3.5 AMB RESTORES ASL PHYSIOLOGY IN PRIMARY HUMAN LUNG EPITHELIA AND A CFTR$^{-/-}$ PIG MODEL

To determine if the capacity for AmB to restore ASL pH in a genotype-agnostic manner translates to primary human airway epithelia, we obtained samples from 9 CF patient donors representing a range of different CFTR mutations (Fig. 3.10A, Table 3.1). These include multiple patients with the most common ΔF508/ΔF508 genotype, a double null genotype (R553X/E60X) and a rare splice site allele (1717-1G->A) that both result in little to no CFTR protein produced. Another patient had a V520F allele, which is in the same functional category as G551D but is refractory to treatment with ivacaftor (*31*). Patients were also included with uncategorized alleles (D259G, ΔF508/c.2052dupA) (*32*). As these mutation phenotypes are unknown, rational development of specific treatment is challenging.

Patient #	Genotype	Trial 1 Δ pH	Trial 2 Δ pH	Trial 3 Δ pH
1	ΔF508/ΔF508	0.27	0.36	-
2	ΔF508/ΔF508	0.13	0.11	0.43
3	ΔF508/ΔF508	0.02	0.18	-
4	ΔF508/ΔF508	0.31	-	-
5	ΔF508/ΔF508	0.17	-	-
6	R553X/E60X	0.12	0.31	0.56
7	ΔF508/1717-1G→A	0.04	0.06	0.06
8	ΔF508/c.2052dupA	-0.16	0.14	-
9	D239G/V520F	0.68	0.15	-

Table 3.1. Genotypes and Δ pH measurements of patient donors in ASL pH assay.

On average, AmB increased ASL pH by 0.2 pH units in the genotypes tested (Fig. 3.10A), consistent with our results in CuFi-1 and CuFi-4 epithelia (Fig. 3.5C, 3.8C). This AmB-mediated increase in the ASL pH is also sustained for at least 48 hours (Fig. 3.8B). One mutation with an

unknown allele (ΔF508/c.2052dupA) gave two opposing results during assay replication that resulted in net no change in ASL pH. C35deOAmB and basolateral addition of AmB did not increase ASL pH (Fig. 3.11A). As seen in the cell lines, AmB treatment had no effect on the pH of non-CF primary cultured epithelia, further providing evidence for dependence upon the pH gradient associated with the absence of CFTR (Fig. 3.11B).

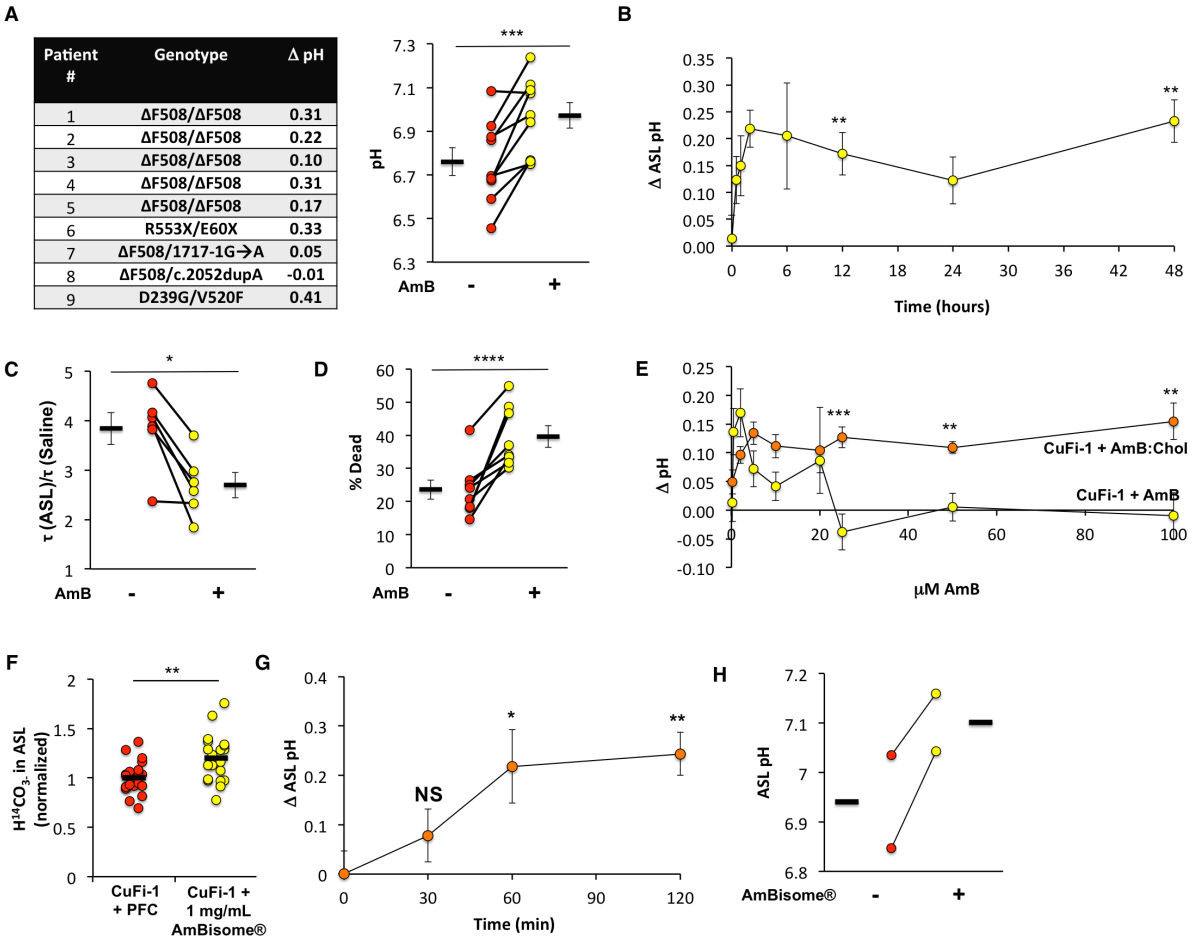

Fig. 3.10. AmB restored ASL physiology in primary cultured human lung epithelia derived from CF patients with a wide range of CFTR genotypes and in CFTR$^{-/-}$ piglets. (**A**) Genotypes and mutation classes of patient donors. An increase in ASL pH was observed upon AmB (2 μM) treatment across a wide range of CFTR genotypes. On average, AmB (2 μM) increased ASL pH by about 0.2 pH units over 48 hours (n = 9). (**B**) On average, AmB (2 μM) increased ASL pH relative to an untreated CF control over 2 hours and this effect persists for at least 48 hours (n = 3 to 9). (**C**) AmB (2 μM) decreased ASL viscosity of genetically diverse CF epithelia over 48 hours (n = 6). (**D**) AmB (2 μM) increased ASL antibacterial activity of genetically diverse CF epithelia over 48 hours (n = 8). (**E**) AmB increased ASL pH in CuFi-1 monolayers at low but not at high concentrations. Complexation of AmB with cholesterol extends the window of efficacy to at least 100 uM (n = 9 to 31). (**F**) AmBisome® (1 mg/mL) increased bicarbonate transport in CuFi-1 cultured epithelia over 2 hours. (**G**) AmBisome® (100 ug/mL) increased ASL pH in CuFi-1 cultured epithelia over 2 hours. (**H**) A high dose of AmBisome ® (1 mg/mL) increased ASL pH in CFTR$^{-/-}$ piglets sustained for at least 1 hour (n = 2). In (**A**) to (**G**), graphs depict means ± SEM; NS, not significant; *P ≤ 0.05; **P ≤ 0.01; ***P ≤ 0.001; ****P ≤ 0.0001.

We further tested in genetically diverse primary cultured human CF epithelia (Table 3.2) whether a single treatment with AmB leads to decreased viscosity in the ASL at the 48 h time point. AmB decreased ASL viscosity across a wide range of patient genotypes (Fig. 3.10C). The average amplitude of viscosity reduction (~1.5 units) matched that previously observed with ivacaftor-treated primary sinonasal epithelia from a CF patient with a G551D allele (*9*). We also determined the capacity for the ASL of AmB-treated primary CF epithelia to kill bacteria at the same 48-hour timepoint. We did this by briefly touching the ASL with a gold grid coated with *Staphylococcus aureus* and then determining the percentage of bacteria killed (*6*). As controls, bacteria-coated grids were also placed in saline or AmB in FC-72 laid over saline to simulate the administration method. Treatment with AmB increased antibacterial activity for a range of patient genotypes (Table 3.3). On average, AmB treatment nearly doubled ASL bacterial killing (Fig. 3.10D), whereas C35deOAmB had no effect (Fig. 3.12A). Importantly, AmB alone does not have antibacterial activity against *S. aureus* as compared to saline (Fig. 3.12B).

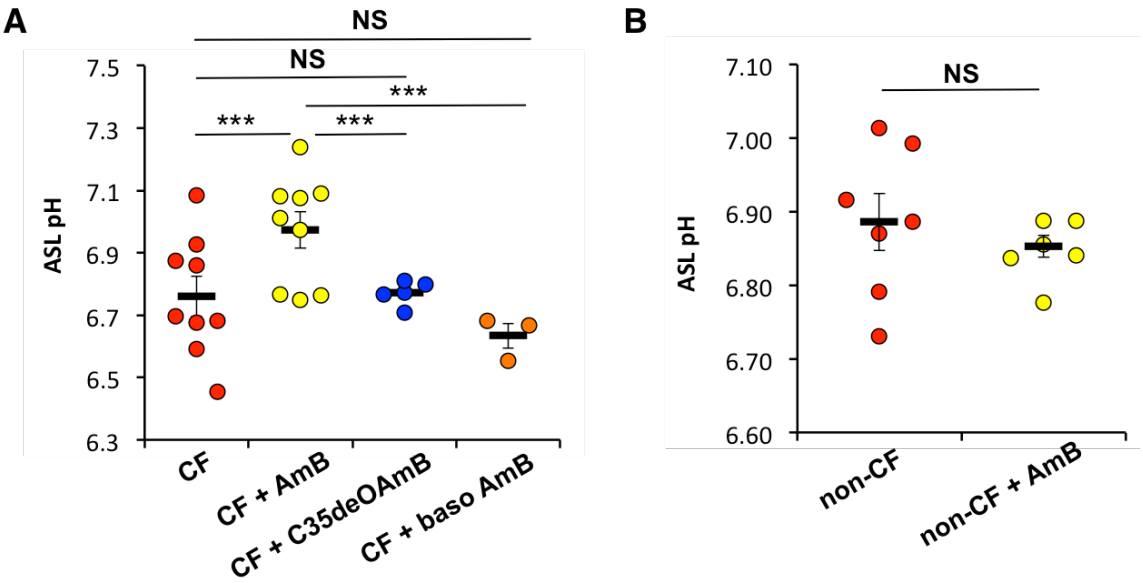

Fig. 3.11. AmB restores ASL pH in primary human lung epithelia isolated from CF patients. (**A**) On average, AmB (2 μM) increased ASL pH while C35deOAmB (2 μM) and basolateral addition of AmB (2 μM) did not (n = 3 to 9). (**B**) AmB (2 μM) does not increase ASL pH in non-CF cultured epithelia (n = 7). In (**A**) and (**B**), graphs depict means ± SEM; NS, not significant; ***P ≤ 0.001.

Genotypes for ASL viscosity assay
ΔF508/ΔF508
ΔF508/ΔF508
ΔF508/ΔF508
ΔF508/c.2052dupA
ΔF508/Y563NPolyT
ΔF508/1717-1G→A

Table 3.2. Genotypes of patient donors in ASL viscosity assay.

Genotypes for ASL antibacterial activity assay
ΔF508/ΔF508
ΔF508/ΔF508
ΔF508/ΔF508
ΔF508/ΔF508
ΔF508/ΔF508
ΔF508/ΔF508
D239G/V520F
ΔF508/1717-1G→A

Table 3.3. Genotypes of patient donors in ASL antibacterial activity assay.

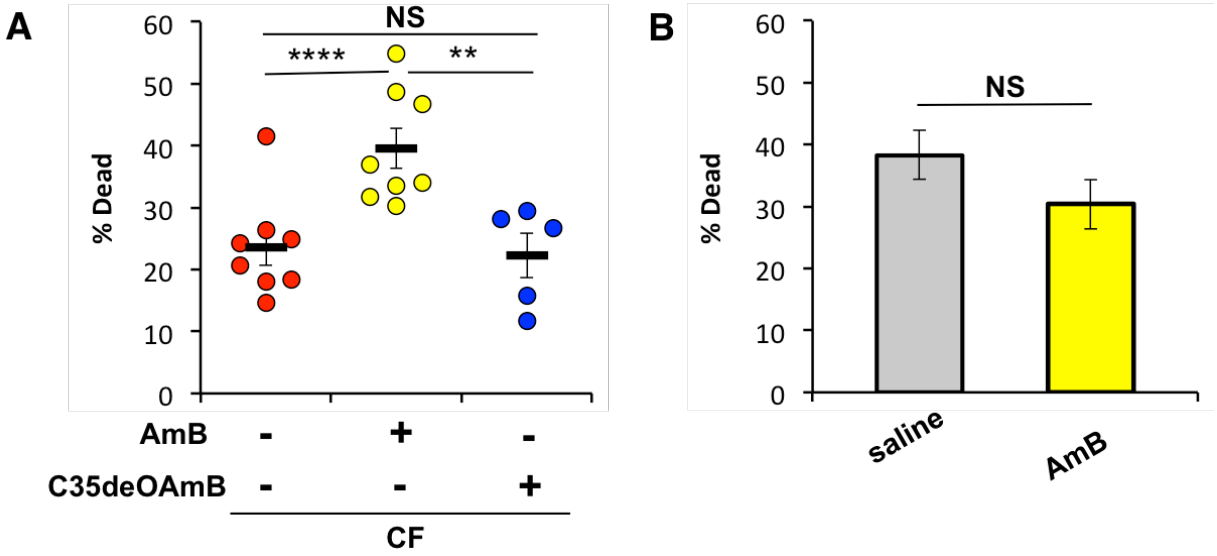

Fig. 3.12. AmB restores ASL antibacterial activity in primary human lung epithelia isolated from CF patients. (**A**) AmB (2 μM) increased ASL antibacterial activity while C35deOAmB (2 μM) did not (n = 5 to 8). (**B**) AmB (2 μM) alone does not have antibacterial activity against *S. aureus* as compared to saline (n = 36). In (**A**) and (**B**), graphs depict means ± SEM; NS, not significant; **P ≤ 0.01; ****P ≤ 0.0001.

The porcine model of CF (*7*) has been invaluable to translational research of the disease due to its similarity to human respiratory anatomy, physiology, and CF pathophysiology. However, based on our understanding of AmB, we foresaw a number of challenges to *in vivo* testing and later clinical application, which include a narrow dosage range, drug delivery to the lung, and variable dosing due to distribution limitations. The AmB-mediated increase in ASL pH in CuFi-1 epithelia reaches a maximum at 2 μM and then decreases at higher concentrations (Fig. 4E).

Suspecting that this loss of activity at higher concentrations may be due to toxic cholesterol binding activity (*15, 33*) and to potentially address the issue of a narrow dosage range, we looked to previous work on the sterol sponge model of AmB (*33*). Saturating the AmB sterol sponge with endogenous sterol has been shown to prevent sterol extraction and therefore toxicity, while still maintaining channel-forming activity (*4, 33*). As shown in Chapter 2, by pre-complexing AmB to the native sterol in yeast, ergosterol, the range of doses for which trk1Δtrk2Δ growth rescue is observed can be extended by more than an order of magnitude (*4, 33*). A similar pre-complexation of AmB to the endogenous human sterol, cholesterol, could potentially allow us to test our hypothesis in CF epithelia at a greater dosage range.

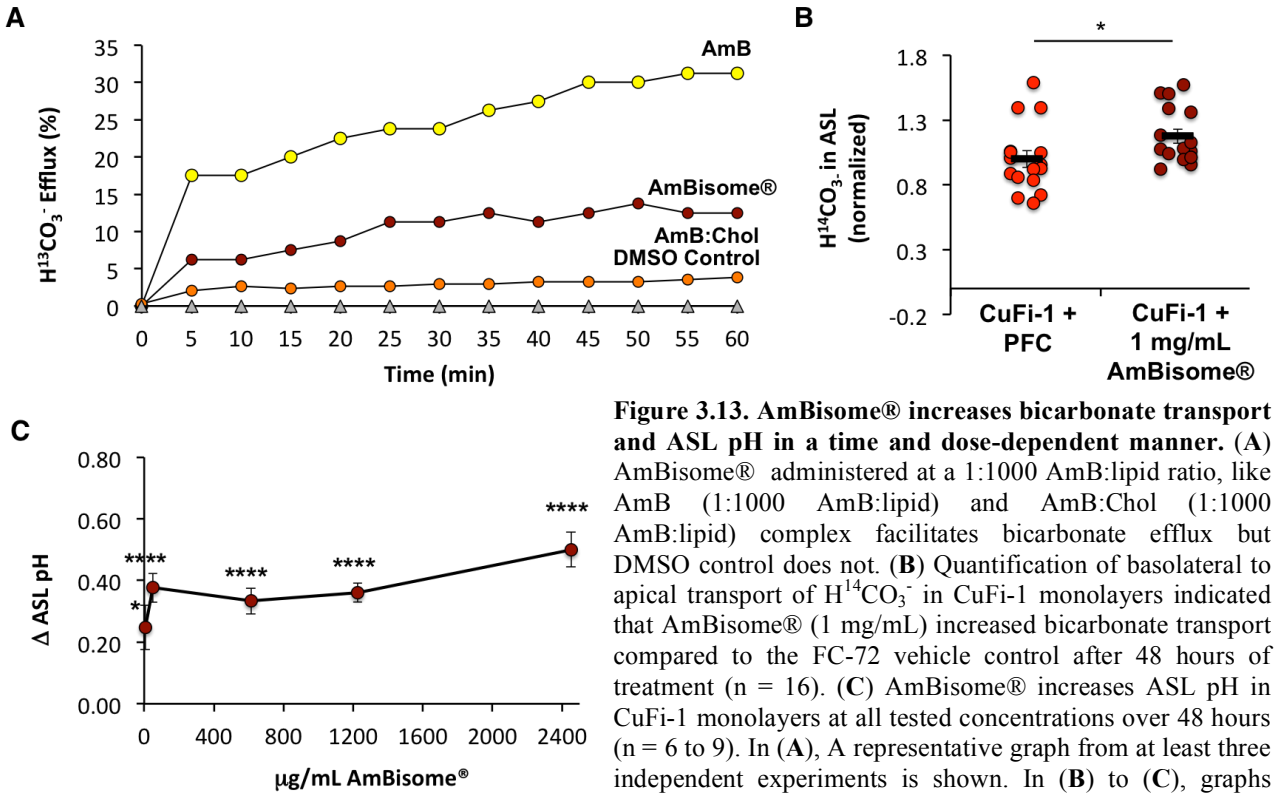

Figure 3.13. AmBisome® increases bicarbonate transport and ASL pH in a time and dose-dependent manner. (**A**) AmBisome® administered at a 1:1000 AmB:lipid ratio, like AmB (1:1000 AmB:lipid) and AmB:Chol (1:1000 AmB:lipid) complex facilitates bicarbonate efflux but DMSO control does not. (**B**) Quantification of basolateral to apical transport of $H^{14}CO_3^-$ in CuFi-1 monolayers indicated that AmBisome® (1 mg/mL) increased bicarbonate transport compared to the FC-72 vehicle control after 48 hours of treatment (n = 16). (**C**) AmBisome® increases ASL pH in CuFi-1 monolayers at all tested concentrations over 48 hours (n = 6 to 9). In (**A**), A representative graph from at least three independent experiments is shown. In (**B**) to (**C**), graphs depict means ± SEM; NS, not significant; *P ≤ 0.05; ****P ≤ 0.0001 relative to vehicle control.

When we pre-formed an AmB:cholesterol complex and repeated this concentration dependence experiment, a similar increase in ASL pH was observed and then sustained even up to very high concentrations of AmB (100 µM) (Fig. 3.10G). The same pattern was previously

observed upon progressively increasing CFTR protein expression, suggesting some kind of homeostatic control over an optimum ASL pH value inherent in the cellular system (*26*). With these sterol complexation results in hand, we decided to test AmBisome®, an FDA-approved formulation of AmB that contains a 2.5:1 cholesterol to AmB ratio. We hypothesized that such a formulation of AmB may recapitulate our finding of an extended dosage window with the AmB:Chol complex (Fig. 3.10G). It is notable that AmBisome® has been safely delivered to the lungs in aerosolized form (*34*), and variable dosing may not be an issue with the extended range of efficacy observed in the presence of cholesterol.

Like AmB alone, AmBisome® is able to transport bicarbonate ions in a liposomal system (Fig. 3.13A) and increased the rate of ^{14}C bicarbonate efflux across the apical membrane of CuFi-1 cultured epithelia over 2 hour and 48 hour time periods (Fig. 3.10F, 3.13B). Consistent with the bicarbonate efflux data, apical AmBisome® treatment increases ASL pH over 2 hours and is sustained for at least 48 hours (Fig. 3.10G). Increase of ASL pH is observed up to at least 2450 mg/mL AmBisome®, equivalent to 100 μM AmB (Fig. 3.13C). This provided a means for testing AmB channel function in the porcine model that may extend the small dosage window of AmB alone.

We then tested AmBisome® in $CFTR^{-/-}$ piglets. We observed in two $CFTR^{-/-}$ piglets from different litters that, compared to baseline values, 1 mg/mL AmBisome® administered to the surface of a 1 cm^2 tracheal window significantly increased ASL pH (Fig. 3.10H). This effect was sustained for at least 60 minutes (Fig. 3.10H).

3.6 CONCLUSIONS AND PROSPECTUS

Thus, imperfect CFTR mimicry with a bicarbonate-permeable small molecule ion channel is sufficient for restoring important aspects of ASL physiology even in cultured epithelia that

produce little to no CFTR as well as $CFTR^{-/-}$ piglets. This approach is CFTR-independent and therefore genotype-agnostic. Small molecule ion channels can functionally interface with the protein-based bicarbonate transport pathway inherent in lung epithelia. The specific intersection of AmB channels with Na^+/K^+ ATPase adds to a growing list of examples where a small molecule surrogate for a missing protein can interact with other ion transport mechanisms in eukaryotic cells (*5*). Our results further reveal that alternative activities of CFTR that are not replicated by AmB, including regulation of other ion transporters (*35*), are not required for maintaining ASL pH, viscosity, and antibacterial properties. Collectively, these findings demonstrate a mechanism for CFTR-independent rescue of CF using small molecules that promote apical membrane bicarbonate permeabilization and substantially brighten the prospect of using small molecules as surrogates for missing protein ion channels in the clinic. Strategic derivatization of AmB has been shown to modify conductance and selectivity of the corresponding ion channels, suggesting a pathway for optimization of this phenomenon should further evaluation of the natural product reveal challenging limitations (*17*). If shown in future studies to be sustainable as an ongoing treatment in human patients, AmB and its derivatives could be powerful tools in the treatment of yet-incurable channelopathies like cystic fibrosis.

3.7 METHODS

Cell lines and growth conditions. NuLi and CuFi-1 cells (*24*) (a gift from the Welsh Laboratory, University of Iowa) were first grown from cryostock on Thermo Scientific BioLite Cell Culture Treated 75 cm^2 flasks, seeded at 1.5 x 10^4 cells/cm^2 and 1 x 10^3 cells/cm^2 respectively. These flasks were previously coated with 3 mL of 60 µg/ml human placental collagen type VI (Sigma-Aldrich) for a minimum of 18 hours at room temperature, rinsed twice with 1X PBS, and then dried prior to seeding. The cells were cultured with 12 mL of the

Bronchial Epithelial Cell Growth Medium (BEGM) BulletKit (Lonza CC-3170), which includes the basal media and eight SingleQuots of supplements. The gentamycin-amphotericin B aliquot was discarded and the media was instead supplemented with 50 μg/ml penicillin-streptomycin (Corning Cellgro), 50 μg/ml gentamycin (Sigma-Aldrich G1397), and 2 μg/ml fluconazole (Sigma-Aldrich).

Cells were grown to a 90% confluence at 37^{o}C and 5% CO_2 with media changed every 2 days, and then trypsinized with 4 mL of standard 0.25% trypsin with 1 mM EDTA (Gibco 25200-056). Trypsin was inactivated with 10 mL of HEPES Buffered Saline Solution (Lonza CC-5024) with added 1% bovine calf serum. Cells were spun down in an Eppendorf Centrifuge 5430 R at 1500 rpm for 5 minutes and resuspended in BEGM media for passaging.

For culturing onto membrane supports for differentiation, cells were resuspended after centrifugation in Ultroser G media. This is composed of a 1:1 ratio of DMEM:Ham's F-12 supplemented with 2% V/V Ultroser G (Crescent Chemical). The membrane supports used were Millicell 0.4 μm PCF inserts (0.6 cm^2) (Millipore PIHP01250) for Ussing chamber studies of candidate ionophores, Falcon® Permeable Support for 6 Well Plate with 0.4 μm Transparent PET Membranes (4.67 cm^2) (Fisher 08-771) in 6-well companion plates (Fisher 08-771-24) for pH-stat studies, and the Corning Costar 0.4 μm 24-well plate Transwell Clear Polyester Membrane inserts (0.33 cm^2) (Corning 3470) for all other studies. These membranes were coated with collagen in the same manner as the flasks detailed above. The Millicell inserts were seeded with 200,000 cells each, the Falcon inserts were seeded with 500,000 cells each, and the Transwell inserts were seeded with 115,000 cells each. These membranes were allowed to mature at an air-liquid interface for a minimum of 14 days to reach full differentiation, with the Ultroser G media changed every other day. At full maturation, media was changed every 7 days.

Primary cultures of airway epithelia. Airway epithelial cells were obtained from human trachea and bronchi of CF and non-CF specimens obtained from the Iowa Donor Network, either as post-mortem specimens or from tissue deemed not fit for transplant. Studies were approved by the University of Iowa Institutional Review Board. Airway epithelial cells were obtained from the trachea and bronchi of pigs and from trachea of mice after euthanasia. After pronase enzymatic digestion, cells were seeded onto collagen-coated semi-permeable membranes (0.33 – 1.12 cm^2, Corning 3470 polyester, 3460 polyester, 3413 polycarbonate) and grown at an air-liquid interface using previously described methods (*36*). Airway epithelial cell cultures were analyzed after they had differentiated and at least 14 days post-seeding.

Statistics. All data depicts the means ± SEM with a minimum of 3 biological replicates. Statistical analysis represents P values obtained from student t-test. NS, not significant. * $P < 0.05$, ** $P \leq 0.01$, *** $P \leq 0.001$, **** $P \leq 0.0001$ unless otherwise noted.

Ussing Chamber studies of NuLi and CuFi monolayers. For evaluation of candidate ionophores, differentiated cultures of CuFi-1 epithelia grown on Millicell® 0.4 μm PCF inserts were mounted in a dual-channel Ussing chamber (Warner U2500) using the culture cup insert for Millicell adapter, 12 mm (Warner U9924M-12). Stock solutions of 100 mM amiloride and 4,4'-diisothiocyano-2,2'-stilbenedisulfonic acid (DIDS) were prepared in DMSO. Stocks of the experimental solutions of HPLC-purified AmB, C35deOAmB, **2**, **3**, and **4** were prepared in DMSO 1000 times more concentrated than the desired final concentration in buffer. **1** was purchased from Sigma-Aldrich (*15, 16, 18-20*). All recordings were acquired using Acquire & Analyze revision II (Physiologic Instruments).

Electrodes were prepared with 3.5% agar and 3 M KCl. 5 mL of 37°C high chloride buffer (135 mM NaCl, 5 mM HEPES, 2.4 mM K_2HPO_4, 0.6 mM KH_2PO_4, 1.2 mM $CaCl_2$, 1.2 mM

$MgCl_2$, 5 mM dextrose, pH 7.4 with 10 N NaOH) was placed on both sides of the chamber, kept warm by circulating heater (Lauda E 100) and gassed with compressed air. Epithelial sodium channel (ENaC) and calcium-activated chloride channel (CaCC) were inhibited by apical addition of 1 μM amiloride and 1 μM DIDS (4,4'-disothiocyanostilbene-2,2'-disulfonic acid), respectively, to achieve a baseline for small molecule-mediated permeabilization. To establish a basolateral (135 mM) to apical (4.9 mM) chloride gradient, the buffer on the apical side of the membrane was replaced by 5 mL of low chloride buffer (135 mM sodium gluconate, 5 mM HEPES, 2.4 mM K_2HPO_4, 0.6 mM KH_2PO_4, 1.2 mM $CaCl_2$, 1.2 mM $MgCl_2$, 5 mM dextrose, pH 7.4 with 10 N NaOH). When baseline was stabilized, 5 μL of the small molecule for testing was added to the apical buffer and was given a minimum of 10 minutes to observe permeabilization (*24*).

To assess the presence of membrane-expressed CFTR, differentiated cultures of NuLi and CuFi-1 epithelia grown on Corning Costar 0.4 μm 24-well plate Transwell Clear Polyester Membrane inserts were used. NuLi and CuFi-1 epithelia were treated with 20 μL of perfluorocarbon (FC-72, Sigma) vehicle or 2 μM amphotericin B (AmB) sonicated into a suspension in FC-72. After 48 hours of incubation, the epithelia were mounted in a dual-channel Ussing chamber (Warner U2500) using the culture cup insert for Transwell adapter, 6.5 mm (Warner U9924T-06) and bathed on both the apical and basolateral sides with a bicarbonate solution (120 mM NaCl, 25 mM $NaHCO_3$, 5 mM KCl, 2 mM $CaCl_2$, 1.2 mM $MgCl_2$, 13.75 mM NaH_2PO_4, pH 7.0) at 37°C and gassed with compressed air. Dextrose was added to this solution immediately prior to experiments to a final concentration of 5.6 mM. ENaC and CaCC were inhibited as previously described herein. 0.1 μM forskolin/IBMX (3-isobutyl-1-methylxanthine) added apically was used to activate CFTR, and 1 μM CFTR-inh172 was used to inhibit CFTR.

Each successive addition of reagent was allowed approximately 10 minutes to equilibrate before the addition of the next reagent.

^{13}C NMR studies of $H^{13}CO_3^-$ efflux from POPC liposomes. Palmitoyl oleoyl phosphatidylcholine (POPC) was obtained as a 25 mg/mL solution in $CHCl_3$ from Avanti Polar Lipids (Alabaster, AL) and was stored at -20 ºC under an atmosphere of dry argon and used within 3 months. Prior to preparing a lipid film, this solution was warmed to ambient temperature to prevent condensation from contaminating the solution and degrading the lipid film. Cholesterol (Sigma Aldrich) was purified by recrystallization from ethanol. $NaH^{13}CO_3$ was obtained as a white solid from Sigma Aldrich. To a 20 mL scintillation vial (Fisher Scientific) was added 42 mg of solid cholesterol, followed by 14 mL of POPC solution. The solvent was removed with a gentle stream of nitrogen, and the resulting lipid film was stored under high vacuum for a minimum of twelve hours prior to use. The film was then hydrated with 2 mL of 260 mM $NaH^{13}CO_3$ in 40 mM HEPES buffer pH 7.5 (D_2O), and vortexed vigorously for approximately 3 minutes to form a suspension of multilamellar vesicles (MLVs). The lipid suspension was then subjected to 15 freeze-thaw cycles, where the suspension was alternatingly allowed to freeze in a liquid nitrogen bath, followed by thawing in a 50 °C water bath. The resulting lipid suspension was pulled into a Hamilton (Reno, NV) 1 mL gastight syringe and the syringe was placed in an Avanti Polar Lipids Mini-Extruder. The lipid solution was then passed through a 5.00 μm Millipore (Billerica, MA) polycarbonate filter 35 times, the newly formed large unilamellar vesicle (LUV) suspension being collected in the syringe that did not contain the original suspension of MLVs to prevent the carryover of MLVs into the LUV solution. To obtain a sufficient quantity of LUVs, two independent 1 mL preparations were pooled together for the dialysis and subsequent efflux experiments. The newly formed LUVs were dialyzed using Pierce

(Rockford, IL) Slide-A-Lyzer MWCO 3,500 dialysis cassettes, 3 mL capacity. The LUV suspension was dialyzed 10 times against 300 mL of 87 mM Na_2SO_4 in 40 mM HEPES buffer pH 7.3 (H_2O) with stirring. The first dialysis was four hours long, while the subsequent nine dialyses were performed for 1 hour.

Determination of total phosphorus was adapted from a previous report (*37*). The LUV solution was diluted fortyfold with 87 mM Na_2SO_4 in 40 mM HEPES buffer pH 7.3 (D_2O). Three 10 μL samples of the diluted LUV suspension were added to three separate 7 mL vials. Subsequently, the solvent was removed with a stream of N_2. To each dried LUV film, including a fourth vial containing no lipids that was used as a blank, was added 450 μL of 8.9 M H_2SO_4. The four samples were incubated open to ambient atmosphere in a 225 °C aluminum heating block for 25 min and then moved to 23 °C and allowed to cool for 5 minutes at room temperature. After cooling, 150 μL of 30% w/v aqueous hydrogen peroxide was added to each sample, and the vials were returned to the 225 °C heating block for 30 minutes. The samples were then moved to 23 °C and allowed to cool for 5 minutes at room temperature before the addition of 3.9 mL water. Then 500 μL of 2.5% w/v ammonium molybdate was added to each vial, and the resulting mixtures were then vortexed briefly and vigorously five times. Subsequently, 500 μL of 10% w/v ascorbic acid was added to each vial, and the resulting mixtures were then vortexed briefly and vigorously five times. The vials were enclosed with a PTFE lined cap and then placed in a 100 °C aluminum heating block for 7 minutes. The samples were moved to 23 °C and allowed to cool for approximately 15 minutes at room temperature to 23 °C prior to analysis by UV/Vis spectroscopy. Total phosphorus was determined by observing the absorbance at 820 nm and comparing this value to a standard curve obtained through this method and a standard phosphorus solution of known concentration.

The pooled LUV solution was diluted to 70 mM with 87 mM Na_2SO_4, 40 mM HEPES buffer, pH 7.3 (D_2O), and 0.025% (w/v) ^{13}C D-glucose (1-^{13}C) (Sigma Aldrich) was added as an internal standard. ^{13}C NMR spectra were acquired on a Bruker Avance III HD 500 MHz NMR spectrometer equipped with a 5 mm BBFO CryoProbe. The ^{13}C frequency was set to 125.83 MHz, and spectral width was 31,512 Hz. The instrument was locked on D_2O. Experimental conditions were: acquisition time, 0.93 s; 90° pulse width, 10.0 μs; relaxation delay, 0.2 s; number of scans, 256; temperature 25 °C.

For each experiment, 1.4 μL of vehicle, AmB, or C35deOAmB (17.5 μM final concentration, stock solution was 100 times more concentrated in DMSO) was added to 140 μL of the liposome suspension. The liposome suspension was immediately transferred to a New Era (Vineland, NJ) micro NMR sample tube (3 mm lower/5 mm upper), and 12 consecutive FIDs were obtained as described above. For experimental runs with $MnCl_2$, 5 μL of a 50 mM $MnCl_2$ solution was added after the addition of AmB. To effect complete ion release, 10 μL of a 30% (v/v) solution of triton X-100 (Sigma Aldrich) was added to the liposome suspension before data acquisition (*16, 38-40*).

Studies of proton efflux from POPC liposomes. Proton efflux from POPC/10% cholesterol liposomes was determined as previously described (*17*).

Studies of Na^+, K^+, Cl^-, and $H^{13}CO_3^-$ efflux from POPC liposomes. Sodium, potassium, and chloride measurements were obtained using a Denver Instruments (Denver, CO) Model 225 pH meter equipped with the appropriate ion selective probe inside a Faraday cage. Sodium selective measurements were obtained using an Orion micro sodium electrode (Thermo 9811BN). Potassium selective measurements were obtained with a World Precision Instruments potassium selective electrode (World Precision Instruments KWIKPOT-2, TIPK) and a reference electrode

(World Precision Instruments DRIREF-2). The electrode was filled with 1000 ppm KCl standard solution and conditioned in a 1000 ppm KCl standard solution for 15 minutes prior to potassium selective measurements. Chloride selective measurements were obtained using an Orion combination chloride electrode (Thermo 9617BNWP). For sodium and potassium efflux experiments, measurements were made on 1.5 mL solutions that were magnetically stirred in 7 mL vials incubated at 23 °C. For chloride efflux experiments, measurements were made on 4 mL solutions that were magnetically stirred in 20 mL vials incubated at 23 °C. For sodium, potassium, and chloride efflux experiments, the concentration of each ion was sampled every 10 seconds throughout the course of the efflux experiments.^{13}C NMR spectra for bicarbonate efflux experiments were acquired on a Varian Inova 600MHz NMR spectrometer with a Varian 5 mm broadband autox probe. The ^{13}C frequency was set to 150.8 MHz, and spectral width was 38 kHz. The instrument was locked on D_2O. Experimental conditions were: acquisition time, 0.93 s; 90° pulse width, 6.70 μs; relaxation delay, 0.2 s; number of scans, 256; temperature 27 °C. The inverse-gated ^{13}C spectra were collected.

Liposome preparation. Cholesterol-containing POPC lipid films were prepared as described above and stored under high vacuum for a minimum of twelve hours prior to use. For sodium efflux experiments, the film was rehydrated with 2 mL of 250 mM $NaHCO_3$, 40 mM HEPES buffer, pH 7.5 and vortexed vigorously for approximately 3 minutes to form a suspension of multilamellar vesicles (MLVs). For potassium efflux experiments, the film was rehydrated with 2 mL of 250 mM $KHCO_3$, 40 mM HEPES buffer, pH 7.5. For chloride efflux experiments, the film was rehydrated with 2 mL of 250 mM NaCl, 40 mM HEPES buffer, pH 7.5. For bicarbonate efflux experiments, the film was rehydrated with 2 mL of 250 mM $NaH^{13}CO_3$, 40 mM HEPES buffer, pH 7.5 (D_2O). To obtain a sufficient quantity of LUVs, at least two independent lipid film

preparations were pooled together for the subsequent formation of LUVs. The freeze-thaw and extrusion protocol was as previously described for ^{13}C liposomes. Multiple 1 mL preparations were pooled together for the dialysis and subsequent efflux experiments. The newly formed LUVs were dialyzed using Pierce (Rockford, IL) Slide-A-Lyzer MWCO 3,500 dialysis cassettes, 15 mL capacity. The LUV suspension was dialyzed 3 times against 600 mL of 62.5 mM $MgSO_4$, 40 mM HEPES buffer, pH 7.3. The first two dialyses were two hours long, while the final dialysis was performed overnight. Determination of phosphorous content was performed as described above.

Efflux from LUVs. The pooled LUV suspension was diluted to 70 mM with 62.5 mM $MgSO_4$, 40 mM HEPES buffer, pH 7.3. The LUV suspension (1.5 mL for sodium, and 4 mL for chloride and potassium) was added to either a 7 mL or 20 mL vial and gently stirred. The appropriate probe was inserted, and data were collected for one minute prior to addition of AmB. For sodium efflux experiments, 15 μL of either vehicle or AmB (70 μM final concentration, stock solution was 100 times more concentrated in DMSO) was added to 1.5 mL of LUV suspension, and data were collected for 10 minutes. To effect complete ion release, 15 μL of a 30% v/v solution of triton X-100 was added, and data were collected for an additional five minutes. For chloride and potassium efflux experiments, 40 μL of either vehicle or AmB (70 μM final concentration, stock solution was 100 times more concentrated in DMSO) was added to 4 mL of LUV suspension, and data were collected for 10 minutes. To effect complete ion release, 40 μL of a 30% v/v solution of triton X-100 was added, and data were collected for an additional five minutes. For bicarbonate efflux experiments, 5 μL of either vehicle or AmB (70 μM, 100X stock in DMSO) was added to 500 μL of the pooled LUV suspension, and consecutive FIDs were acquired for 60 minutes. 5 μL of a 30% v/v solution of triton X-100 to effect complete ion release.

The efflux data from each run was normalized to the percent of total ion release from 0 to 100%. For bicarbonate efflux experiments, after lysis of the liposome suspension, the integration of the signal corresponding to extravesicular bicarbonate relative to the integration of the ^{13}C glucose standard was scaled to correspond to 100% efflux. For each experimental run with AmB addition, the signal corresponding to extravesicular bicarbonate was integrated relative to the ^{13}C glucose standard for each FID. The scaling factor S was calculated for each experiment using the following relationship:

$$\left[\frac{[\mathrm{Ion}]_{final}}{[\mathrm{Ion}]_{initial}} - 1\right] \cdot S = 100$$

Each data point was then multiplied by S before plotting as a function of time.

Intracellular pH of NuLi and CuFi monolayers. Intracellular pH was measured using pHrodo® Green AM Intracellular pH Indicator (Invitrogen, P35373). NuLi and CuFi-1 epithelia cultured on 0.33 cm^2 24-well plate Transwell Clear Polyester Membrane inserts were used for this experiment and basolateral media was changed the day prior to experimentation. 10 µL of the pHrodo™ Green AM in DMSO was added to 100 µL of PowerLoad™ concentrate. The dye solution was then diluted into 10 mL of USG media to make the staining solution. The existing basolateral media was removed from cells, and the basolateral side of each culture was rinsed once with USG media. The basolateral media was then replaced with the pHrodo™ AM staining solution and incubated at 37°C for 30 minutes. The basolateral staining solution was then removed and replaced with USG media prior to measurement. The cultures were analyzed using a Synergy H1 MONO Plate Reader on fluorescent endpoint setting with excitation 506 nm and emission 540 nm to establish the baseline fluorescence of the untreated cultured epithelia. To quantify absolute pH value, a cell loading solution was prepared utilizing an Intracellular pH Calibration Buffer Kit (Invitrogen, P35379). 10 µL of the provided valinomycin/nigericin stock

solution was diluted in 10 mL of the desired Cellular pH Calibration Buffer (Component C/pH 6.5, Component D/pH 7.5, Component D/adjusted to pH 8.5) for a final concentration of 10 μM. After the baseline measurement, the basolateral media was removed, washed one time, and replaced with the prepared cell loading solution. This was incubated at 37°C for 5 minutes. The cultures were again analyzed using a plate-reader on fluorescent endpoint setting with excitation 506 nm and emission 540 nm to measure the calibrated fluorescence values. These three values per culture were pooled and averaged to get a linear standard curve, from which the intracellular pH was extrapolated.

Measurement of ASL pH in cell line and primary cultures of airway epithelia. 0.33 cm^2 NuLi, CuFi, and primary cultured epithelia were used for this experiment. The ratiometric pH indicator SNARF-conjugated dextran (Molecular Probes) was used to measure ASL pH. SNARF powder was suspended via sonication in perfluorocarbon (FC-72, Sigma) and distributed onto the apical surface. ASL pH was measured 2 hr later (*6, 9, 41*). SNARF was excited at 488 nm and emission was recorded at 580 nm and 640 nm using a Zeiss LSM 800 microscope at 40X water immersion for cell line cultures and a Zeiss LSM 510 microscope for primary cultures. To generate a standard curve for pH determination, SNARF was dissolved in colorless pH standards and fluorescence ratios were converted to pH.

Agents tested in this assay were first lyophilized into powder and then suspended in the appropriate volume of perfluorocarbon (FC-72, Sigma) and sonicated for 1 minute to suspend. AmBisome should not be sonicated; instead, the fine powder was suspended by vortexing. 20 μL of this suspension was administered onto the surface of cultured airway epithelia (0.33 cm^2) at the following approximate concentrations in suspension:

amphotericin B 0.25-100 μM

amphotoricin B-cholesterol complex 0.5-100 μM

C35deOamphotericin B 2 μM (*15*)

10 mM ouabain (inhibition of Na+/K+ ATPase) (*42*)

10 μM ivacaftor/10 μM forskolin (*9*)

AmBisome 0.25-2450 μg/mL

In all experiments, ASL pH of compound-treated epithelia was measured compared the results to vehicle-treated epithelia.

For apical AmB administration, cultured airway epithelia were incubated for 30 min – 48 hrs at 37°C before measurement of ASL pH. For AmB-cholesterol complex and C35deOAmB administration, cultured airway epithelia were incubated for 48 hrs at 37°C before measurement of ASL pH. To test the effect of Na+/K+ ATPase inhibition, AmB was administered 47 hours prior to 10 mM ouabain addition, and cultured airway epithelia were incubated for an additional 1 hr at 37°C before measurement of ASL pH. For 10 μM ivacaftor/10 μM forskolin administration, cultured airway epithelia were incubated for 2 hrs at 37°C before measurement of ASL pH (*9*). For basolateral AmB administration, a 2 mM stock of AmB in DMSO was diluted 1000-fold to a final concentration of 2 μM in USG media. The basolateral media of cultured airway epithelia was replaced with the AmB-containing USG media and incubated for 48 hrs at 37°C before measurement of ASL pH.

pH-stat titration of NuLi and CuFi monolayers. Large diameter NuLi and CuFi-1 cultured epithelia were used for this experiment (4.67 cm^2). These cultures were mounted in a dual-channel Ussing chamber (Warner U2500) using the culture cup insert for Transwell adapter, 24mm (U9924T-24). The membranes were bathed at 37°C on the apical side with a buffer-free solution (140 mM NaCl, 2 mM KCl, 2 mM $CaCl_2$, and 1 mM $MgCl_2$, 15 mM dextrose, gassed

with air) and on the basolateral side with either a bicarbonate buffer (120 mM NaCl, 25 mM $NaHCO_3$, 5 mM KCl, 2 mM $CaCl_2$, 1.2 mM $MgCl_2$, 13.75 NaH_2PO_4, 5.6 mM dextrose, pH adjusted to 7.0) or a bicarbonate-free buffer (140 mM NaCl, 2 mM KCl, 2 mM $CaCl_2$, 1 mM $MgCl_2$, 10 mM HEPES, 5 mM dextrose, pH adjusted to 7.0). A microdiameter pH electrode (89231-590) and temperature probe (Radiometer Analytical T201 Temperature Sensor, E51M001) and titration burette attached to a Hach TIM856 NB pH/EP/Stat pH-STAT Titrator (R41T028) were inserted into the apical chamber. The basolateral chamber was covered with the chamber lid to prevent gas exchange. The pH electrode was then calibrated using known pH solutions (Hach, S11M002, S11M004, S11M007).

The apical pH was titrated to a target pH of 6.0 using 1 mM HCl as titrant (min speed 0.25 mL/min, max speed 0.35 mL/min) (*25, 43-45*). Acid titration was measured over 20 minutes to establish a baseline value for the cultured epithelia (max speed 2 mL/min). Both apical and basolateral bathing solutions were then removed. A stock solution of AmB in DMSO was added to a final concentration of 0.5, 1, or 2 μM in an aliquot of buffer-free solution and added to the apical chamber, and the basolateral chamber was replaced with fresh bicarbonate or bicarbonate-free buffer. The apical pH was once again titrated to a target pH of 6.0 using 1 mM HCl as titrant. Acid titration was then measured over another 20 minutes to evaluate AmB-mediated pH change in the apical solution.

Data was plotted as nmoles of H^+ titrated in per minute, and the slope of this curve was divided by the area of the culture (4.67 cm^2) to obtain the rate of acid titration (nmoles $H^+/min/cm^2$).

$H^{14}CO_3^-$ transport across NuLi and CuFi monolayers. ^{14}C-labeled sodium bicarbonate was obtained as a sterile 35.7 mM aqueous solution pH 9.5 (MP Biomedicals). 0.33 cm^2 NuLi and

CuFi cultured epithelia were used in this experiment. All experiments were run less than 2 months post seeding. Fresh USG media was added to the basolateral side prior to experimentation. The apical membrane was treated with 20 μL of vehicle, AmB, or ivacaftor/forskolin as a suspension in perfluorocarbon-72 (Sigma Aldrich), and the cultured epithelia were incubated for 48 hours at 37 °C in a 5% CO_2 atmosphere. After 48 hours, 5 μL of a 1.4 mM $H^{14}CO_3^-$ solution in USG media was added to the basolateral media. The cultured epithelia were then incubated at 37 °C for 10 minutes. After 10 minutes, the apical membrane of the cultured epithelia was washed with 200 μL of PBS. The ASL wash and a 200 μL aliquot of the basolateral media were diluted in scintillation cocktail and analyzed via liquid scintillation counting (*5*).

Airway surface liquid (ASL) height assay. ASL height was studied using an established fluorescent dye assay (*27, 46*). 0.33 cm^2 NuLi and CuFi-1 cultured epithelia were used in this experiment. 24 hours prior to the start of experiment, the apical side of all cultured epithelia was rinsed three times with warm PBS to remove excess mucus. NuLi epithelia were treated with perfluorocarbon (FC-72) vehicle, and CuFi epithelia were treated with 20 μL vehicle, 0.005, 0.5, or 50 μM AmB, or 0.5 μM C35deOAmB suspended in perfluorocarbon (FC-72, Sigma) and incubated for 24 hours at 37 ^oC. Basolateral treatments of 0.5 μM AmB or 500 μM bumetanide were administered in DMSO. After 24 hours, 2.5 μL of a 2 mg/mL 70kDa Texas Red-dextran conjugate (Molecular Probes) solution in PBS was added to the apical side of the epithelia, followed by 100 μL of FC-770 to prevent evaporation. Then the culture support was placed on top of 100 μL of PBS on a 10 mm glass bottom Fluorodish for imaging (World Precision Instruments). Epithelia were imaged immediately after dye addition and again at 24 hours to examine dye absorption. Three Z-stack images per membrane in biological n = 3 were taken on

an Zeiss LSM700 confocal microscope at 40x oil immersion. These images were analyzed using ImageJ[29] to determine the average ASL height in the center 1300 pixels of each image. Images were smoothed, converted to 8-bit, and thresholded to most accurately represent the red area. The parameters for Analyze Particles were particles from 1-Infinity μm^2 in size and from 0%-100% circularity. Height was determined by dividing the area output in pixels by the known 1300 pixel width and converted to microns using the known scaling factor of 0.49 μm/pixel.

Viscosity of AmB-treated primary cultures of airway epithelia. ASL viscosity in airway epithelial cultures was determined as previously described (*8, 9*). The apical surface was not washed for at least 2 weeks before study. Cultured epithelia were treated with 2 μM AmB administered in perfluorocarbon (FC-72, Sigma) as previously described for 48 hours. FITC-dextran (70 kD, Sigma) was then administered to the apical surface of epithelia as a dry powder 2 hrs before measurement of viscosity. FRAP was assayed in a humidified chamber at 37°C using a Zeiss LSM 510 META microscope. Images were acquired until maximal recovery was reached. At least 6 recovery curves from different locations in each culture were acquired and averaged to obtain data for one epithelial culture. The time constant (τsaline) was calculated by regression analysis from fluorescence recovery curves. Viscosity is expressed relative to the time constant of saline (τASL/τsaline).

Antibacterial activity of AmB-treated primary cultures of airway epithelia. Staphylococcus aureus-coated gold grids were used to measure antibacterial activity of airway epithelial cultures as previously described (*6, 41*). Bacteria-coated gold TEM grids were placed onto the apical surface of airway epithelia for 1 minute after 48 hours of perfluorocarbon (FC-72, Sigma), 2 μM AmB, or 2 μM C35deOAmB treatment. As controls, bacteria-coated grids were also placed in saline or AmB in FC-72 laid over saline to simulate the administration method for 1 minute.

After removal, bacteria on the grids were assessed for viability using Live/Dead BacLight Bacterial Viability assay (Invitrogen). Viability was determined in 4-6 fields to determine the percentages of dead bacteria.

Animals for study. We studied female and male newborn pigs with targeted disruption of the *CFTR* gene *CFTR*$^{-/-}$, generated from mating *CFTR*$^{+/-}$ pigs. We also studied WT siblings using the same protocol. Pigs were obtained from Exemplar Genetics. The University of Iowa Animal Care and Use Committee approved all animal studies.

Measurement of ASL pH in CFTR$^{-/-}$ and WT piglets. ASL pH was measured in pigs *in vivo* as previously described (*7, 41*). To administer AmBisome in pig trachea, pigs were initially sedated with ketamine (Ketaject, Phoenix; 20 mg/kg, i.m. injection) and anesthetized using propofol (Diprivan, Fresenius Kabi; 2 mg/kg, i.v. injection). The trachea was surgically exposed and accessed anteriorly, and a small anterior window was cut through the tracheal rings. To mimic physiologic conditions, data was obtained in a 100% humidified chamber at 37°C and constant 5% CO_2.

For the first CFTR$^{-/-}$ and one WT piglet, a baseline ASL pH measurement was taken for about 8 minutes before 60 μL of 100 μg/mL AmBisome® was administered to the tracheal window. ASL pH was continually measured for 60 minutes. Then, 60 μL of 1 mg/mL of AmBisome was administered to the tracheal window and continually measured for another 60 minutes. For the second CFTR$^{-/-}$ piglet, a baseline ASL pH measurement was taken for about 8 minutes before 60 μL of FC-72 vehicle was administered to the tracheal window as an internal control. ASL pH was continually measured for another 30 minutes. Then, 60 μL of 1 mg/mL of AmBisome was administered to the tracheal window and continuous measurements were then taken for 106 minutes.

Synthesis and characterization of small molecules. Commercial reagents were purchased from Sigma-Aldrich, Fisher Scientific, or Steraloids, and were used without further purification unless otherwise noted. Solvents were purified via passage through packed columns as described by Pangborn and coworkers (THF, MeOH, CH_2Cl_2: dry neutral alumina; DMF: activated molecular sieves)[1]. All water was deionized prior to use. Triethylamine was freshly distilled under an atmosphere of nitrogen from CaH_2 before use. **1** was commercially available through Sigma-Aldrich. The following compounds were prepared according to known literature procedures: ***2***[2-4], ***3***[5-7], and ***4***[8-9]. Their full spectroscopic analysis can be found below.

Reactions were monitored by analytical thin layer chromatography (TLC) performed using the indicated solvent on E. Merck silica gel 60 F254 plates (0.25 mm). Compounds were visualized by exposure to a UV lamp (λ = 254 nm or 366 nm), and/or a solution of $KMnO_4$ stain, followed by heating using a Varitemp heat gun. Flash column chromatography was performed using Merck silica gel grade 9385 60Å (230-240 mesh).

^{1}HNMR and ^{13}CNMR were recorded at 20°C on Varian Unity 400, Unity Inova 400, Unity Inova 500NB, Varian XR500, or Unity 500 instruments. Chemical shifts (δ) are reported in parts per million (ppm) downfield from tetramethylsilane and referenced to residual protium in the NMR solvent ($CHCl_3$, δ=7.26; MeOH, δ=3.31, center line; acetone, δ=2.05, center line) or to added tetramethylsilane (δ=0.00). Data are reported as follows: chemical shift, multiplicity (s=singlet, d=doublet, t=triplet, q=quartet, m=multiplet, br=broad, app=apparent), coupling constant (*J*) in Hertz (Hz), and integration. ^{13}CNMR are referenced to carbon resonances in the NMR solvent ($CDCl_3$, δ=77.16, center line; MeOH, δ=49.00, center line; acetone, δ=29.84, center line). High resolution mass spectra (HRMS) were performed at the University of Illinois, School of Chemical Sciences Mass Spectrometry Laboratory. HPLC characterization were

performed using an Agilent 1260 Infinity series analytical HPLC with a 3.5 μm C18 column (Agilent Technologies).

Synthesis of *Hydroxybisnorcholenic-spermine-sulfonate, GL-172* (2)

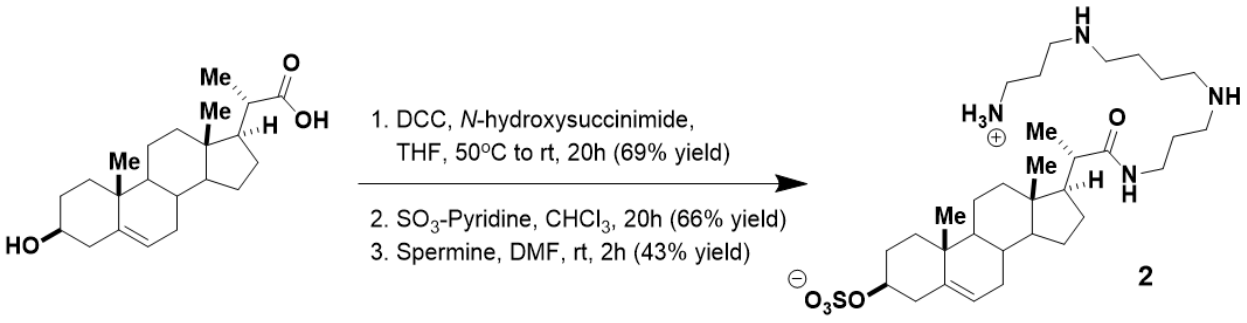

2 was prepared according to literature precedent in 19.6% overall yield starting from Fernholz Acid[2-4]. Characterization of this compound was consistent with previously reported data[4].

TLC (8:2:1 $CHCl_3$:MeOH:NH_4OH)

R_f = 0.58, visualized by $KMnO_4$ stain

^{1}HNMR (500 MHz, CD_3OD)

δ 5.44-5.29 (m, 1H), 4.18-4.10 (m, 1H), 3.29-3.19 (m, 1H), 3.17 (dt, *J* = 13.6, 6.7 Hz, 1H), 2.77 (app t, *J* = 7.1 Hz, 2H), 2.71 (app t, *J* = 7.2 Hz, 2H), 2.69-2.62 (m, 6H), 2.58-2.46 (m, 1H), 2.38-2.31 (m, 1H), 2.31-2.18 (m, 2H), 2.07 (d, *J* = 13.0 Hz, 1H), 1.99 (app t, *J* = 13.4 Hz, 1H), 1.91-1.83 (m, 1H), 1.79-1.67 (m, 6H), 1.64-1.55 (m, 4H), 1.55-1.45 (m, 4H), 1.37-1.22 (m, 3H), 1.15 (d, *J* = 6.8 Hz, 3H), 1.14-1.07 (m, 2H), 1.03 (s, 3H), 0.97 (td, *J* = 11.2, 4.9 Hz, 2H), 0.75 (s, 3H)

^{13}CNMR (125 MHz, CD_3OD)

δ 179.8, 142.2, 122.3, 72.4, 57.9, 54.0, 51.7, 50.1, 49.9, 48.0, 47.5, 45.1, 43.4, 43.0, 41.0, 40.4, 38.6, 37.7, 37.6, 33.3, 33.0, 32.3, 31.6, 29.8, 28.5, 27.8, 27.8, 25.4, 22.2, 19.9, 18.0, 12.5

HRMS (ESI+)

Calculated for $C_{32}H_{59}N_4O_5S$ $[M+H^+]^+$	:	611.4206
Observed	:	611.4205

HPLC (0.1% TFA in H_2O to MeCN gradient, 214 nm)

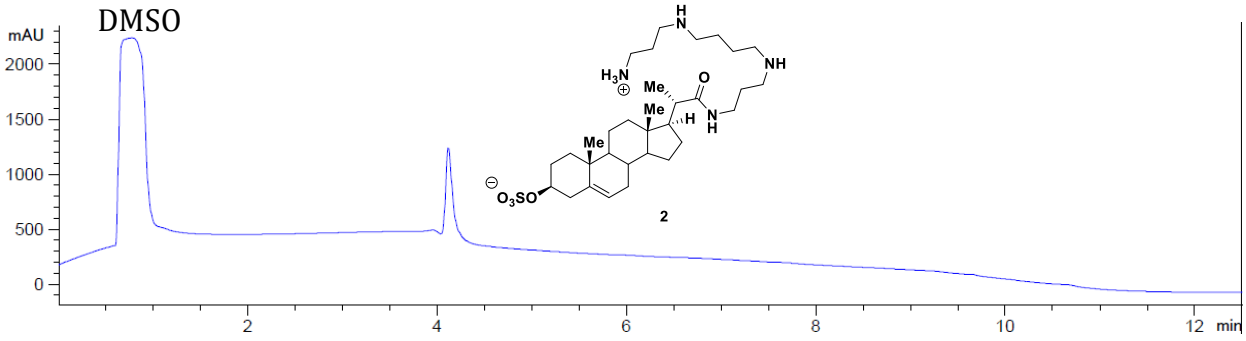

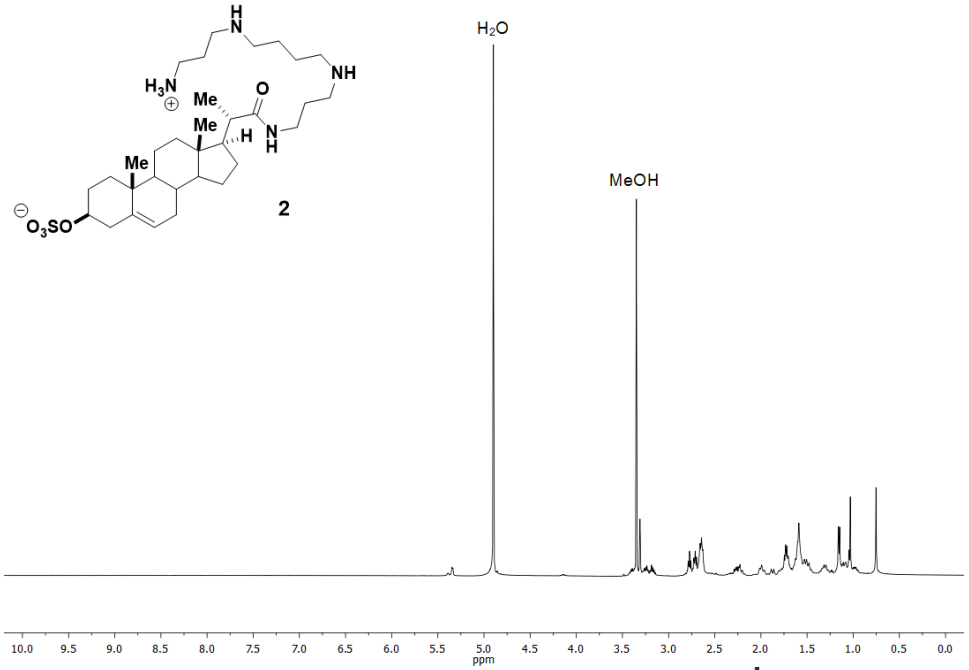

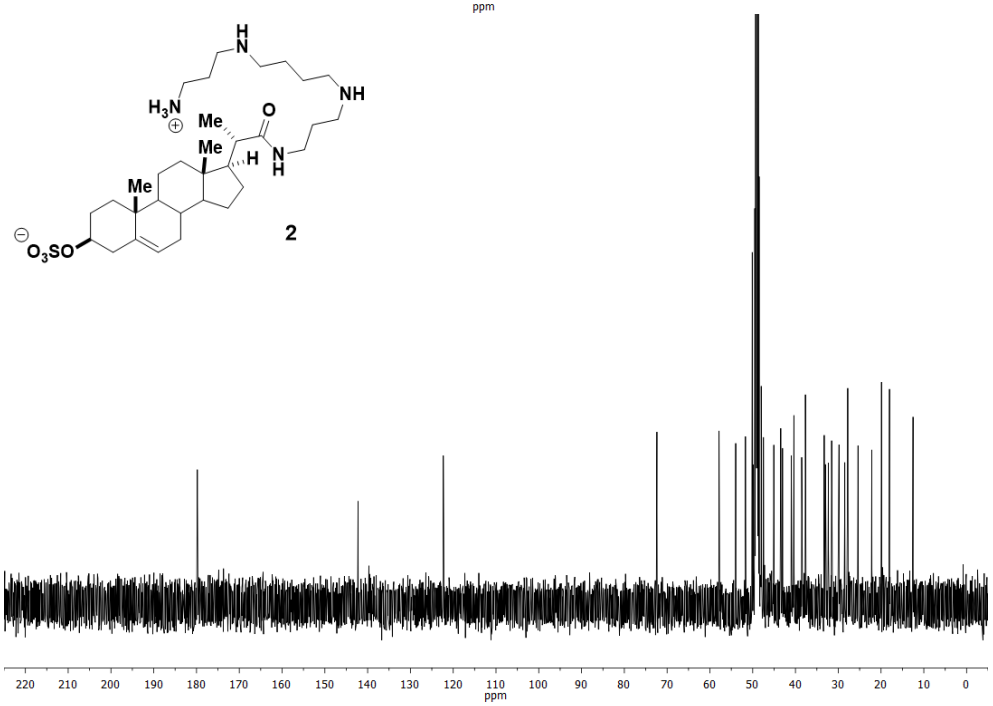

Synthesis of *Methyl 3α-acetoxy-7α,12α-di[(4-nitrophenylaminocarbonyl)amino]-5β-cholan-24-oate, Cholapod 2e* (3)

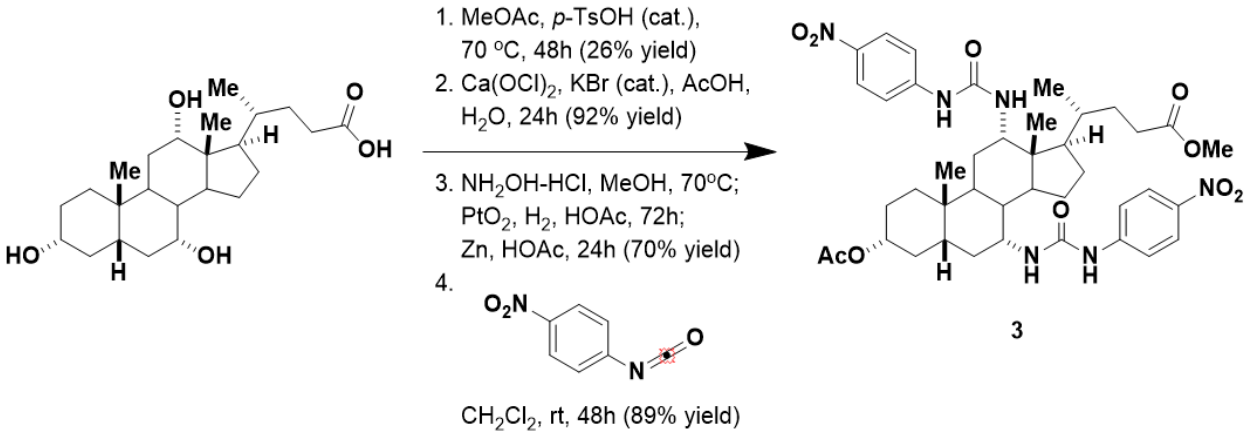

3 was prepared according to literature precedent in 14.9% overall yield starting from cholic acid[5-7]. Characterization of this compound was consistent with previously reported data[5-7].

TLC (1:2 Hexanes:Ethyl Acetate)

R_f = 0.40, visualized by UV (254 nm and/or 366 nm) and/or $KMnO_4$ stain

^{1}HNMR (500 MHz, Acetone-d_6)

δ 8.85 (br s, 1H), 8.66 (br s, 1H), 8.15 (app d, *J* = 9.1 Hz, 4H), 7.73 (app d, *J* = 9.2 Hz, 4H), 6.24-6.14 (app br s, 2H), 4.56-4.47 (m, 1H), 4.21-4.16 (m, 1H), 4.12-4.06 (m, 1H), 3.55 (s, 3H), 2.29-2.23 (m, 4H), 2.20-2.09 (m, 2H), 2.02-1.94 (m, 4H), 1.91 (s, 3H), 1.89-1.77 (m, 4H), 1.75-1.55 (m, 4H), 1.52-1.22 (m, 6H), 0.91 (s, 3H), 0.89 (s, 3H), 0.87 (s, 3H)

^{13}CNMR (125 MHz, Acetone-d_6)

δ 174.4, 170.2, 154.5, 148.0, 148.0, 147.9, 142.2, 142.1, 125.9, 117.7, 117.7, 74.6, 53.9, 51.5, 49.1, 47.0, 45.6, 42.1, 38.0, 35.8, 35.8, 35.5, 33.4, 31.5, 31.2, 27.9, 27.6, 27.3, 24.0, 23.2, 21.3, 17.5, 14.0

HRMS (ESI+)

Calculated for $C_{41}H_{55}N_6O_{10}$ $[M+H^+]^+$: 791.3980

Observed : 791.3977

Analytical HPLC (H_2O to MeCN gradient, 360 nm)

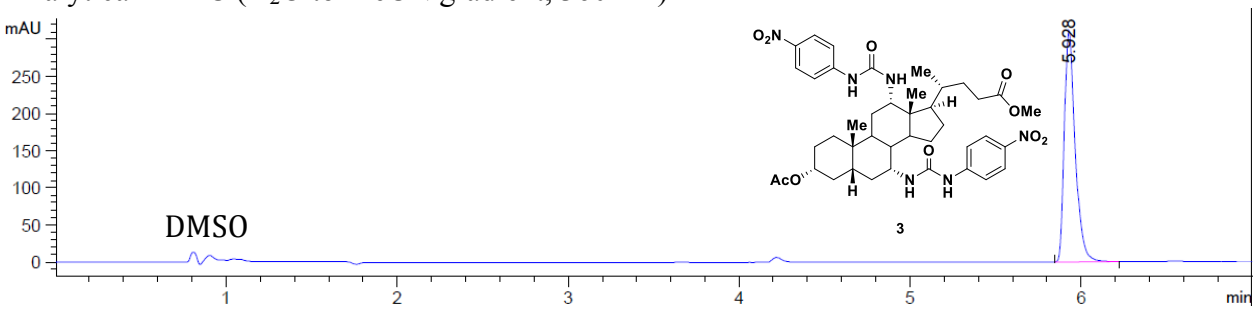

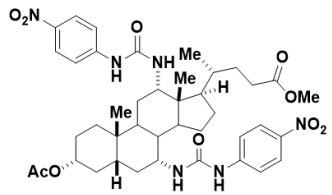

3

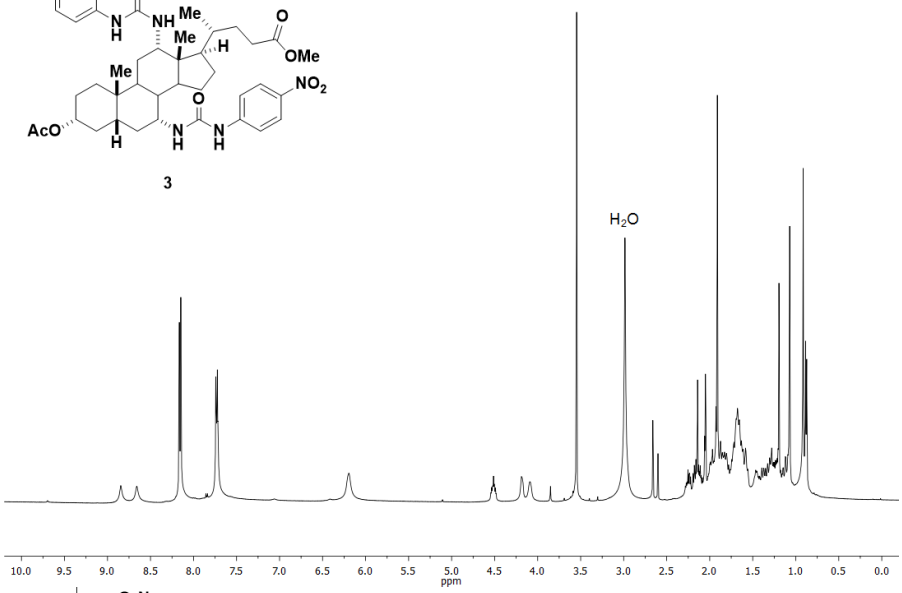

3

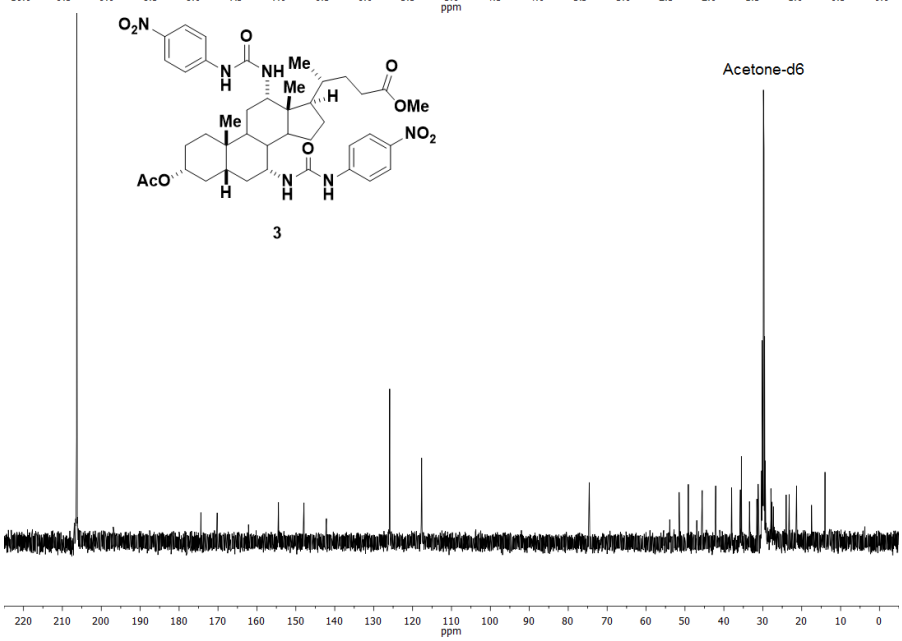

Synthesis of *N*[1],*N*[3]*-bis(((R)-1-(isobutylamino)-4-methyl-1-oxopentan-2-yl)oxy)isophthalamide, Yang Channel* (4)

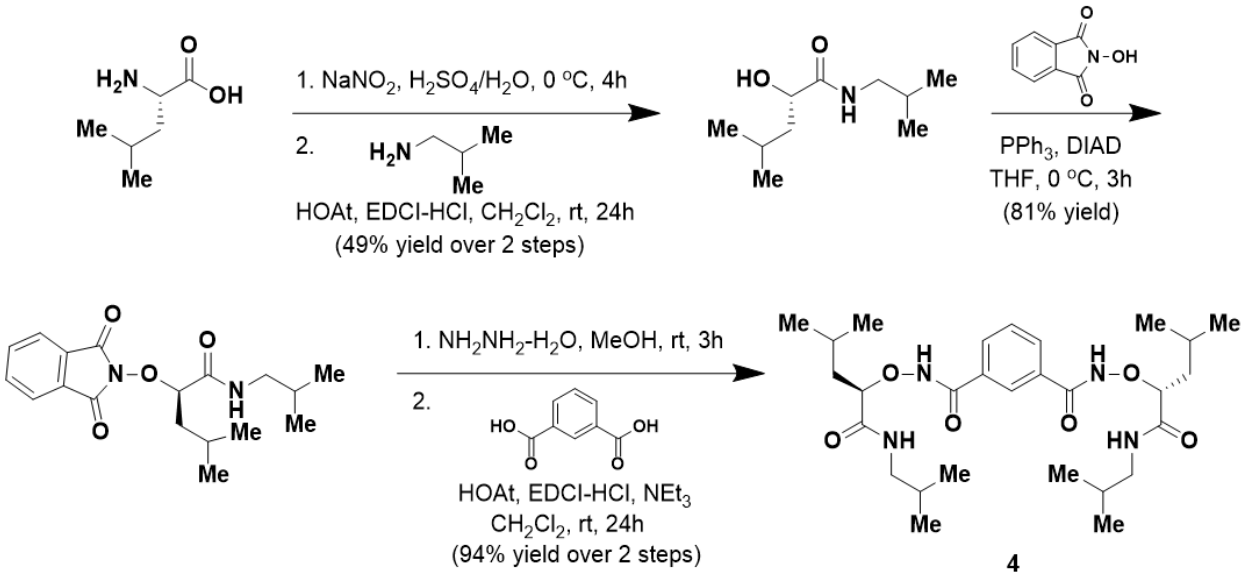

4 was prepared according to literature precedent in 37.3% overall yield starting from leucine[8,9]. Characterization of this compound was consistent with previously reported data[8,9].

TLC (1:1 Hexanes:Ethyl Acetate)

R_f = 0.33, visualized by UV (254 nm) and/or $KMnO_4$ stain

^{1}HNMR (500 MHz, $CDCl_3$)

δ 11.06 (br s, 2H), 8.16 (br s, 3H), 8.01 (dd, *J* = 7.7, 1.6 Hz, 2H), 7.51 (t, *J* = 7.8 Hz, 1H), 4.39 (dd, *J* = 9.7, 3.6 Hz, 2H), 2.99 (dt, *J* = 13.0, 6.4 Hz, 2H), 2.87 (dt, *J* = 13.0, 6.4 Hz, 2H), 1.84-1.77 (m, 2H), 1.75-1.60 (m, 4H), 1.56 (ddd, *J* = 13.7, 9.0, 3.6 Hz, 2H), 0.87 (d, *J* = 6.6 Hz, 12H), 0.80 (d, *J* = 6.6 Hz, 6H), 0.74 (d, *J* = 6.6 Hz, 6H)

^{13}CNMR (125 MHz, $CDCl_3$)

δ 172.3, 166.1, 131.9, 131.4, 129.5, 125.3, 85.4, 46.8, 41.3, 28.4, 24.9, 23.3, 21.9, 20.1, 20.1

HRMS (ESI+)

Calculated for $C_{28}H_{47}N_4O_6$ $[M+H^+]^+$: 535.3496

Observed : 535.3497

Analytical HPLC (H_2O to MeCN gradient, 254 nm)

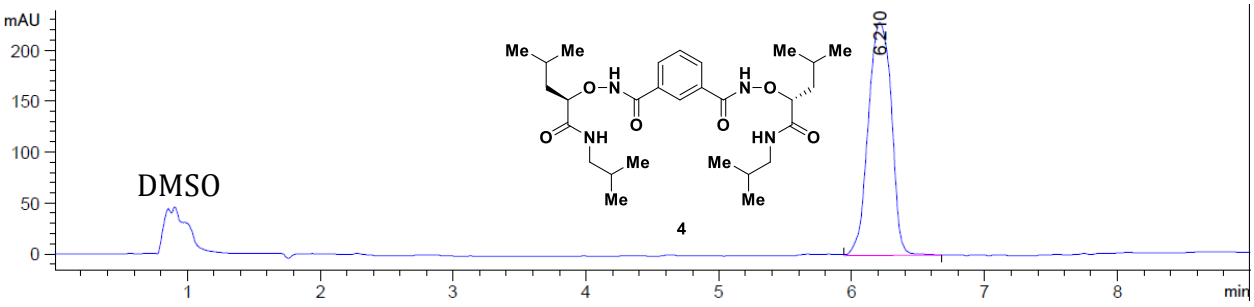

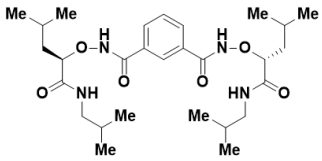

4

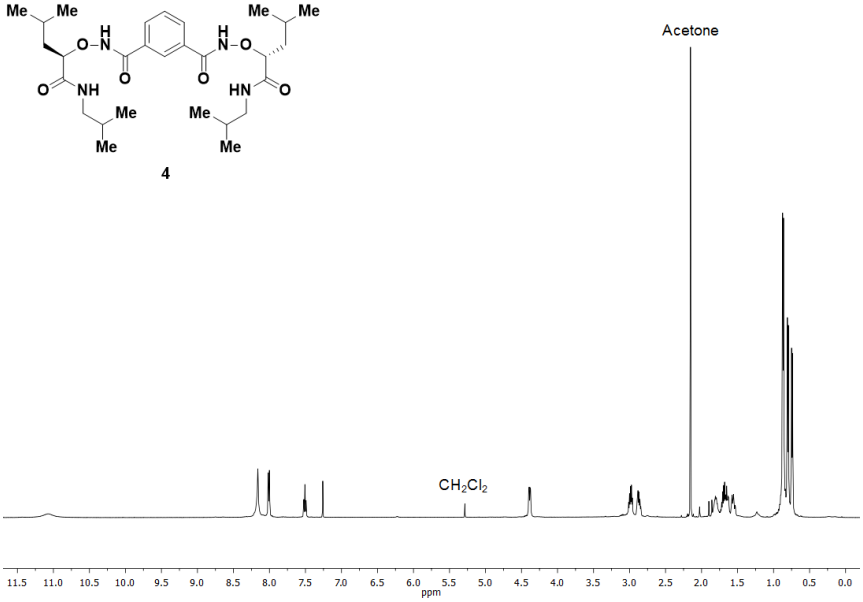

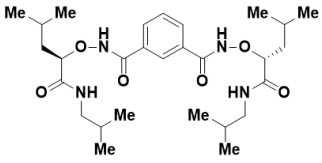

4

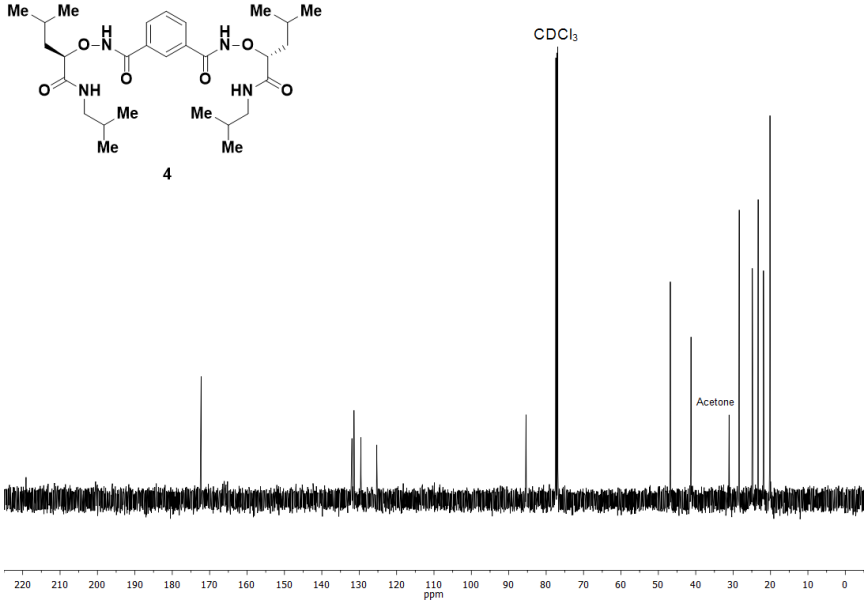

3.8 REFERENCES

1. D. A. Stoltz , D. K. Meyerholz , M. J. Welsh Origins of Cystic Fibrosis Lung Disease. *New England Journal of Medicine* **372**, 351-362 (2015).
2. M. P. Rogan, D. A. Stoltz, D. B. Hornick, Cystic Fibrosis Transmembrane Conductance Regulator Intracellular Processing, Trafficking, and Opportunities for Mutation-Specific Treatment. *Chest* **139**, 1480-1490 (2011).
3. L. Maiuri, V. Raia, G. Kroemer, Strategies for the etiological therapy of cystic fibrosis. *Cell Death Differ* **24**, 1825-1844 (2017).
4. A. G. Cioffi, J. Hou, A. S. Grillo, K. A. Diaz, M. D. Burke, Restored Physiology in Protein-Deficient Yeast by a Small Molecule Channel. *J Am Chem Soc* **137**, 10096-10099 (2015).
5. A. S. Grillo *et al.*, Restored iron transport by a small molecule promotes absorption and hemoglobinization in animals. *Science* **356**, 608-616 (2017).
6. V. S. Shah *et al.*, Airway acidification initiates host defense abnormalities in cystic fibrosis mice. *Science* **351**, 503-507 (2016).
7. M. H. Abou Alaiwa *et al.*, Repurposing tromethamine as inhaled therapy to treat CF airway disease. *JCI Insight* **1**, (2016).
8. X. X. Tang *et al.*, Acidic pH increases airway surface liquid viscosity in cystic fibrosis. *J Clin Invest* **126**, 879-891 (2016).
9. E. H. Chang *et al.*, Medical reversal of chronic sinusitis in a cystic fibrosis patient with ivacaftor. *Int Forum Allergy Rhinol* **5**, 178-181 (2015).
10. B. W. Ramsey *et al.*, A CFTR Potentiator in Patients with Cystic Fibrosis and the G551D Mutation. *New England Journal of Medicine* **365**, 1663-1672 (2011).
11. J. P. Garnett *et al.*, Hyperglycaemia and Pseudomonas aeruginosa acidify cystic fibrosis airway surface liquid by elevating epithelial monocarboxylate transporter 2 dependent lactate-H+ secretion. *Sci Rep* **6**, 37955 (2016).
12. F. Van Goor *et al.*, Rescue of CF airway epithelial cell function in vitro by a CFTR potentiator, VX-770. *Proceedings of the National Academy of Sciences* **106**, 18825-18830 (2009).
13. J. L. Taylor-Cousar *et al.*, Tezacaftor–Ivacaftor in Patients with Cystic Fibrosis Homozygous for Phe508del. *New England Journal of Medicine*, (2017).
14. N. M. Walker *et al.*, Cellular chloride and bicarbonate retention alters intracellular pH regulation in Cftr KO crypt epithelium. *Am J Physiol Gastrointest Liver Physiol* **310**, G70-80 (2016).
15. K. C. Gray *et al.*, Amphotericin primarily kills yeast by simply binding ergosterol. *Proc Natl Acad Sci U S A* **109**, 2234-2239 (2012).
16. J. T. Davis *et al.*, Using small molecules to facilitate exchange of bicarbonate and chloride anions across liposomal membranes. *Nat Chem* **1**, 138-144 (2009).
17. S. A. Davis *et al.*, C3-OH of Amphotericin B Plays an Important Role in Ion Conductance. *J Am Chem Soc* **137**, 15102-15104 (2015).
18. B. Shen, X. Li, F. Wang, X. Yao, D. Yang, A synthetic chloride channel restores chloride conductance in human cystic fibrosis epithelial cells. *PLoS One* **7**, e34694 (2012).
19. A. V. Koulov *et al.*, Chloride transport across vesicle and cell membranes by steroid-based receptors. *Angew Chem Int Ed Engl* **42**, 4931-4933 (2003).

20. C. Jiang *et al.*, Partial correction of defective Cl(-) secretion in cystic fibrosis epithelial cells by an analog of squalamine. *Am J Physiol Lung Cell Mol Physiol* **281**, L1164-1172 (2001).
21. M. El-Etri, J. Cuppoletti, Metalloporphyrin chloride ionophores: induction of increased anion permeability in lung epithelial cells. *Am J Physiol* **270**, L386-392 (1996).
22. L. N. Ermishkin, K. M. Kasumov, V. M. Potseluyev, Properties of amphotericin B channels in a lipid bilayer. *Biochim Biophys Acta* **470**, 357-367 (1977).
23. H. Kawase *et al.*, A dipeptidyl peptidase-4 inhibitor ameliorates hypertensive cardiac remodeling via angiotensin-II/sodium-proton pump exchanger-1 axis. *J Mol Cell Cardiol* **98**, 37-47 (2016).
24. J. Zabner *et al.*, Development of cystic fibrosis and noncystic fibrosis airway cell lines. *Am J Physiol Lung Cell Mol Physiol* **284**, L844-854 (2003).
25. D. Y. Cho, P. H. Hwang, B. Illek, H. Fischer, Acid and base secretion in freshly excised nasal tissue from cystic fibrosis patients with DeltaF508 mutation. *Int Forum Allergy Rhinol* **1**, 123-127 (2011).
26. V. S. Shah *et al.*, Relationships among CFTR expression, HCO(3)(−) secretion, and host defense may inform gene- and cell-based cystic fibrosis therapies. *Proceedings of the National Academy of Sciences of the United States of America* **113**, 5382-5387 (2016).
27. M. M. Myerburg *et al.*, AMPK agonists ameliorate sodium and fluid transport and inflammation in cystic fibrosis airway epithelial cells. *Am J Respir Cell Mol Biol* **42**, 676-684 (2010).
28. R. C. Boucher, Evidence for airway surface dehydration as the initiating event in CF airway disease. *J Intern Med* **261**, 5-16 (2007).
29. T. J. Miller, P. B. Davis, FXYD5 modulates Na+ absorption and is increased in cystic fibrosis airway epithelia. *Am J Physiol Lung Cell Mol Physiol* **294**, L654-664 (2008).
30. D. Peckham, E. Holland, S. Range, A. J. Knox, Na+/K+ ATPase in lower airway epithelium from cystic fibrosis and non-cystic-fibrosis lung. *Biochem Biophys Res Commun* **232**, 464-468 (1997).
31. F. Van Goor, H. Yu, B. Burton, B. J. Hoffman, Effect of ivacaftor on CFTR forms with missense mutations associated with defects in protein processing or function. *Journal of Cystic Fibrosis* **13**, 29-36 (2014).
32. J. Hull, S. Shackleton, A. Harris, Abnormal mRNA splicing resulting from three different mutations in the CFTR gene. *Hum Mol Genet* **2**, 689-692 (1993).
33. T. M. Anderson *et al.*, Amphotericin forms an extramembranous and fungicidal sterol sponge. *Nat Chem Biol* **10**, 400-406 (2014).
34. V. Monforte *et al.*, Nebulized liposomal amphotericin B prophylaxis for Aspergillus infection in lung transplantation: pharmacokinetics and safety. *J Heart Lung Transplant* **28**, 170-175 (2009).
35. W. B. Guggino, The Cystic Fibrosis Transmembrane Regulator Forms Macromolecular Complexes with PDZ Domain Scaffold Proteins. *Proceedings of the American Thoracic Society* **1**, 28-32 (2004).
36. P. H. Karp *et al.*, An in vitro model of differentiated human airway epithelia. Methods for establishing primary cultures. *Methods Mol Biol* **188**, 115-137 (2002).
37. P. S. Chen, T. Y. Toribara, H. Warner, Microdetermination of Phosphorus. *Analytical Chemistry* **28**, 1756-1758 (1956).

38. N. J. Andrews *et al.*, Structurally simple lipid bilayer transport agents for chloride and bicarbonate. *Chemical Science* **2**, 256-260 (2011).
39. N. Busschaert *et al.*, Tripodal transmembrane transporters for bicarbonate. *Chem Commun (Camb)* **46**, 6252-6254 (2010).
40. N. Busschaert *et al.*, Synthetic transporters for sulfate: a new method for the direct detection of lipid bilayer sulfate transport. *Chemical Science* **5**, 1118-1127 (2014).
41. A. A. Pezzulo *et al.*, Reduced airway surface pH impairs bacterial killing in the porcine cystic fibrosis lung. *Nature* **487**, 109-113 (2012).
42. D. C. Devor *et al.*, Bicarbonate and chloride secretion in Calu-3 human airway epithelial cells. *J Gen Physiol* **113**, 743-760 (1999).
43. D. Y. Cho, M. Hajighasemi, P. H. Hwang, B. Illek, H. Fischer, Proton secretion in freshly excised sinonasal mucosa from asthma and sinusitis patients. *Am J Rhinol Allergy* **23**, e10-13 (2009).
44. H. Fischer, J. H. Widdicombe, Mechanisms of Acid and Base Secretion by the Airway Epithelium. *The Journal of membrane biology* **211**, 139-150 (2006).
45. H. Fischer, Function of Proton Channels in Lung Epithelia. *Wiley Interdiscip Rev Membr Transp Signal* **1**, 247-258 (2012).
46. E. N. Worthington, R. Tarran, Methods for ASL measurements and mucus transport rates in cell cultures. *Methods Mol Biol* **742**, 77-92 (2011).